# PHOTOPRODUCTION OF ETA MESONS FROM HYDROGEN AT $0^{\circ}$ AND $180^{\circ}$ FOR ENERGIES BETWEEN 0.7 AND 1.1 GEV

Thesis by
William A. McNeely, Jr.

In Partial Fulfillment of the Requirements
For the Degree of
Doctor of Philosophy

California Institute of Technology
Pasadena, California

1971

(Submitted May 4, 1971)

# ACKNOWLEDGMENTS

The originator of this experiment was C. A. Heusch, who provided the advice, active participation, and constant encouragement needed to make the project possible. Steve Yellin, who collaborated with me, brought to the experiment his high standards of excellence and a steady commitment to the hard work involved.

We owe a debt of gratitude to many people. Charles Prescott gave us invaluable assistance with the on-line computer and related electronics. Walter Nilsson and Bill Friedler designed and assembled equipment for us, and Joe Ungerer lent his mechanical expertise. Paul VanLigten and the synchrotron crew provided continual, competent support, as did the beam operators under Al Neubieser. Earle Emery and Dick Wileman were responsible for the hydrogen and deuterium targets, and they helped out in many other ways.

With all of this help, we needed additional assistance in running the experiment. This was cheerfully provided by Kirk McDonald, Bruce Winstein, Steven Cheng, Leon Rochester, Robert Kline, Lily Yeh, and Ernest Jan. These people made the long hours of data collection more pleasant and eventful.

I would like to personally thank certain people for working closely with me and taking an interest in the outcome. Foremost is my wife Sonia, who, in addition to giving me continual encouragement, patiently suffered the burden of raising a family as the wife of a graduate student. Special thanks to Kirk McDonald , Gary Luxton,

and Geoffrey Fox for their help with the theoretical interpretation of the experimental results, and to R. L. Walker for several informative discussions. Jorge Gonzalez, David Miller, and Roger Schreiber facilitated my computing task on the IBM 360/75. My thanks also to Virginia Franklin, who typed this thesis.

I gratefully acknowledge the financial support of the National Science Foundation and the California Institute of Technology.

## ABSTRACT

We have measured, using the Caltech 1.5-GeV electron synchrotron, the cross section for $\gamma p \rightarrow p\eta(\eta \rightarrow \gamma\gamma)$ at $0^{\circ}$ and $180^{\circ}$ in the energy range 0.7 to 1.1 GeV. Two totally-absorbing lead glass Cherenkov counters detected both photons from the decay $\eta \rightarrow \gamma\gamma$, while the recoil proton went undetected. Eta events produced a peak in the di-photon energy spectrum of the two counters. Approximately 100,000 eta events were identified using a background subtraction procedure.

The energy of the incident photon was not well resolved experimentally, which made the cross section evaluation difficult. One method of evaluation localizes the incident photon energy artificially by forming appropriate linear combinations of the physical measurements. An alternate method parametrizes the cross section as a smooth function of energy and fits the physically measured yield of eta events. The two methods agree tolerably well.

A significant departure from angular isotropy in the cross section is observed starting at about 0.8 GeV, with the backward cross section dominating the forward cross section. We interpret this result, plus recent measurements of the recoil proton polarization, in the framework of a simple resonance model. Tentative upper limits are set for the contributions of the states $P_{11}(1460)$ and $S_{11}(1710)$ to the amplitude for eta photoproduction.

To my girls

TABLE OF CONTENTS


| PART | TITLE | PAGE |
|---|---|---|
| 1. | INTRODUCTION | 1 |
| 2. | EXPERIMENTAL METHOD | 8 |
| 3. | DATA ANALYSIS | 19 |
| | 3.1 General | 19 |
| | 3.2 Preliminary Data Processing | 28 |
| | 3.3 Background Fitting | 34 |
| | 3.4 Foreground Fitting | 45 |
| | 3.5 Combined Background and Foreground Fitting | 49 |
| | 3.6 Cross Section Evaluation | 54 |
| | A. General Considerations | 56 |
| | B. Method of Linear Combinations | 58 |
| | C. Method of Parametrization | 59 |
| 4. | RESULTS | 62 |
| 5. | DISCUSSION | 78 |
| | 5.1 Comparison with Previous Measurements | 78 |
| | 5.2 Phenomenological Analysis | 79 |
| | A. Scope of the Analysis | 81 |
| | B. Formalism | 83 |
| | C. Numerical Results | 86 |
| | 5.3 Conclusions | 94 |

| PART | TITLE | PAGE |
|---|---|---|
| 6. | APPENDIX | 95 |
| | 6.1 Primary Photon Beam; Beam Monitoring | 95 |
| | 6.2 The Hydrogen Target | 100 |
| | 6.3 The Photon Telescopes | 104 |
| | A. Calibration | 105 |
| | B. Resolution | 111 |
| | C. Gain Matching | 114 |
| | 6.4 Operating Procedure | 116 |
| | 6.5 Timing Optimization | 120 |
| | 6.6 Maximum Likelihood Method | 123 |
| | 6.7 Efficiency Calculation | 132 |
| | A. Monte Carlo Method | 132 |
| | B. Approximate, Closed Form Method | 138 |
| | 6.8 Electronic Dead Time, Empty Target Corrections | 142 |
| | 6.9 Synchrotron Endpoint Calibration | 145 |
| | 6.10 Error Analysis | 146 |
| | A. Background-Foreground Fitting Method | 146 |
| | B. Uncertainties in the Eta Yield | 158 |
| | C. Uncertainties in the Cross Section Evaluation | 164 |
| 7. | REFERENCES | 166 |

# LIST OF FIGURES


| FIGURE | TITLE | PAGE |
|---|---|---|
| 1.1 | Cross Section for Eta Photoproduction | 4 |
| 1.2 | Recoil Proton Polarization at $90^{o}$ | 5 |
| 2.1 | Experimental Layout | 9 |
| 2.2 | Electronics Block Diagram | 12 |
| 2.3 | Oscilloscope Displays | 13 |
| 2.4 | Experimental Layout with Temporary Proton Telescope | 16 |
| 2.5 | Two-photon Invariant Mass Spectra, Without (a) and With (b) Proton in Coincidence | 18 |
| 3.1 | $(E_1, E_2)$ Spectrum, All Events of a Typical Run | 20 |
| 3.2 | $(E_1, E_2)$ Spectrum, Estimated Background | 23 |
| 3.3 | $(E_1, E_2)$ Spectrum, Estimated Foreground | 24 |
| 3.4 | $(E_1, E_2)$ Spectrum, All Events Minus Background | 26 |
| 3.5 | $(E_1, E_2)$ Spectrum, All Events Minus Background and Minus Foreground | 27 |
| 3.6 | Typical Time Difference Spectrum | 29 |
| 3.7 | Typical Time Difference Spectrum, Eta Events Only | 31 |
| 3.8 | Typical Photon Energy Spectrum for One Shower Counter | 32 |
| 3.9 | Typical Invariant Mass Spectrum | 35 |
| 3.10 | The Matrix $N(i_1, i_2)$, All Events of a Below-Threshold Run | 37 |

# LIST OF FIGURES


| FIGURE | TITLE | PAGE |
|---|---|---|
| 3.11 | The Matrix $(N - F)(i_1, i_2)$ | 41 |
| 3.12 | The Matrix $N(i_1, i_2)$ With a Mass Cut | 43 |
| 3.13 | The Matrix $(N - F)(i_1, i_2)$ With a Mass Cut | 44 |
| 4.1 | Cross Section for (a) Forward and (b) Backward Photoproduction | 66 |
| 4.2 | Error Envelope of (a) $\sigma_o(k)$ and (b) $\sigma_1(k)$, $\chi^2 = 60$ | 69 |
| 4.3 | Error Envelope of (a) $\sigma_o(k)$ and (b) $\sigma_1(k)$, $\chi^2 = 20$ | 70 |
| 4.4 | Error Envelope of (a) $\sigma_o(k)$ and (b) $\sigma_1(k)$, $\chi^2 = 4$ | 71 |
| 4.5 | Hybrid Results for (a) $\sigma_o(k)$ and (b) $\sigma_1(k)$ | 76 |
| 5.1 | Comparison with Previous Measurements: (a) $\sigma_o(k)$ and (b) $\sigma_1(k)$ | 80 |
| 5.2 | Resonance Model Solutions for (a) $\sigma_o(k)$, (b) $\sigma_1(k)$, and (c) $P(90^o)$ | 92 |
| 6.1 | Charge Ratio, Quantameter to Ion Chamber, as a Function of Endpoint Energy | 98 |
| 6.2 | Force Fed Hydrogen Target | 102 |
| 6.3 | Condensing Type Hydrogen Target | 103 |
| 6.4 | Shower Counter, Side View | 106 |
| 6.5 | Phototube Arrangement in Shower Counter | 107 |

| FIGURE | TITLE | PAGE |
|---|---|---|
| 6.6 | Mean Pulse Height as a Function of Shower Energy | 109 |
| 6.7 | Pulse Height Spectrum of Bi-207 Source | 110 |
| 6.8 | Apparent Number of Photoelectrons as a Function of Shower Energy | 113 |
| 6.9 | Time Difference Spectrum, Before (a) and After (b) Slewing Compensation | 121 |
| 6.10 | Slewing Compensation as a Function of Photon Energy | 124 |
| 6.11 | Two Examples of Time Difference Spectrum Obtained with 100 ns Delay Between the Shower Counters | 131 |
| 6.12 | Detection Efficiency as a Function of Incident Photon Energy and Center-of-Mass Production Angle | 134 |
| 6.13 | Geometry of Hypothetical Point Counters, as Seen in the Laboratory Frame (a) and the Eta Rest Frame (b) | 139 |
| 6.14 | Squared Amplitude as a Function of Incident Photon Energy for Three Values of the Endpoint Calibration Constant | 147 |

# LIST OF TABLES


| TABLE | TITLE | PAGE |
|---|---|---|
| 2.1 | Table of Experimental Settings | 15 |
| 4.1 | Cross Section for Forward and Backward Photoproduction | 63 |
| 4.2 | Cross Section for Forward and Backward Photoproduction, Hybrid Results | 73 |
| 5.1 | Values of the Parameters in the Phenomenological Analysis | 88 |
| 6.1 | Effects of Variations in the Background-Foreground Fitting Method | 150 |
| 6.2 | Results of Fitting Sub-Divided Runs | 160 |

# 1. INTRODUCTION

This experiment on the forward and backward cross section of the process

$$\gamma p \rightarrow p\eta \ ,$$

performed at the Caltech 1.5 GeV electron synchrotron, was motivated by increasing interest in the angular structure of the cross section in the resonance region of that reaction. Prior to the start of the experiment, other experiments[2,3,6] had resolved no definite deviation from isotropy in the cross section, although such might well be expected on the basis of interference between various resonances. Interest in this point has since been heightened by a recent measurement of the recoil proton polarization in this process.[1] That experiment detected interference effects, albeit through a different bilinear combination of the interfering amplitudes, and a deviation from isotropy was predicted. The present experiment measured the cross section for center of mass angles localized about $0^{\circ}$ and $180^{\circ}$, for laboratory energies from threshold (~0.71 GeV) to about 1.1 GeV. Before considering the resonance picture in eta photoproduction from protons, let us recall the situation as known from other reactions.

A wealth of information about nucleon isobars has emerged from $\pi N$ phase shift analyses. The quantum numbers of these isobars, along with the masses and partial widths, are the objects of a continuing theoretical and experimental investigation. For information on the nucleon electromagnetic current, one must turn to

photoproduction or electroproduction experiments, since the radiative decays of nucleon isobars are sufficiently rare so as to escape most attempts at direct observation. Of the photoproduction experiments, the most accessible is pion photoproduction. For that reaction, a fairly consistent resonance picture can be formulated, but only in a highly non-unique fashion.[13] The dominant resonances in pion photoproduction are the $P_{33}(1238)$, $D_{13}(1536)$, and the $F_{15}(1688)$, the so-called first, second, and third resonances. A lively theoretical interest has centered on the radiative decay widths (or photoexcitation amplitudes) of these and other resonances. Left very much in doubt by pion photoproduction are the photoexcitation widths of certain $I = 1/2$, $J = 1/2$ isobars, such as

$$P_{11}(1460)$$

$$S_{11}(1550)$$

$$S_{11}(1710)$$

$$P_{11}(1780) \quad .$$

Let us see why eta photoproduction is a potentially better probe for these isobars.

Eta photoproduction, unlike pion photoproduction, singles out $I = 1/2$ isobars in the intermediate state. This follows from isospin conservation at the final vertex. At the initial vertex, the photon may interact with either the isoscaler or isovector part of the nucleon electromagnetic current, but the isovector coupling to $I = 3/2$

states vanishes in eta photoproduction. The amplitudes for eta photoproduction from protons and neutrons are simply the sum and difference of the isoscalar and isovector amplitudes. Denoting the isoscalar and isovector amplitudes by $A^S$ and $A^V$ respectively, the eta photoproduction amplitudes are

$$A(\gamma p \rightarrow p\eta) = \frac{1}{\sqrt{2}} (A^s - A^v)$$

$$A(\gamma n \rightarrow n\eta) = \frac{1}{\sqrt{2}} (A^s + A^v) .$$

Experimentally, the cross section for eta photoproduction from protons shows an uncomplicated energy structure, as seen in Figure 1.1. There is a large peak above threshold, above which is a dip and a flat, broad peak centered at about 1.2 GeV. The angular dependence (not shown in Figure 1.1) appears to be consistent with isotropic, with a hint of a forward dip at higher energies.[14] The recoil proton polarization is sizable near $90^\circ$, as shown in Figure 1.2.

As expected, the observed features of eta photoproduction are satisfactorily accounted for with a small number of isobar terms. Good descriptions of the cross section are reported with the isobars $S_{11}(1550)$ and $P_{11}(1780)$,[4] which also appear to suffice when the polarization data are included.[1] The apparent absence of certain isobars is not surprising. Little or no contribution from the $D_{13}(1536)$ is expected, on several grounds. For one, an angular momentum barrier of the form $q^{2\ell+1} = q^5$ suppresses the D wave part

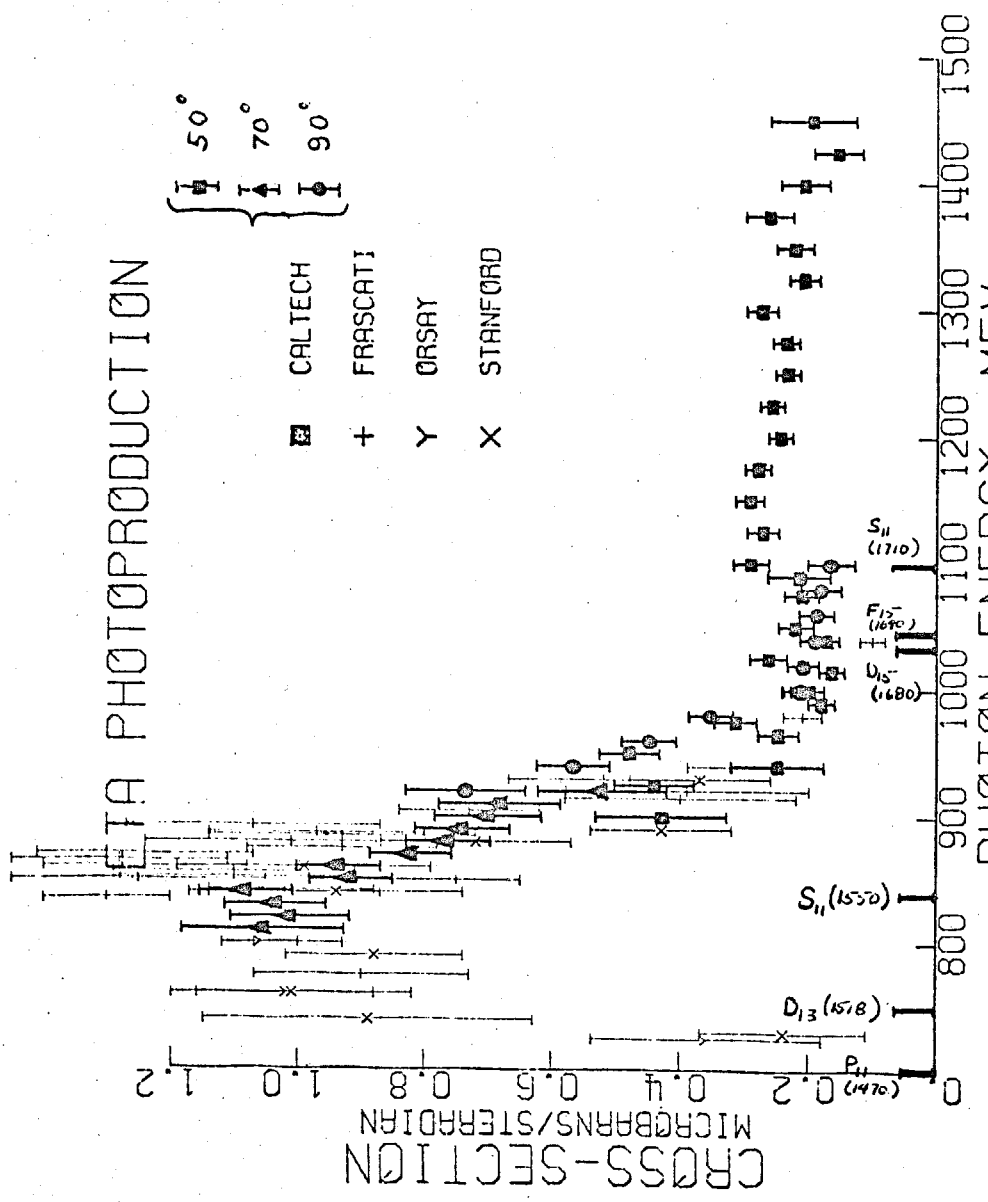


Figure 1.1 Cross Section for Eta Photoproduction

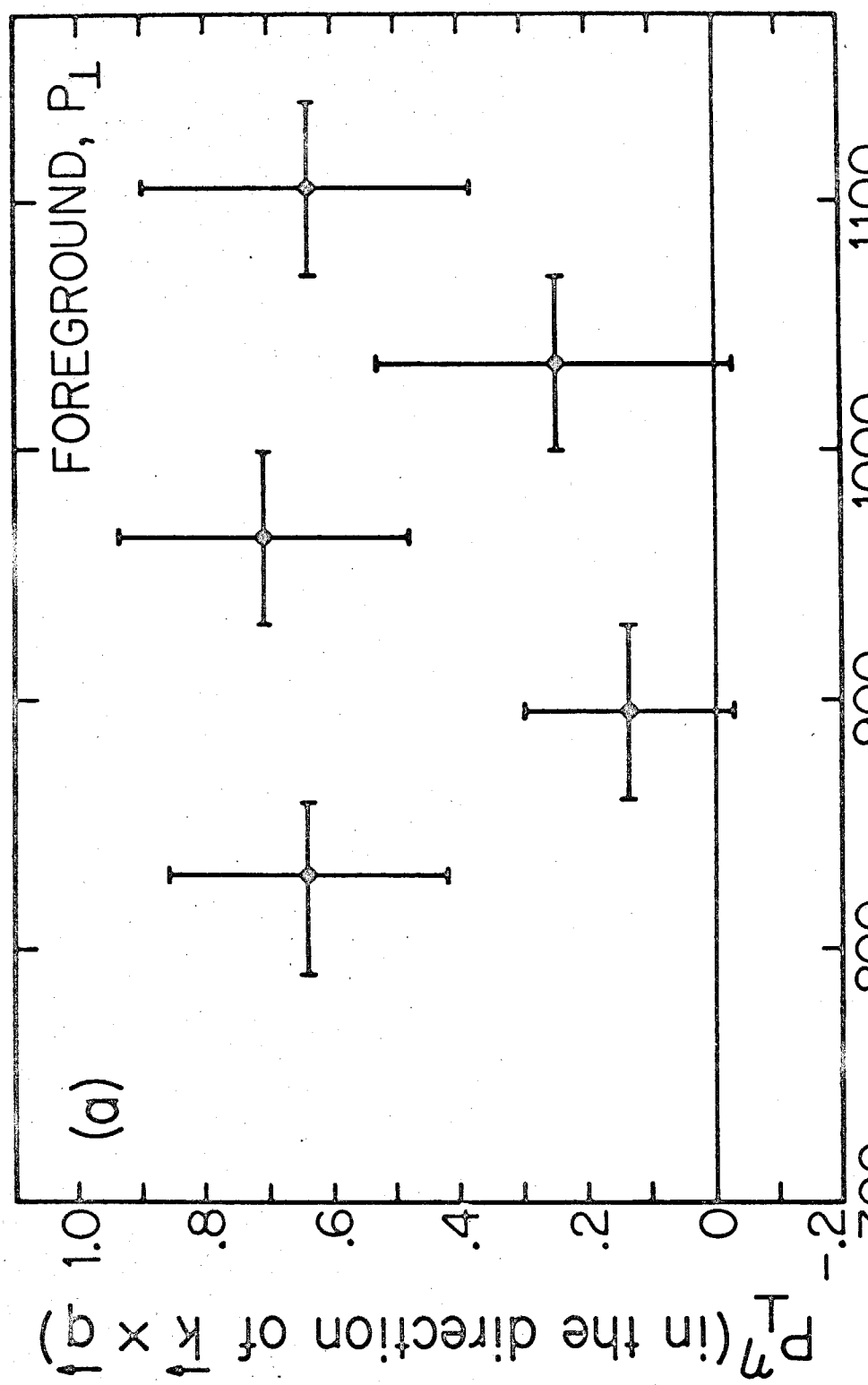


Figure 1.2 Recoil Proton Polarization at 90°.

of the amplitude just above threshold. For another, as Yellin points out,[5] the interference between this resonance and any S or P wave is expected to be suppressed by virtue of the fact that the $D_{13}(1536)$ (also the $F_{15}(1688)$) is produced primarily in the $J_z = 3/2$ state.[13]

The $F_{15}(1688)$ is a prominent feature in $\pi N$ elastic scattering and in pion photoproduction. In $\pi^- p \to \eta n$, however, one can only place an upper limit of $\sim 0.3$ μb for an enhancement at 1688 Mev.[33] We can relate that result to eta photoproduction by writing

$$\left[\frac{\sigma(\gamma p \to \eta\, p)}{\sigma(\gamma p \to \pi^+ n)} = \frac{\sigma(\pi^+ n \to \eta\, p)}{\sigma(\pi^+ n \to \pi^+ n)}\right]_{F_{15}\ \text{part of}\ \sigma} \tag{1.1}$$

and using isospin arguments on the right-hand side to relate numerator and denominator with the $F_{15}$ parts of $\sigma(\pi^- p \to \eta n)$ and $\sigma(\pi^- p \to \pi^- p)$, respectively. Putting in numbers,[13,20] we find that $\sigma(\gamma p \to \eta p)_{F_{15}} \lesssim 1$ μb is the upper limit for an enhancement at 1688 Mev in eta photoproduction, compared with an observed total cross section of $\sim 2.5$ μb (cf. Figure 1.1). We may arrive at essentially the same conclusion using SU(3) arguments and experimental data on the partial widths of the $F_{15}(1688)$ and its $J^P = (5/2)^+$ octet partners, $\Lambda(1815)$, $\Sigma(1940)$, and (tentatively) $\Xi(2030)$. For example, the ratio of the couplings $(F_{15}N\eta)$ to $(F_{15}N\pi)$ is, from SU(3) Clebsch-Gordon coefficients, $(3 - 4\alpha)^2/3$, where $\alpha/(1 - \alpha)$ is the D/F ratio for coupling the $(5/2)^+$ octet to the $(1/2)^+$ and $0^-$ baryon and meson octets.[32] The coupling $(F_{15}N\eta)$ vanishes if $\alpha = 3/4$. It is interesting to note that the $(5/2)^+$ octet is the first Regge recurrence of the $(1/2)^+$ octet, and SU(6) considerations yield $\alpha = 3/5$ for coupling $(1/2)^+$ to $(1/2)^+$ and $0^-$.[34] In a

systematic study of the known partial widths in the $(5/2)^+$ octet, where kinematical factors are accounted for in a reasonable way, Tripp et al. find $\alpha = 0.46$ (with an error of 0.1) in good agreement with all known partial widths except the $\Sigma\pi$ decay of $\Sigma(1940)$.[35] In a later study, Flaminio et al. find $\alpha = 0.40$ in good agreement with <u>all</u> known partial widths, where the $\Sigma\pi$ decay of $\Sigma(1940)$ had been re-measured.[39] According to that more recent study, $\Gamma(F_{15} \to N\eta)/\Gamma(F_{15} \to N\pi) \simeq 1$ Mev/73 Mev. This gives us that

$$\left[\frac{\sigma(\gamma p \to \eta\, p)}{\sigma(\gamma p \to \pi^+ n)}\right]_{F_{15}} \simeq \frac{1}{2/3(73)} \simeq 0.02,$$

and, using 25 μb for $\sigma_{F_{15}}(\gamma p \to \pi^+ n)$,[13] $\sigma_{F_{15}}(\gamma p \to \eta p) \simeq 0.5$ μb or about 20% of the total cross section at the $F_{15}$ peak (compared with the upper limit of about 40% obtained using Eq. (1.1)). From this evidence, and from the fact that the cross section is at a relative minimum at the $F_{15}$ mass (photon energy of about 1.0 Gev), we feel justified in neglecting the $F_{15}$ contribution to eta photoproduction.

Two interesting questions are left open by the possibility of observing the $P_{11}(1460)$ and the $S_{11}(1710)$ in eta photoproduction. Pion photoproduction[7] and other reactions[8,9] have failed to conclusively turn up the $P_{11}(1460)$ "Roper resonance," which was first identified in $\pi N$ phase shift analyses.[10] Although the peak of this resonance is probably below the threshold for eta photoproduction, the tail of the peak should interfere with the $S_{11}(1550)$ above threshold, producing a sharp deviation from isotropy in the cross section. A similarly sharp deviation from isotropy would be expected of interference between the

$S_{11}(1710)$ and the $P_{11}(1780)$. Although the $S_{11}(1710)$ is predicted to be not photoexcitable in the non-relativistic quark model,[11] configuration mixing between this state and the $S_{11}(1550)$ could lead to some photoexcitation of the former, notwithstanding the quark model selection rule.

As seen in Figure 1.2, the recoil proton polarization at $90^{\circ}$ is sizable in the energy region spanned by the $S_{11}(1550)$ and the $P_{11}(1780)$. This could only result from an admixture of opposite parity (although not necessarily resonant) amplitudes, most likely P wave in the region of the $S_{11}(1550)$ and S wave in the region of the $P_{11}(1780)$. However, there is as yet no firm indication for the presence of either the $P_{11}(1460)$ or the $S_{11}(1710)$, since interference between the $S_{11}(1550)$ and the $P_{11}(1780)$ alone may plausibly account for the observed polarization.[1] The roles of the $P_{11}(1460)$ and the $S_{11}(1710)$ in eta photoproduction can only be clarified with the aid of information from other interference-sensitive experiments, such as the present one on the cross section anisotropy. There are obvious inplications of the observation or non-observation of these states in photoexcitation experiments for their proper assignments in terms of models for baryon spectroscopy. We will briefly touch on these points in the Discussion section below.

# 2. EXPERIMENTAL METHOD

The goal is to measure the differential cross section for the reaction

$$\gamma p \rightarrow p\eta$$

for center of mass production angles near $0^{\circ}$ and $180^{\circ}$ and for energies between threshold (0.709 GeV) and about 1.1 GeV. The method is to detect only the final state eta meson by its 38% decay mode

$$\eta \rightarrow \gamma\gamma \qquad (2.1)$$

using two photon telescopes in coincidence. The recoil proton is not detected, for it travels along the beam line in $0^{\circ}$ or $180^{\circ}$ photoproduction and is not easily separated from the primary photon beam. Moreover, in $0^{\circ}$ photoproduction the proton may fail to escape from the liquid hydrogen target for lack of energy.

The experimental layout is shown in Figure 2.1. The synchrotron accelerates a circulating beam of electrons which collides with an internal tantalum target, producing a bremsstrahlung photon beam. The photon beam, which emerges from the synchrotron through a mylar window, is collimated, scraped, and swept before reaching the target in the experimental area. Further downstream, the beam is monitored by an ion chamber and finally absorbed in a beam catcher. The photon beam and its monitoring are more fully described in Section 6.1; the hydrogen target in Section 6.2.

For the detection of the final state 2.1, two photon telescopes are arranged symmetrically with respect to the beam line in

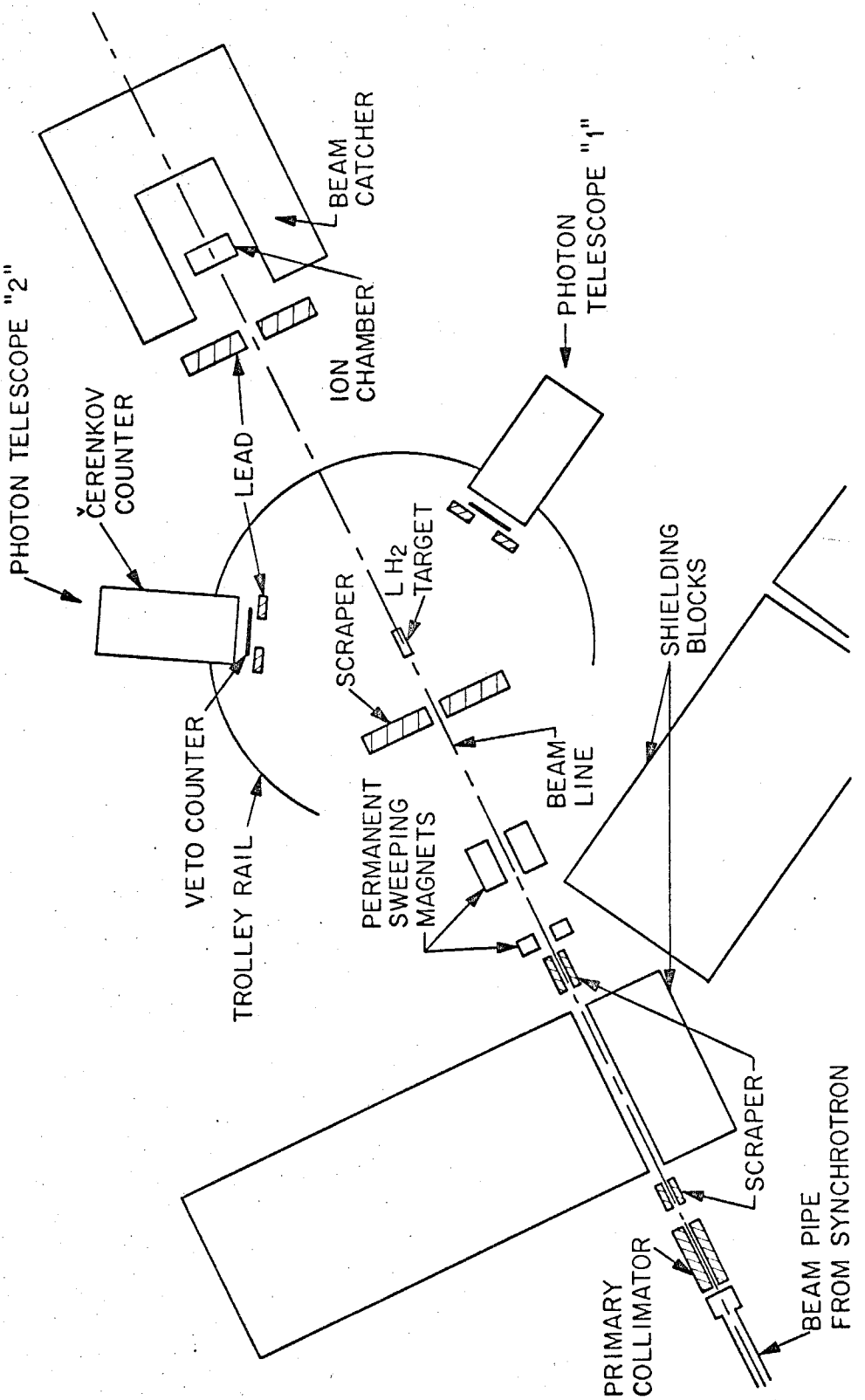


Figure 2.1 Experimental Layout

a horizontal plane. The telescopes are mounted on trolleys which ride a circular rail centered on the target. Each telescope, as described more fully in Section 6.3, consists of a defining lead aperture, a veto counter, and a totally absorbing Cherenkov shower counter. Each shower counter consists of a large block of lead glass to which seven phototubes are attached. Energy calibration is performed in a monenergetic electron beam, and an energy reference point is retained with the aid of a radioactive source and scintillator affixed to each lead glass block. Care was taken to optimize the photostatistical resolution for the combined signal of the seven phototubes; the light source for this optimization consisted of light emitting diodes attached to the lead glass.

Each shower counter is in anticoincidence with a veto counter which is biased on minimum-ionizing particles. The veto counter, located behind the lead aperture, is shielded from soft electrons by a layer of 1/2 inch lucite. Photons failing to pass through the aperture, entering the 1.25 inch lead wall instead, most likely convert in the lead and cause a veto signal. A "gamma" or possible photon is defined as an unvetoed shower which surmounts a bias of about 100 MeV. An "event" or possible eta decay is defined as the coincidence of two gammas in the two telescopes. The time between the gammas is recorded, so that the final coincidence requirement may be set in the data analysis. For each event, the time difference between showers and the two shower energies (rather, the corresponding digitized pulse heights) are recorded on magnetic tape under the supervision of

a PDP-5 computer. The electronic layout is shown schematically in Figure 2.2. The scalers indicated in that figure were useful in monitoring the progress of the experiment, and the scaler totals were recorded at the end of each run. The on-line computer, when it was not busy, drove an oscilloscope display which was most valuable in assessing the current status of the experiment and the quality of the accumulated data. Section 6.4 describes the experimental running procedure and explains the oscilloscope displays as reproduced in Figure 2.3 .

The symmetrical arrangement of the telescopes insures maximum eta detection efficiency. The angle $\theta_o$ between the downstream beam line and the center of either telescope aperture, measured from the center of the target, was varied in steps over the range $35^o$ to $97.5^o$. The value of $\theta_o$ indicates whether forward or backward eta production will dominate in the sample of etas collected, changing from forward to backward as $\theta_o$ increases. There is no sharp dividing line, but for $\theta_o$ near $65^o$, threshold production is favored and all production angles contribute. The detection efficiency is a rather slowly varying function of k, the incident photon energy, for k above the minimum kinematically permitted value (which is determined by $\theta_o$). The maximum value of k is the synchrotron endpoint energy, $E_o$. The poor experimental resolution in k is offset by the use of many settings of $E_o$ in conjunction with $\theta_o$. This usage of $E_o$ necessitated a less uncertain calibration of the synchrotron than previously existed. It proved possible to calibrate by using the data from this experiment taken near threshold; we return to this point in Section 6.9.

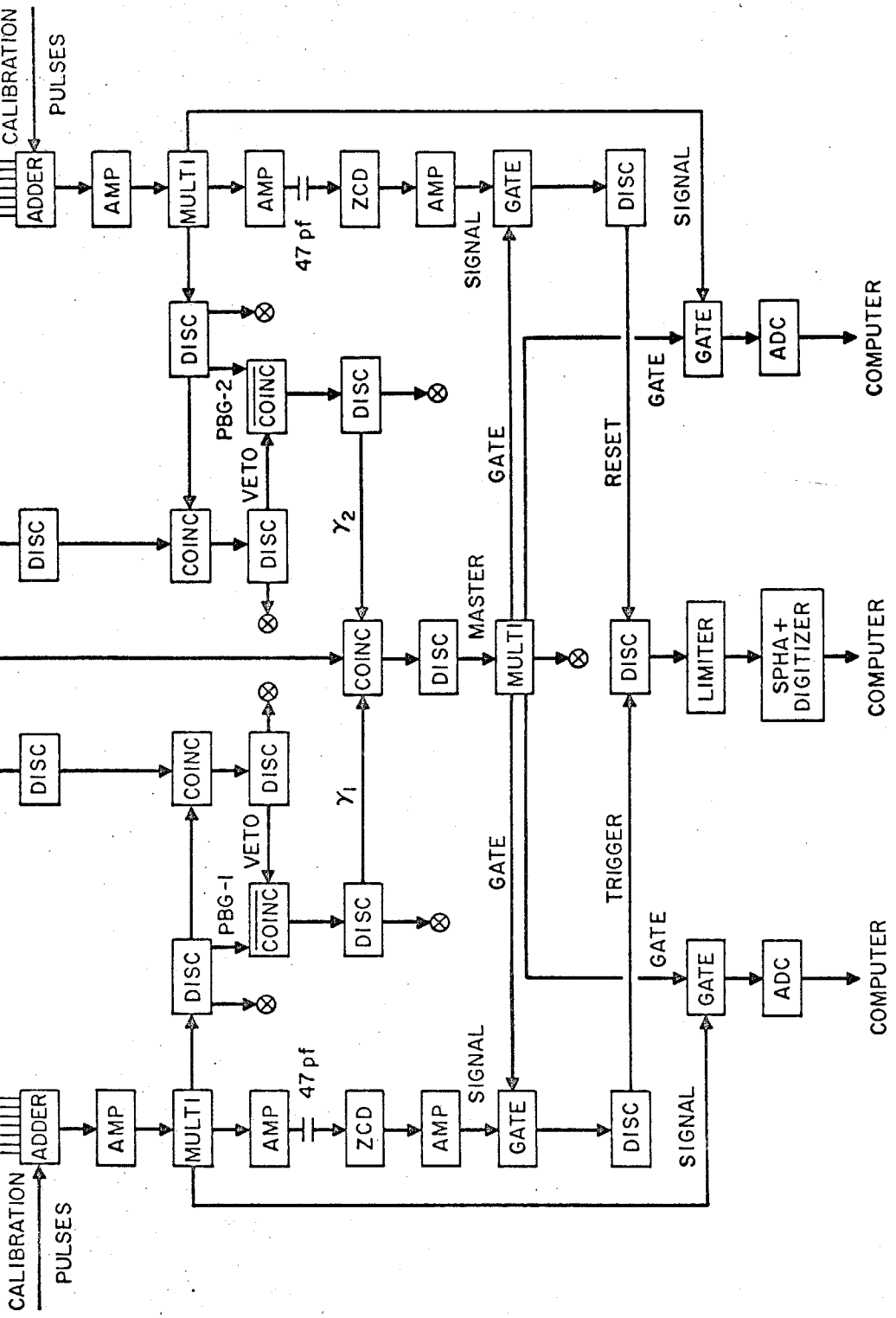


Figure 2.2 ELECTRONICS BLOCK DIAGRAM

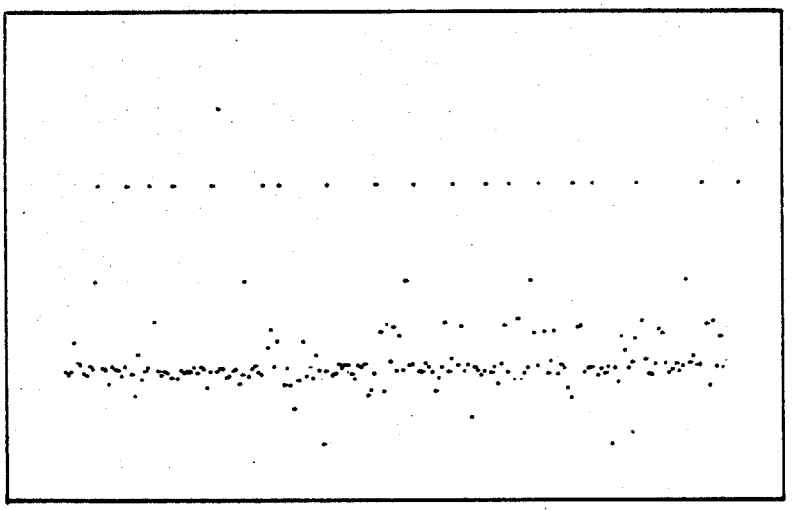

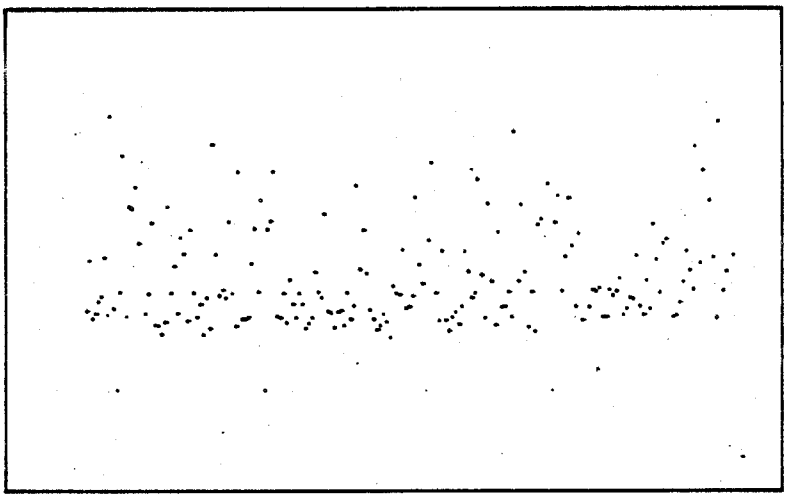

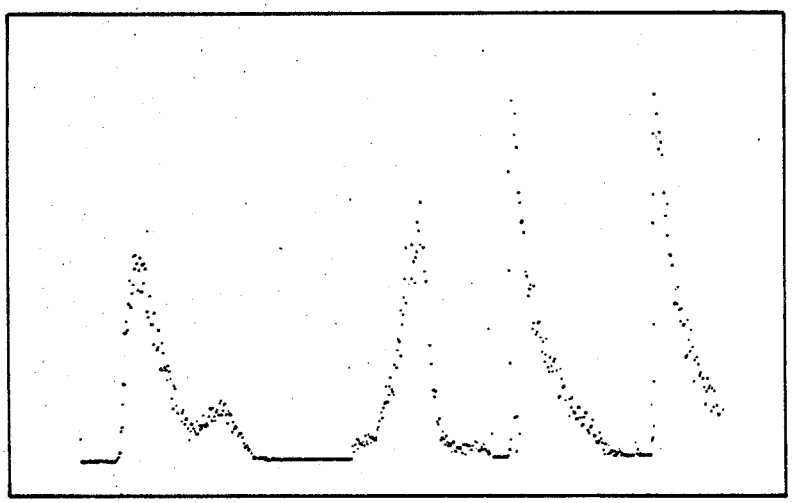

Figure 2.3 Oscilloscope Displays

Table 2.1 lists the settings of $\theta_o$ and $E_o$, the amount of beam allocated (in equivalent quanta), and the estimated number of eta events detected.

To the extent that we measure the four-momentum of each of the two photons from eta decay, we measure the four momentum of the eta. This ideally permits the identification of eta events by invariant mass and the determination of the reaction kinematics, assuming that the undetected recoil particle is a proton. For example, we could calculate the energy of the incident photon, starting from the two shower energies and the geometry of the counters. In practice, the kinematical resolution is such as to permit only the identification of etas on a statistical basis, using the distribution of shower energies to subtract the expected contamination of background events. We use the geometry of the counters to calculate the efficiency for eta detection irrespective of decay photon energies. The cross section is unfolded from the eta yields, using the detection efficiency, in two different ways. The more conventional way is a generalization of the method of synchrotron endpoint subtraction, and the other way involves fitting the cross section to a smooth curve. Both techniques are elaborated in Section 3.6, after the method for counting eta events has been introduced, and the results are presented in Section 4.

A test performed early in the experiment dramatically illustrates the price of not detecting the recoil proton. The photon telescopes and a temporary proton detector were arranged as shown in Figure 2.4. Data were then taken both with and without a proton

TABLE 2.1

TABLE OF EXPERIMENTAL SETTINGS

$\theta_o$ = Angle between beam line and either shower counter, in degrees.

$E_o$ = Nominal synchrotron endpoint energy, in MeV.

Q = Number of equivalent quanta (x $10^{13}$).

N = Number of eta events.

| $\theta_o$ | $E_o$ | Q | N |
|---|---|---|---|
| 35 | 1150 | 2.59 | 283 |
| 37 | 1025 | 2.09 | 90 |
| 37 | 1100 | 2.06 | 203 |
| 40 | 720 | 0.37 | 1 |
| 40 | 900 | 1.39 | 2176 |
| 40 | 925 | 0.26 | 33 |
| 40 | 950 | 1.90 | 236 |
| 40 | 1020 | 0.20 | 287 |
| 45 | 825 | 1.73 | 3786 |
| 45 | 850 | 2.05 | 5558 |
| 50 | 775 | 2.62 | 5150 |
| 50 | 800 | 3.31 | 5282 |
| 50 | 825 | 1.09 | 3780 |
| 55 | 710 | 1.60 | 365 |
| 55 | 725 | 1.72 | 1516 |
| 55 | 750 | 2.10 | 4503 |
| 55 | 775 | 2.34 | 7448 |
| 55 | 800 | 1.18 | 4779 |
| 60 | 730 | 0.86 | 1794 |
| 60 | 750 | 1.81 | 3759 |
| 60 | 800 | 0.46 | 349 |
| 65 | 690 | 1.80 | 0 |
| 65 | 700 | 2.30 | 258 |
| 65 | 710 | 1.75 | 1723 |
| 65 | 725 | 1.50 | 2421 |
| 65 | 750 | 1.68 | 4495 |
| 65 | 775 | 1.58 | 4868 |
| 65 | 800 | 1.53 | 4716 |
| 70 | 730 | 0.09 | 123 |
| 70 | 750 | 1.67 | 3518 |
| 75 | 725 | 1.27 | 538 |
| 75 | 740 | 0.50 | 510 |
| 75 | 750 | 1.91 | 2162 |
| 75 | 775 | 1.56 | 2744 |
| 75 | 800 | 3.73 | 8601 |

(cont.)

| $\theta_o$ | $E_o$ | Q | N |
|---|---|---|---|
| 75 | 825 | 1.88 | 4695 |
| 75 | 900 | 0.35 | 1069 |
| 80 | 775 | 1.32 | 1468 |
| 80 | 800 | 1.58 | 1779 |
| 80 | 825 | 2.31 | 3577 |
| 85 | 800 | 1.74 | 593 |
| 85 | 825 | 1.54 | 874 |
| 85 | 850 | 1.85 | 1382 |
| 85 | 875 | 1.95 | 1915 |
| 90 | 900 | 0.27 | 191 |
| 90 | 1020 | 0.62 | 275 |
| 93 | 1025 | 1.00 | 444 |
| 93 | 1100 | 0.92 | 435 |
| 95 | 770 | 1.14 | 123 |
| 95 | 1020 | 1.12 | 232 |
| 95 | 1100 | 3.84 | 466 |
| 97 | 1160 | 0.34 | 48 |
| 97 | 1175 | 0.96 | 70 |

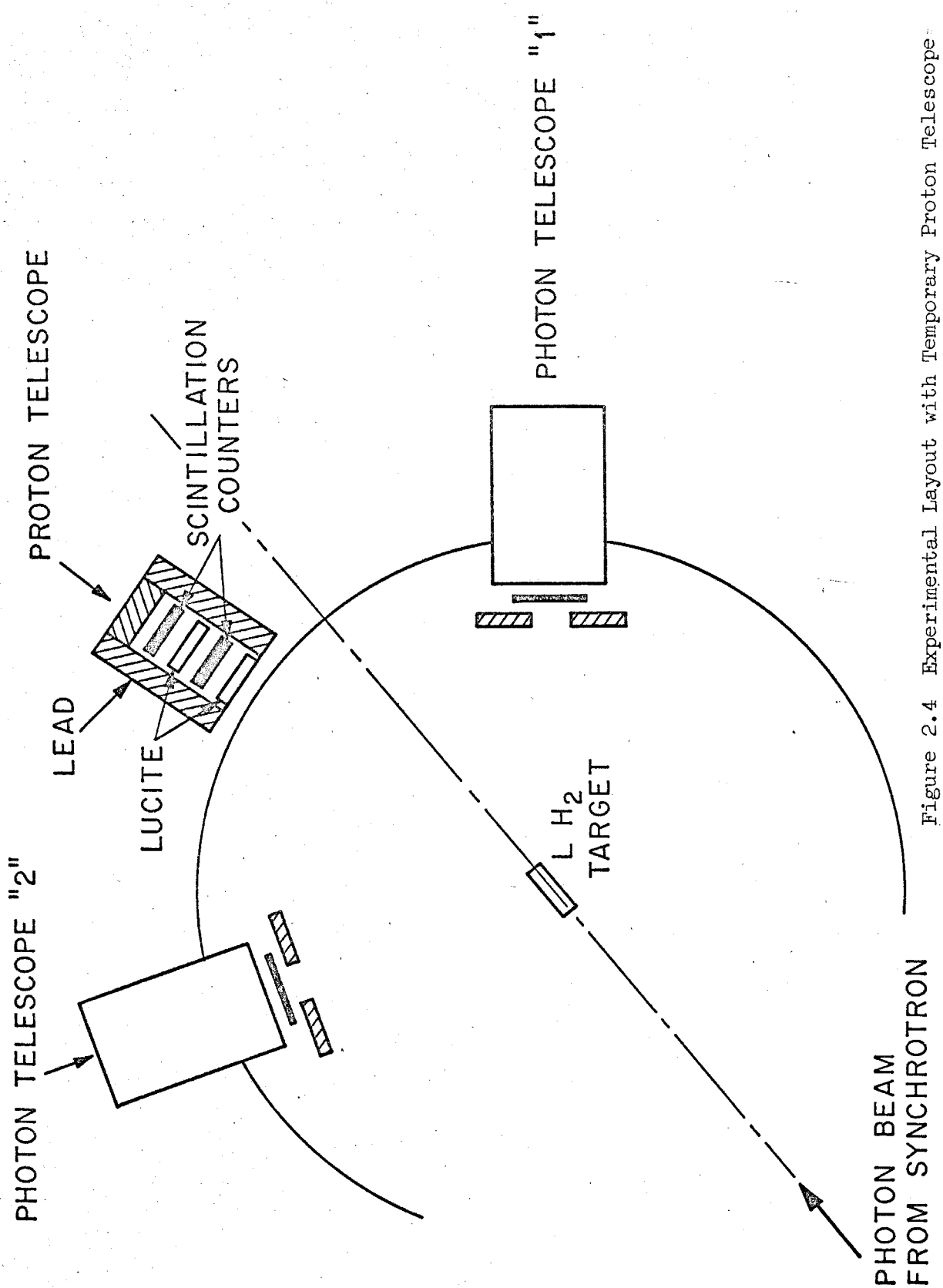


Figure 2.4 Experimental Layout with Temporary Proton Telescope

in coincidence with the two photons. The difference was immediately seen in the on-line display, operating in the mode which binned the geometric mean of the pulse heights representing two photons. This quantity scales like the two-photon invariant mass (see Section 3.2). Figure 2.5a shows the reconstructed mass spectrum for the data taken without a proton coincidence: a peak at the eta mass is superposed on the background (which is cut off at low mass by the shower counter pulse height biases). Compare this with Figure 2.5b, for which a proton coincidence was required: the background is now heavily suppressed. This test, incidentally, was valuable in verifying that eta events were responsible for the observed mass peak.

The test described above provides an opportunity to check that the cross section measurement made with the proton counter in coincidence is roughly consistent with the measurements made without a proton coincidence. Rather than unfold the cross section, which will be a weighted average over the incident photon energy from threshold to the endpoint energy of 820 Mev, we compare the eta yields and detection efficiencies for the runs taken both with and without the proton coincidence requirement. The most uncertain input is the solid angle subtended by the proton counter, as seen at the hydrogen target. We guess that the proton counter was a 4" x 8" detector located 40" from the target, but these numbers are subject to the vagaries of memory. We have made a crude estimate of the detection efficiency with the proton coincidence, and we find that it is a factor of $(15 \pm 5)$ less than the efficiency without the proton coincidence. On the other hand, the yield of eta events drops by a factor of $(14 \pm 2)$ when the proton

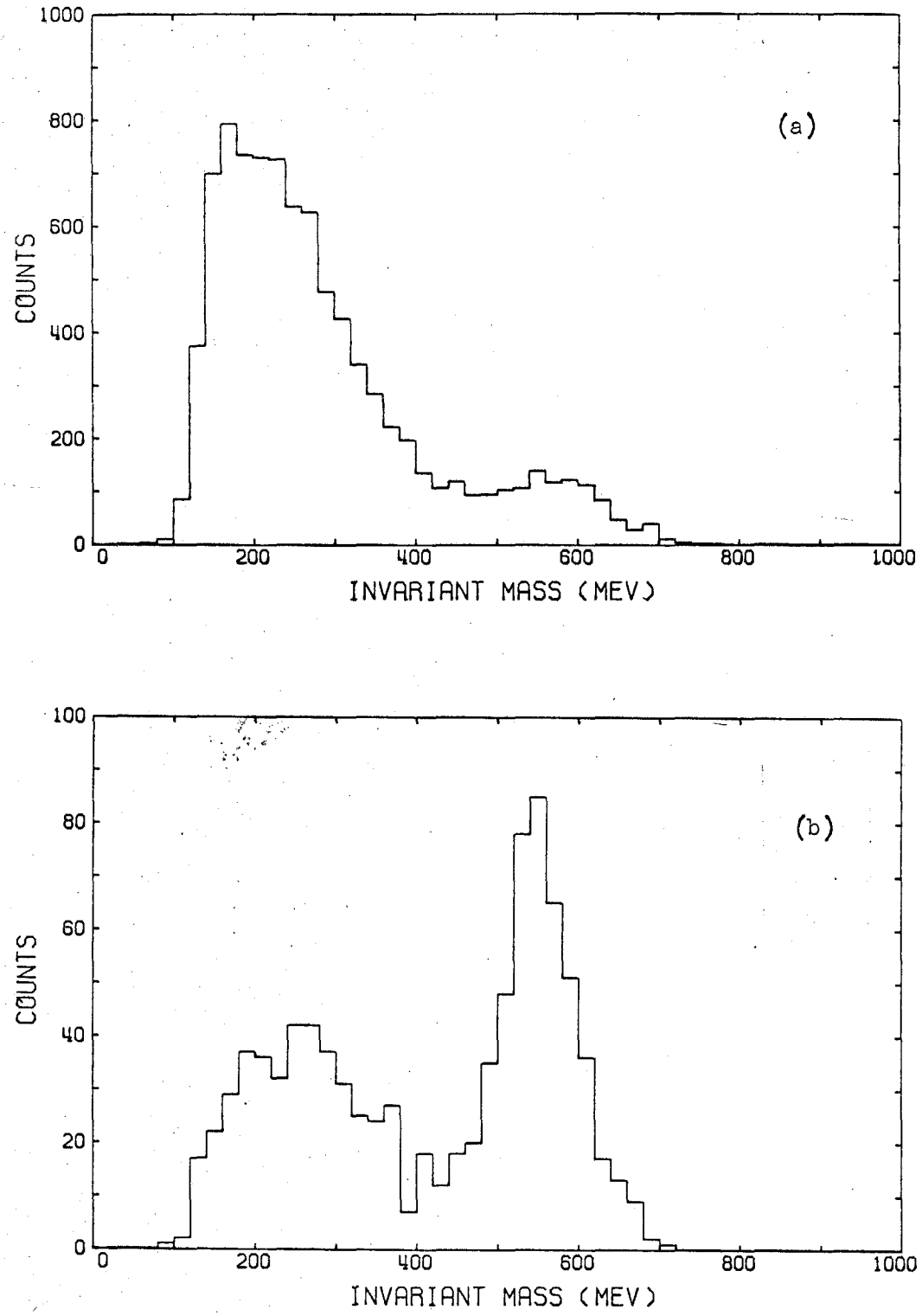


Figure 2.5 Two-Photon Invariant Mass Spectra, Without (a) and With (b) Proton in Coincidence

coincidence is demanded. Thus, we have equality, to within 40%, between the weighted values of the cross section measured with and without the proton coincidence. The weighting factor for the cross section, as a function of incident photon energy, is not identical in the two cases, but the difference in cross section normalization is not expected to be resolvable in this crude analysis. Finally, it was checked that, without a proton coincidence, the unsymmetrical setting of the photon telescopes (Figure 2.4) produced an eta yield consistent with a 30% drop in detection efficiency from the case of a symmetrical setting with the same opening angle between the telescopes.

The problem of background subtraction is discussed in detail in the next Section. For an idea of the magnitude of the background contamination, for detection of only the two photons from eta decay, we present here the ratio R = (foreground/all events) for events with two-photon invariant mass located in the vicinity of the eta mass. The following table lists R for events lying within 1.5 and 3.0 standard deviations of the eta mass peak, for representative kinematic settings defined by the half-opening angle $\theta_o$ and the endpoint energy $E_o$:

| $\theta_o$ | $E_o$ | $R(1.5\sigma)$ | $R(3.0\sigma)$ |
|---|---|---|---|
| 40 | 900 | 0.80 | 0.57 |
| 55 | 800 | 0.86 | 0.79 |
| 60 | 750 | 0.86 | 0.74 |
| 75 | 800 | 0.88 | 0.74 |
| 85 | 850 | 0.77 | 0.58 |
| 90 | 900 | 0.77 | 0.59 |

# 3. DATA ANALYSIS

The object of the data analysis is to extricate the differential cross section for the process

$$\gamma p \rightarrow p \eta \ (\eta \rightarrow \gamma\gamma)$$

from the experimental data produced by the two photon telescopes. We first outline the major features of the analysis and then treat certain aspects in detail.

## 3.1 General

For each setting of the telescope geometry and synchrotron endpoint energy where data were taken, there is a set of events to be analyzed for eta content. Each event contains information on the two shower energies, $E_1$ and $E_2$, and on the time at which one shower occurred relative to the other. The timing information is useful in excluding as many accidental coincidences as possible without excluding real coincidences. The $(E_1, E_2)$ distribution of events will contain a number of events from two-photon eta decays as well as a background of events from other sources. Figure 3.1 is a perspective view of the $(E_1, E_2)$ spectrum for a setting which produces a prominent eta peak. The eta peak is the relative maximum at the front right in Figure 3.1 , and the background is the steep slope on which the eta peak is located. The spectrum is seen to cut off for either $E_1$ or $E_2$ below certain values; this is the effect of the electronic biases on the shower counter signals.

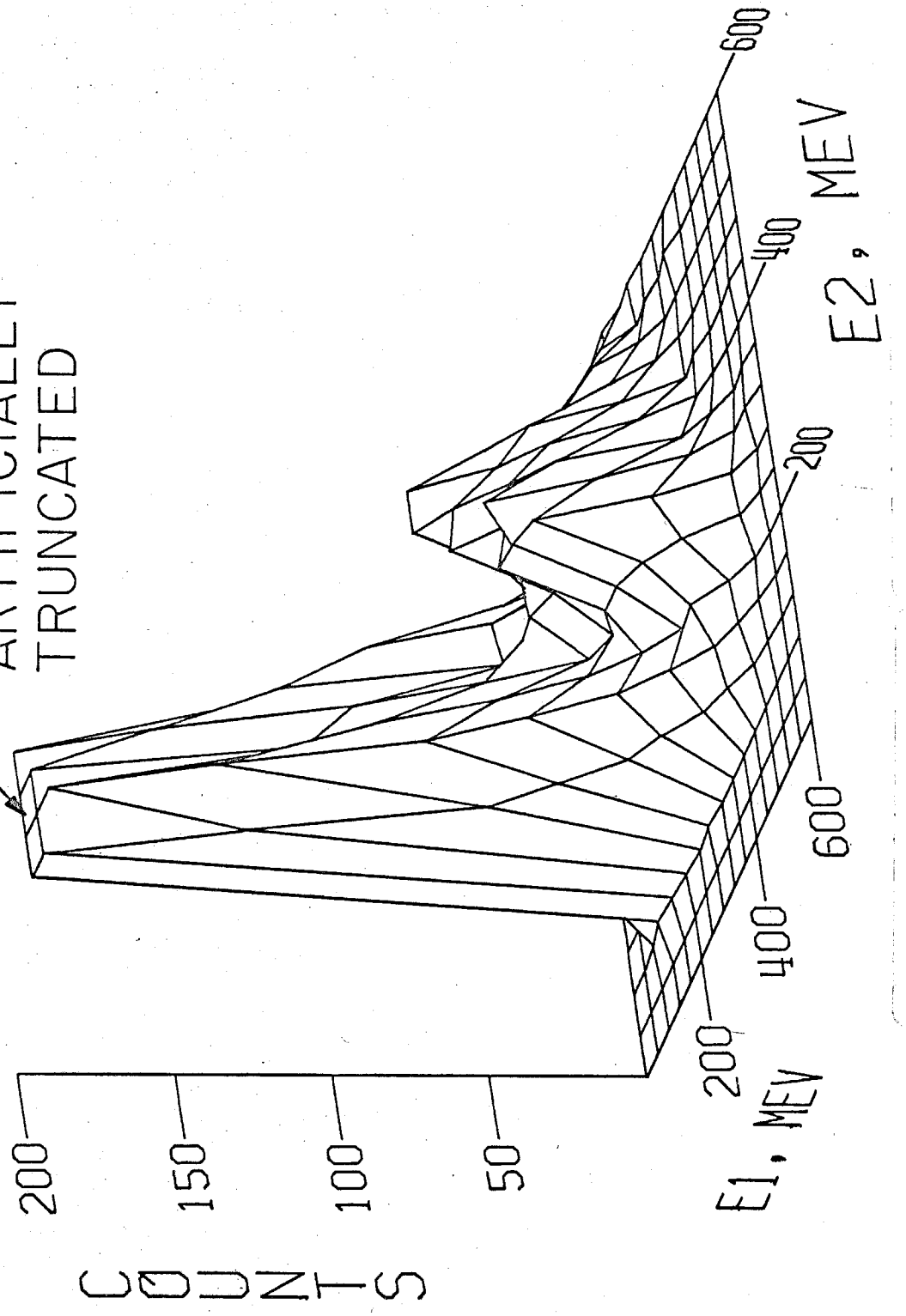


Figure 3.1 $(E_1, E_2)$ Spectrum, All Events of a Typical Run

A central problem in counting etas is the extrapolation of the spectrum of background events into the region of the eta peak. We do not attempt to predict the background from contributing processes, but rather we fit the background empirically. An uncorrelated term in $E_1$ and $E_2$ happens to fit the background quite well, provided that we exclude events with both $E_1$ and $E_2$ small, as shown in Section 3.3 . The $(E_1, E_2)$ spectrum is then fitted by the sum of an uncorrelated term and a term describing the eta peak. The term which simulates the eta peak is constructed from the expected distribution of photon energies for eta decays and a parametrized version of the responses of the shower counters to photons. We use the Monte Carlo efficiency program and a trial differential cross section to generate the expected distribution of photon energies. The background and eta peak terms are adjusted until the sum of the terms best fits the observed $(E_1, E_2)$ spectrum, and the number of etas in the sample is estimated to be the volume of the simulated eta peak. The fitting method is maximum likelihood, modified to compensate for intrinsic bias.

The trial cross section is needed to fix only the shape of the simulated eta peak, since the normalization of that peak is one of the adjustable parameters. The influence of the cross section on the peak shape is small, relative to the energy resolution of the shower counters, and our results are almost independent of reasonable errors in the trial cross section. We explore this point quantitatively in Section 6.10 .

The responses of the shower counters to photons, i.e., the calibration and resolution of each counter, enter in the simulated eta peak as described in Section 3.4. Our parametrization of these responses introduces two calibration factors (one for each counter) and one resolution constant (assumed to be common to both counters). The shower counter responses were measured with the aid of a nearly monoenergetic positron beam (Section 6.3); however, we allow the associated parameters to participate in the search for a maximum likelihood fit to the photoproduction data containing an eta peak. In effect, we independently measure these parameters using the observed eta peak, and the two methods of measurement are in fair agreement for the two calibration factors. However, there is an unmistakeable disagreement for the energy resolution constant: the eta peak in forward photoproduction is less well resolved than we would expect from the results of the electron beam measurements. In Section 3.5 we advance possible reasons for the disagreement; at any rate, the electron beam measurements are not imposed on the problem of fitting the observed eta peak. Wherever it is not feasible to determine the parameters from the fitting, e.g. when the eta peak is overwhelmingly obscured by the background, the parameters are gently "guided" toward values extrapolated from well-determined cases, as described in Section 3.5.

Figures 3.1 through 3.5 depict the elements of the fitting procedure outlined above. Figure 3.1 is the observed $(E_1, E_2)$ spectrum for one experimental setting. Figure 3.2 is the uncorrelated term describing the background, and Figure 3.3 is the

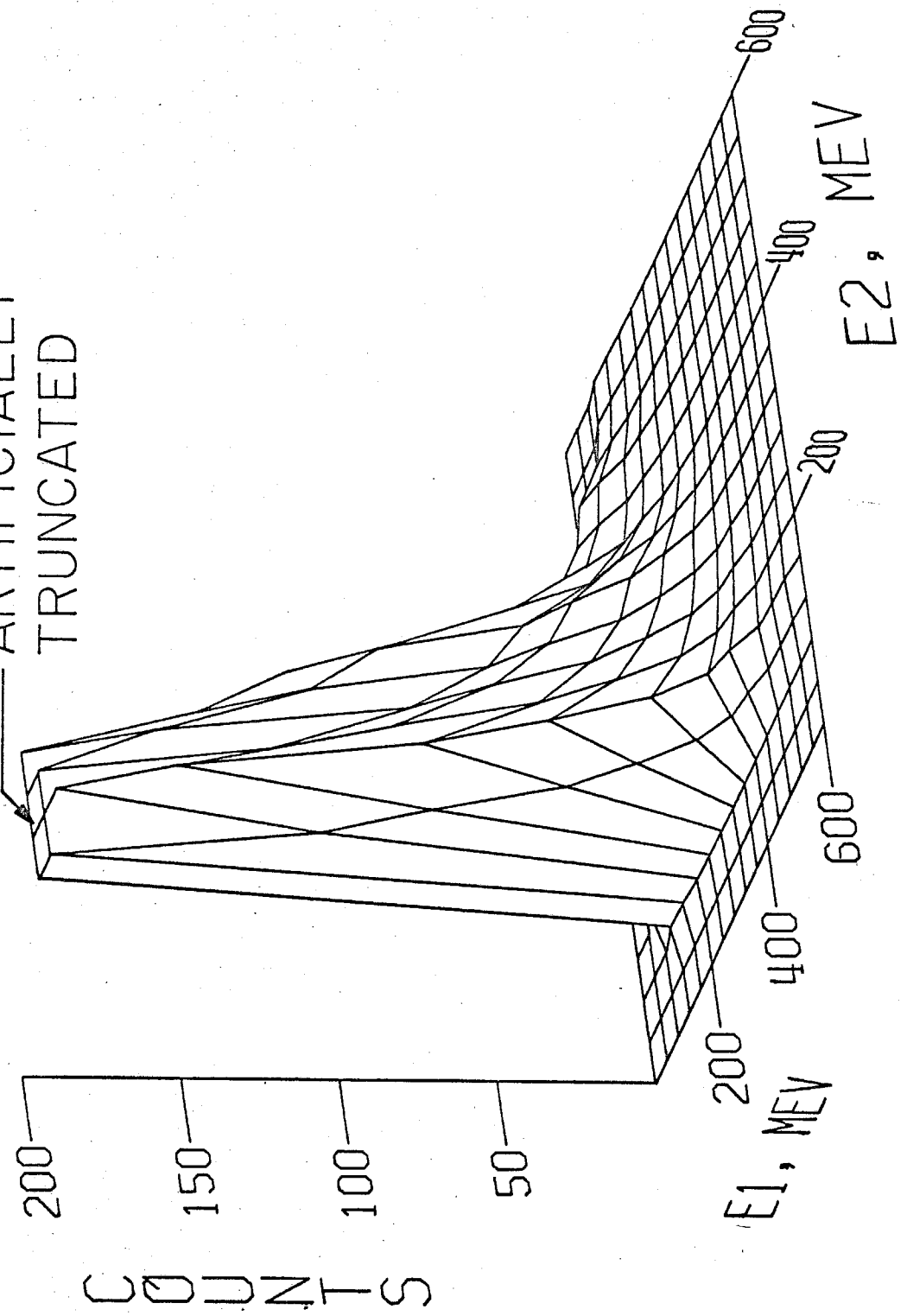


Figure 3.2 $(E_1, E_2)$ Spectrum, Estimated Background

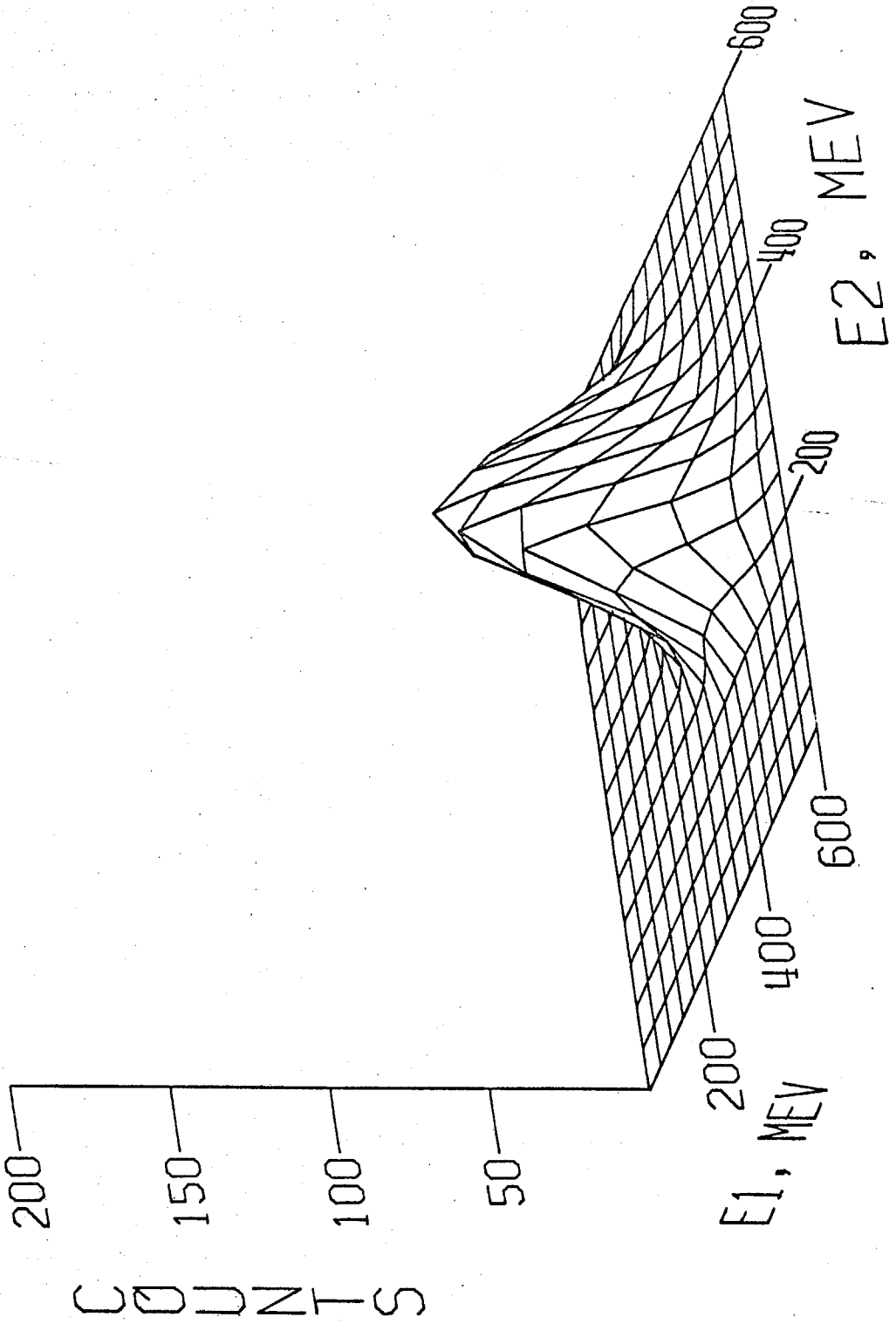


Figure 3.3 $(E_1, E_2)$ Spectrum, Estimated Foreground

simulated eta peak. (Note: The truncation at the 200 counts level, seen in Figures 3.1 and 3.2 , is a feature of the plotting only.) Subtracting the background term from the observed data, Figure 3.2 from 3.1 , produces Figure 3.4 . There we see a series of low energy spikes and, at higher energies, the experimentally observed eta peak. The low energy spikes are located in a region of the $(E_1, E_2)$ plane which was excluded from the fitting (for reasons explained in Section 3.3); the fit has been extrapolated into the omitted region in producing these Figures. Finally, subtracting the simulated eta peak from the observed eta peak, Figure 3.3 from 3.4 , produces 3.5 . The omitted region aside, a good fit is visually indicated by the lack of structure in the residue of Figure 3.5 .

The number of etas for each setting, corrected for empty target contribution and electronic dead time, is converted to an eta yield, i.e., the number of etas per unit of integrated beam energy. Each setting is associated with an eta yield and a resolution function (the detection efficiency as a function of energy and production angle), and the cross section emerges from a study of yields and resolution function over all settings. S. J. Yellin has developed two methods for unfolding the cross section, and both have been applied to this experiment. One method generalizes the notion of endpoint subtraction, and the results appear in the conventional format of a cross section point. The other method, dubbed the "black box" by its perpetrator, fits the cross section to a smooth curve with an unusual set of criteria for the best fit, as explained in Section 3.6 . The output of both methods is displayed in Section 4.

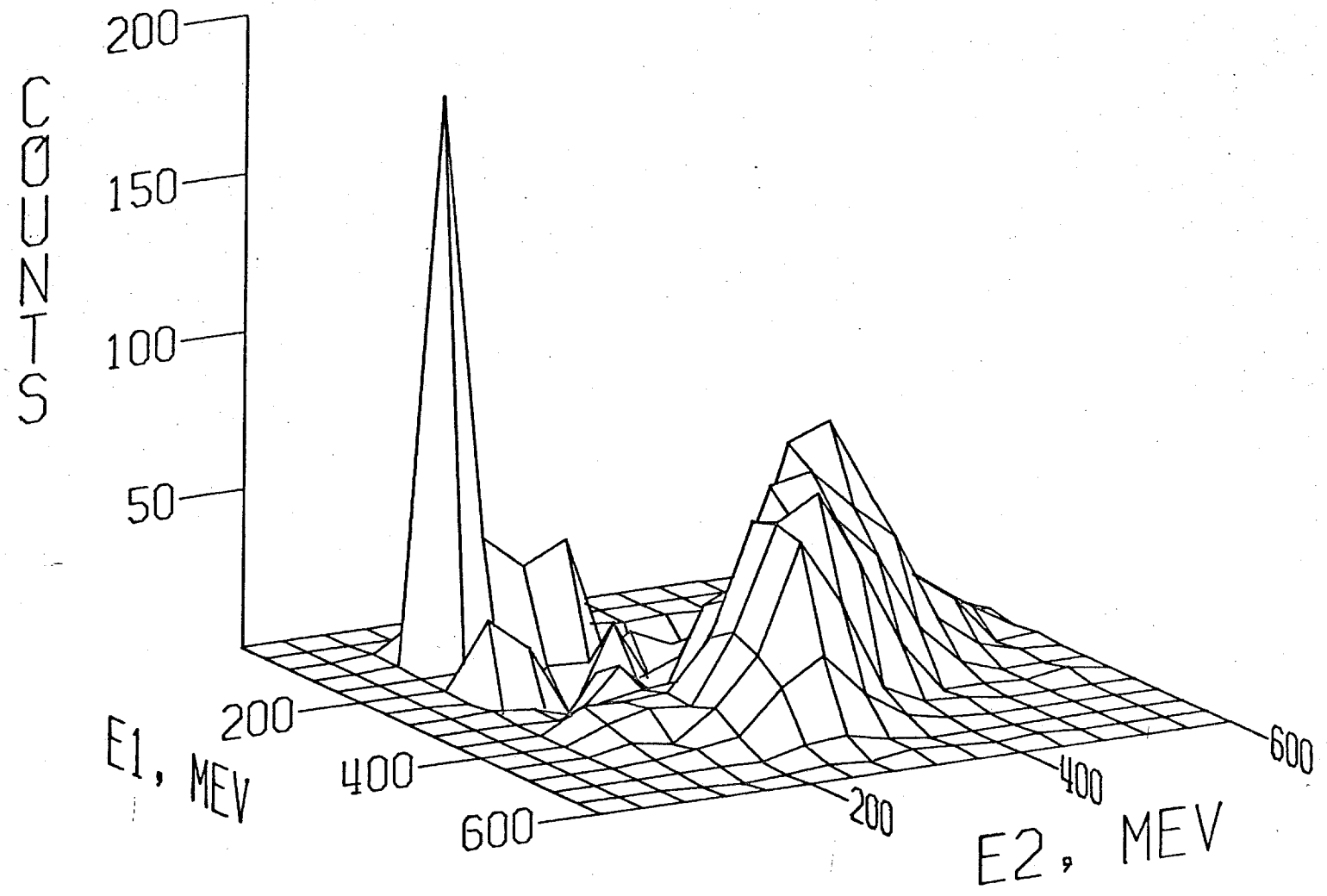


Figure 3.4 $(E_1,E_2)$ Spectrum, All Events Minus Background

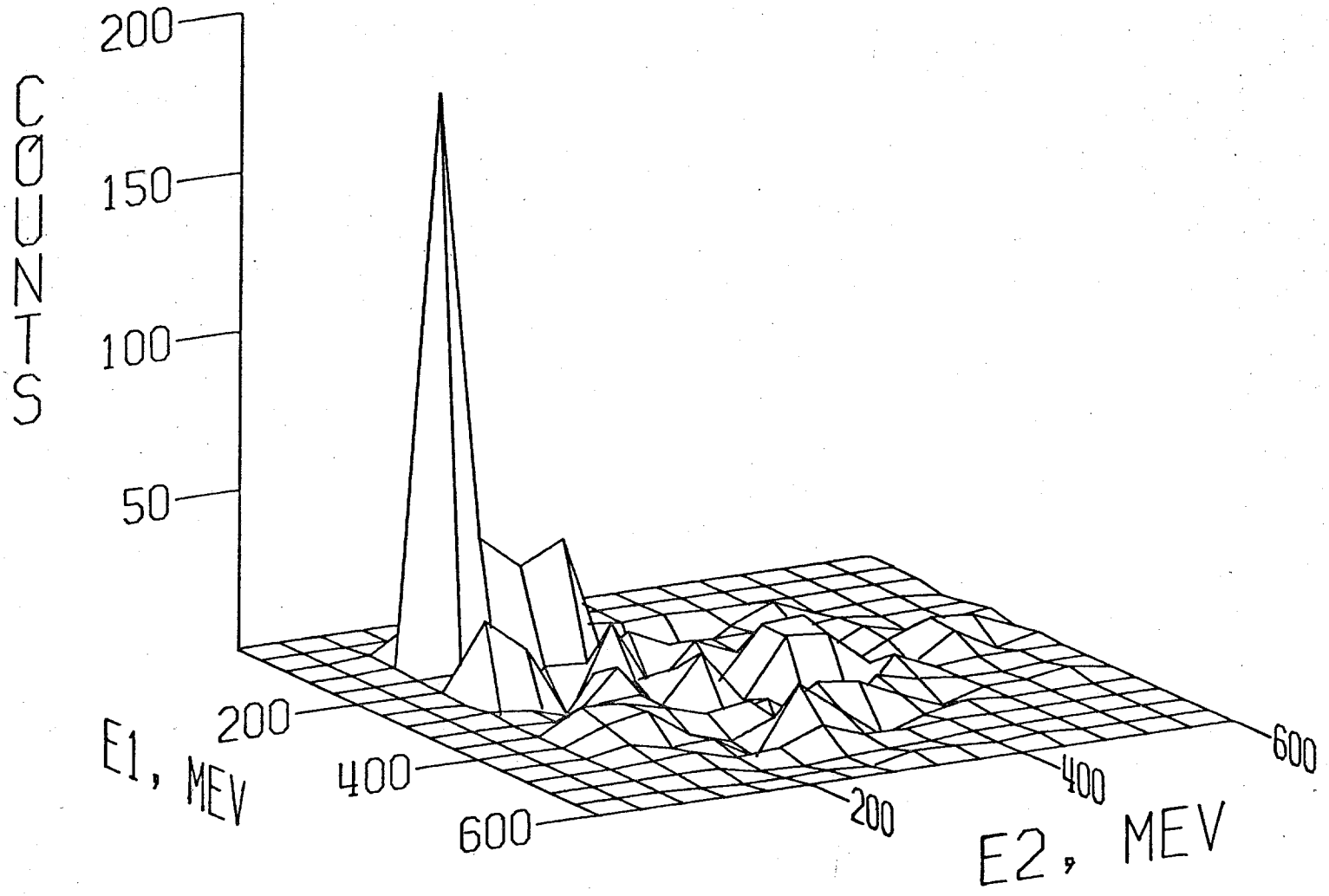


Figure 3.5 $(E_1,E_2)$ Spectrum, All Events Minus Background and Minus Foreground

## 3.2 Preliminary Data Processing

The shower counters produced signals which were pulse height analyzed and digitally recorded on magnetic tape. Denote the digitized pulse heights $e_1$ and $e_2$ for shower counters 1 and 2, respectively, and let $t_{12}$ denote the digitized signal representing the time difference between shower signals. The built-in criteria for an event restricted the range of $t_{12}$ as well as the minimum values for $e_1$ and $e_2$. The Nuclear Data pulse height analyzer determined the maximum values for $e_1$ and $e_2$.

Figure 3.6 shows the $t_{12}$ spectrum (not calibrated in time units), of all events of a representative run. The large peak is due to true coincidences, and the rest of the spectrum is due to accidental coincidences. For an idea of the time scale, the true coincidence peak has a full width at half maximum of 5 ns, and the total range covered is about 40 ns. The smaller peak, above the true coincidence peak and below the cutoff at high $t_{12}$, is only the effect of gross nonlinearity in the $t_{12}$ scale near the upper cutoff.

The ultimate value of the timing information ($t_{12}$) is that we may set a strict coincidence requirement within the data. To this end, it is desirable to optimize the timing resolution. Electronic drift was alleviated by the use of fiducial events, which furnishes a reference point for $t_{12}$ (as well as for $e_1$ and $e_2$). A property of electronic discriminators called "slewing," which causes the timing to depend on the pulse heights involved, had to be considered. We minimized slewing in the hardware by using zero-crossing

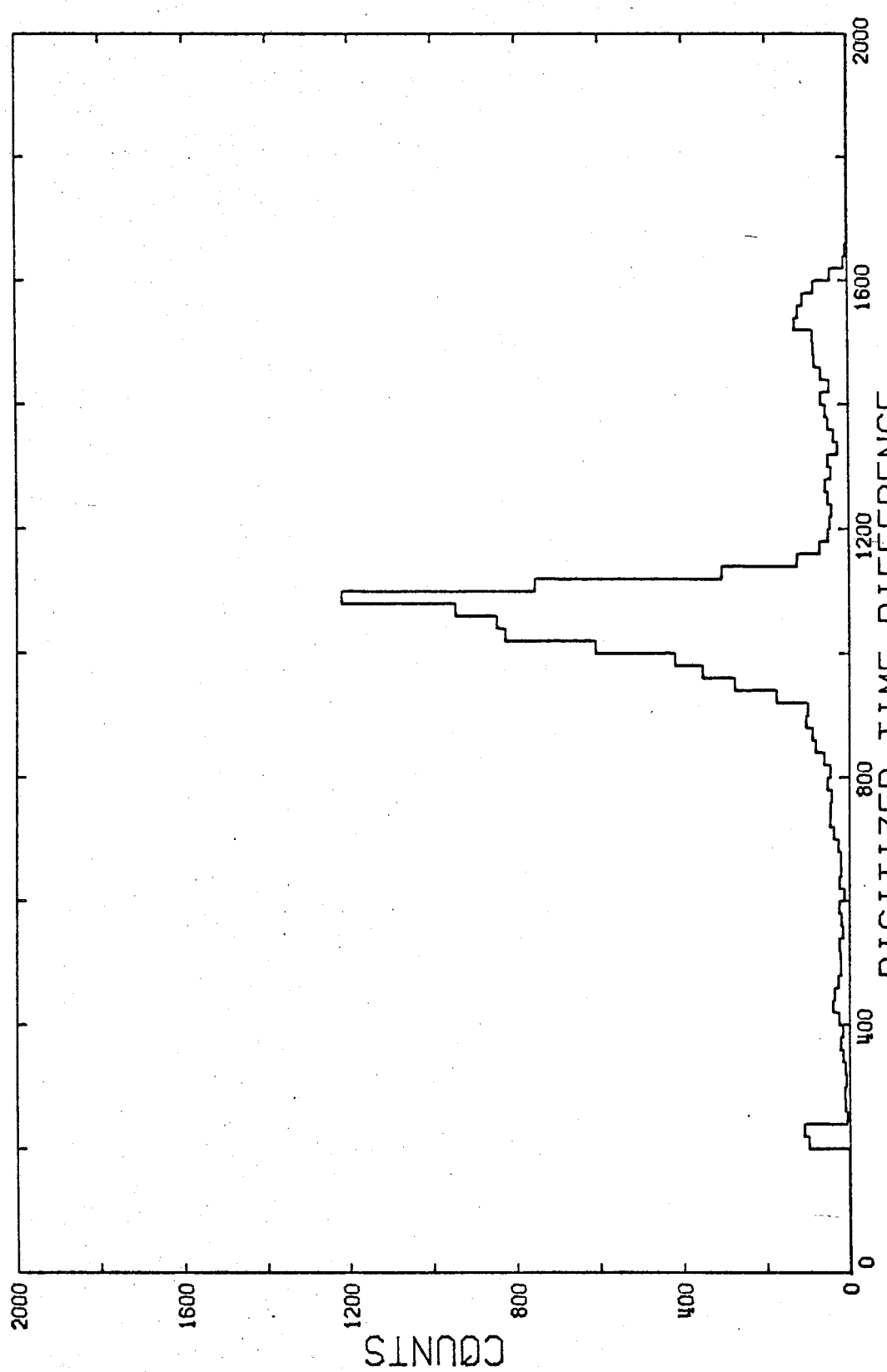


Figure 3.6 Typical Time Difference Spectrum

discriminators[21] at strategic points in the fast logic, labeled "ZCD" in the diagram of Figure 2.2. Additionally, it proved possible to reduce slewing in the data, as described in Section 6.5.

The final coincidence requirement is set on the basis of the eta content of the data. (The procedure for determining eta content is explained in the following Sections, although we mention the results here for the sake of continuity.) We divided the data into several bins in $t_{12}$ and determined the number of eta events in each bin, as seen in Figure 3.7 for one case. The smooth curve is a gaussian fit, and the arrows indicate where the coincidence requirement was set, taken as the points at 6.5 standard deviations from the mean of the gaussian fit. Unless otherwise noted, we assume that only events with $t_{12}$ within that range are under consideration.

Consider the distribution of the shower counter pulse heights $e_1$ and $e_2$. Because the counters are symmetrically oriented about the beam, the spectrum of events in $e_1$ alone is expected to be similar to the spectrum in $e_2$ alone; the discriminator biases may be set at different values, however. At the point where the discriminator first allows signals to pass, there is a rapid rise in the spectrum, as seen for $e_1$ in Figure 3.8 . The spectrum peaks above that point, and where the discriminator finally permits all signals to pass, we see a sharply decreasing spectrum. Eta events appear as a very broad shoulder in this spectrum.

The fiducial events are used to correct $e_1$ and $e_2$ for electronic drift of the kind which changes the calibration by an additive

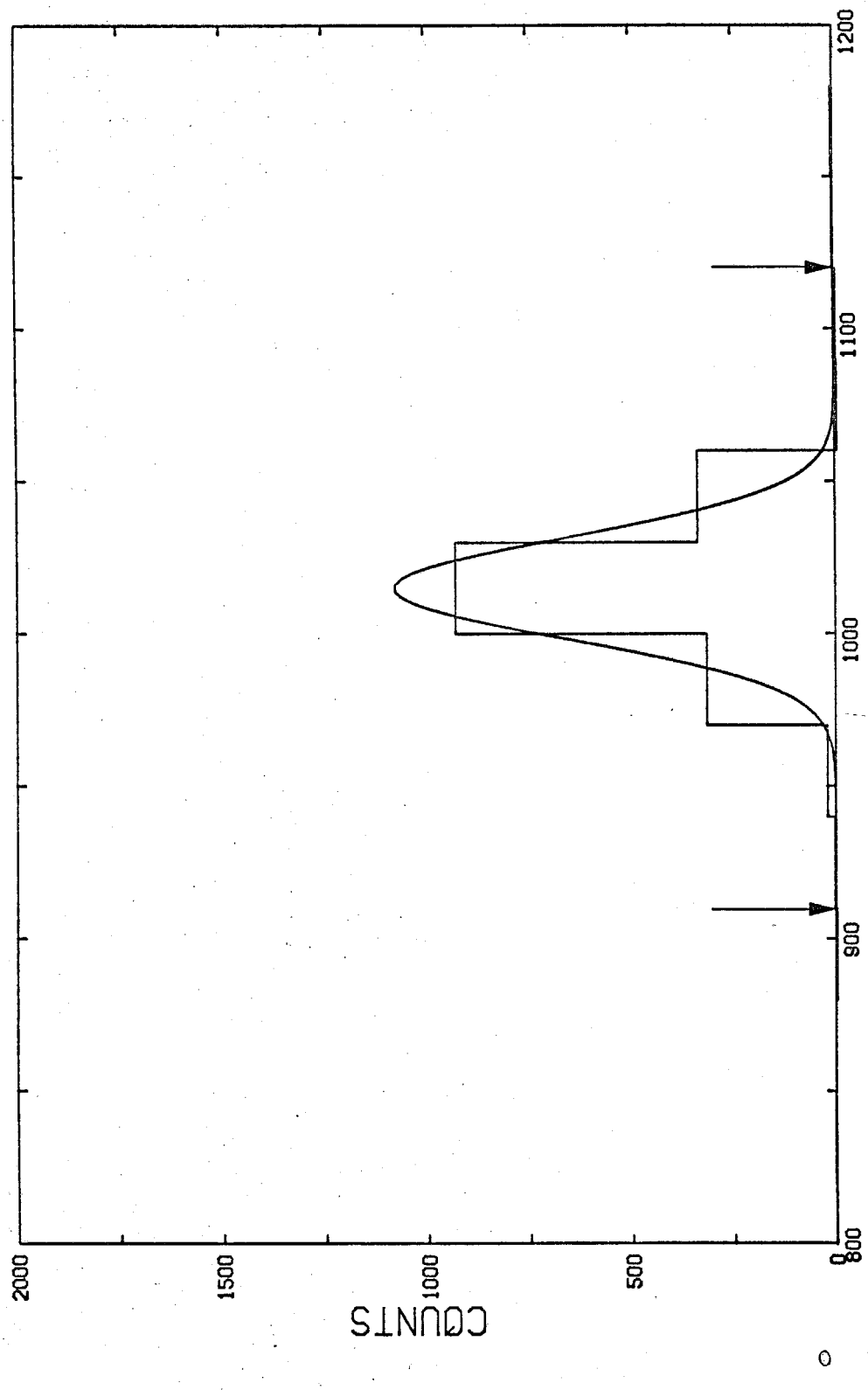


Figure 3.7 Typical Time Difference Spectrum, Eta Events Only

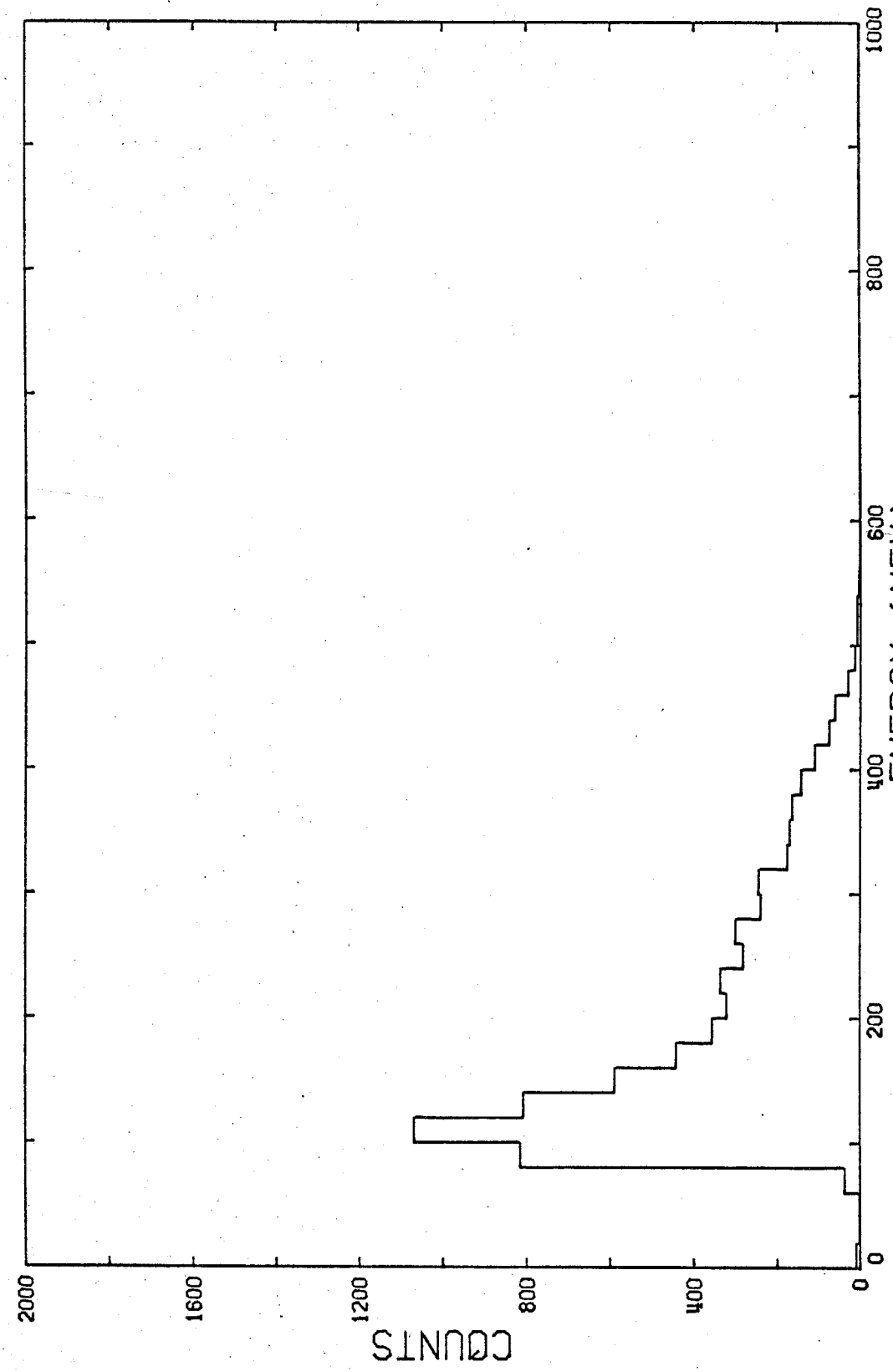


Figure 3.8 Typical Photon Energy Spectrum for One Shower Counter

constant. The scale factor, i.e., the electronic gain, was stable to better than one percent over a day. The pulse height analyzing system is linear to within a few percent, at least over the range of pulse heights finally accepted.

The pulse heights $e_1$ and $e_2$ correspond to shower energies $E_1$ and $E_2$, respectively, although the final calibration depends on the results of fitting the eta peak. The calibration procedure described in Section 6.3A proved inadequate. We were able to improve that procedure by reassigning the equivalent shower energy for each source-scintillator, after making an initial determination of the eta peak parameters (Section 3.5 ). The final calibration is determined by the final values of the eta peak parameters; however, $E_1$ and $E_2$ are assumed to denote the values at the intermediate stage of calibration, i.e., the method of Section 6.3A after source-scintillator energy reassignments.

We have occasion to refer to the invariant mass of the two-photon system, which is calculable from the photon energies, $E_{\gamma 1}$ and $E_{\gamma 2}$, and the opening angle between the photons, $\theta_{\gamma\gamma}$ (all measured in the same frame). The invariant mass, $M_{\gamma\gamma}$, is given by

$$M_{\gamma\gamma} = 2 \sin(\theta_{\gamma\gamma}/2) \sqrt{E_{\gamma 1} E_{\gamma 2}} .$$

For $E_{\gamma 1}$ and $E_{\gamma 2}$ we substitute the measured shower energies $E_1$ and $E_2$, respectively, and for $(\theta_{\gamma\gamma}/2)$ we substitute the counter opening angle $\theta_o$ defined in Section 2. Experimentally, then:

$$M_{\gamma\gamma} = 2 \sin \theta_o \sqrt{E_1 E_2} \quad . \qquad (3.1)$$

Figure 3.9 shows the spectrum of $M_{\gamma\gamma}$, calculated from Equation 3.1 for the same data as appeared in the $e_1$ spectrum of Figure 3.8.

## 3.3 Background Fitting

Consider the distribution of $E_1$ and $E_2$, the measured shower energies for the two photon telescopes. It is in this distribution that we seek to resolve eta events from non-eta or "background" events. We first reduce this distribution to a finite matrix, $N(i_1, i_2)$, where

$$i_1 = \text{integer part of } (E_1/20)$$

$$i_2 = \text{integer part of } (E_2/20) \quad ,$$

for $E_1$ and $E_2$ expressed in MeV. $N(i_1, i_2)$ is the number of counts in the bin labelled by $i_1$ and $i_2$.

Consider the physical processes which might contribute significantly to the structure of N. The process under investigation, eta photoproduction and two-photon eta decay, produces a peak in a region characterized by large values for $i_1$ and $i_2$, on the order of 15. A similar peak at much lower values, on the order of 3, would be seen from

$$\gamma p \rightarrow p\pi^o \quad , \qquad (3.2)$$
$$\hookrightarrow \gamma\gamma$$

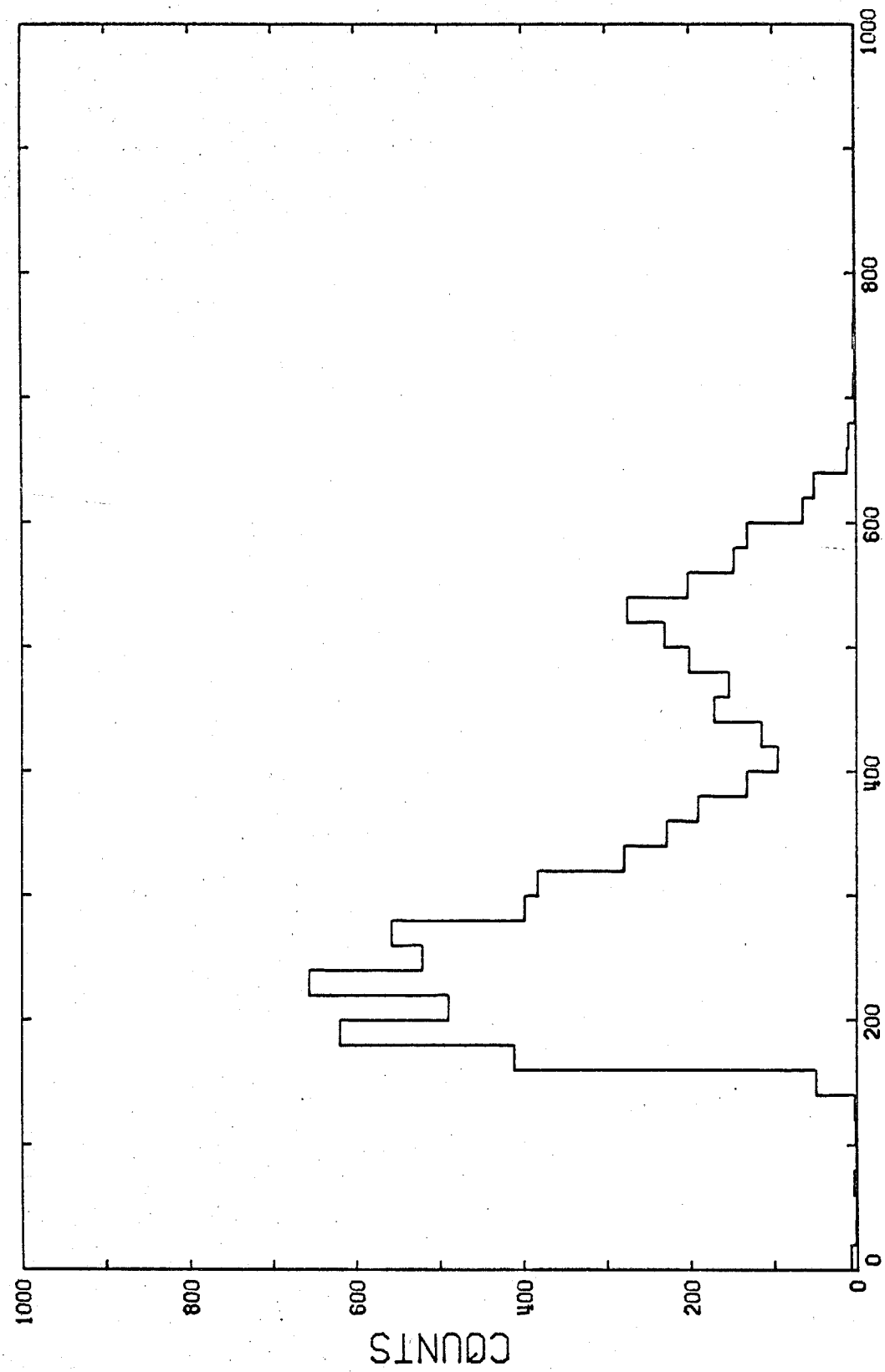


Figure 3.9 Typical Invariant Mass Spectrum

except that biases in the electronics cut off counts for either $i_1$ or $i_2$ less than about 5. Still, a number of such events may have been detected, and in principle we could estimate the expected number from the cross section for (3.2) and the corresponding detection efficiency. In practice, there are some serious uncertainties in the detection efficiency near the energy cutoffs (see Section 6.7). We can only surmise that some events from single $\pi^o$ detection are present where both $i_1$ and $i_2$ are near cutoff. The process dominating the background is believed to be

$$\gamma p \rightarrow p \pi^o \pi^o \quad \begin{matrix} \hookrightarrow \gamma\gamma \\ \hookrightarrow \gamma\gamma \end{matrix} \quad , \qquad (3.3)$$

where each telescope detects only one photon, and the two photons that are detected come from separate $\pi^o$ decays. Because the final state detection for such events is so kinematically incomplete, we expect that $i_1$ and $i_2$ will be relatively independent.

The resonances contributing to reaction (3.3) are of some interest to the background subtraction problem. In particular, we are taking measurements in the region of the $D_{13}(1536)$ and $F_{15}(1688)$, which are highly inelastic resonances with contributions to the reaction $\gamma p \rightarrow p \pi^+ \pi^-$.[36, 37, 38] That reaction is dominated by the formation of the intermediate states $\Delta^{++} \pi^-$, $\Delta^o \pi^+$, and $p \rho^o$ (where $\Delta^o \pi^+$ is suppressed by isospin and possibly dynamical factors). Production of $p \rho^o$ is primarily diffractive, becoming the dominant contribution at higher energies, while $\Delta\pi$ production proceeds via one-pion-exchange (OPE) and via the $D_{13}(1536)$ and $F_{15}(1688)$ resonances

in the direct channel. In the case of $\gamma p \rightarrow p \pi^o \pi^o$, there can be no contribution from either $p \rho^o$ production or OPE production of $\Delta^+ \pi^o$, leaving only resonant production of $\Delta^+ \pi^o$ (plus any non-resonant contribution). It is therefore reasonable to expect a strong energy dependence of the background in this experiment from the otherwise negligible $D_{13}(1536)$ and $F_{15}(1688)$. These states could show up in the cross section results, but only if there is a sizable systematic error in the background subtraction methods. Statistical errors are properly accounted for and propagated through the analysis to the final cross section results. Empirically, the background is roughly a 30% contamination in the vicinity of the eta peak. The subtraction procedure is probably free from systematic error to at least one part in ten, so that the residual background contamination is reduced to a statistically indiscernible level.

Experimentally, the matrix N indeed contains a peak from eta events (see Figure 3.1). However, if eta events are absent, N has no peak except the trivial one resulting from the electronic biases; above the cutoffs, the number of counts decreases with either $i_1$ or $i_2$. Figure 3.10 presents N for a run in which the synchrotron endpoint energy was about 5 MeV below the threshold for eta photoproduction. Close examination of this matrix shows that the shape of the spectrum is decoupled in $i_1$ and $i_2$, except that too many counts appear in the lower left-hand corner, where both $i_1$ and $i_2$

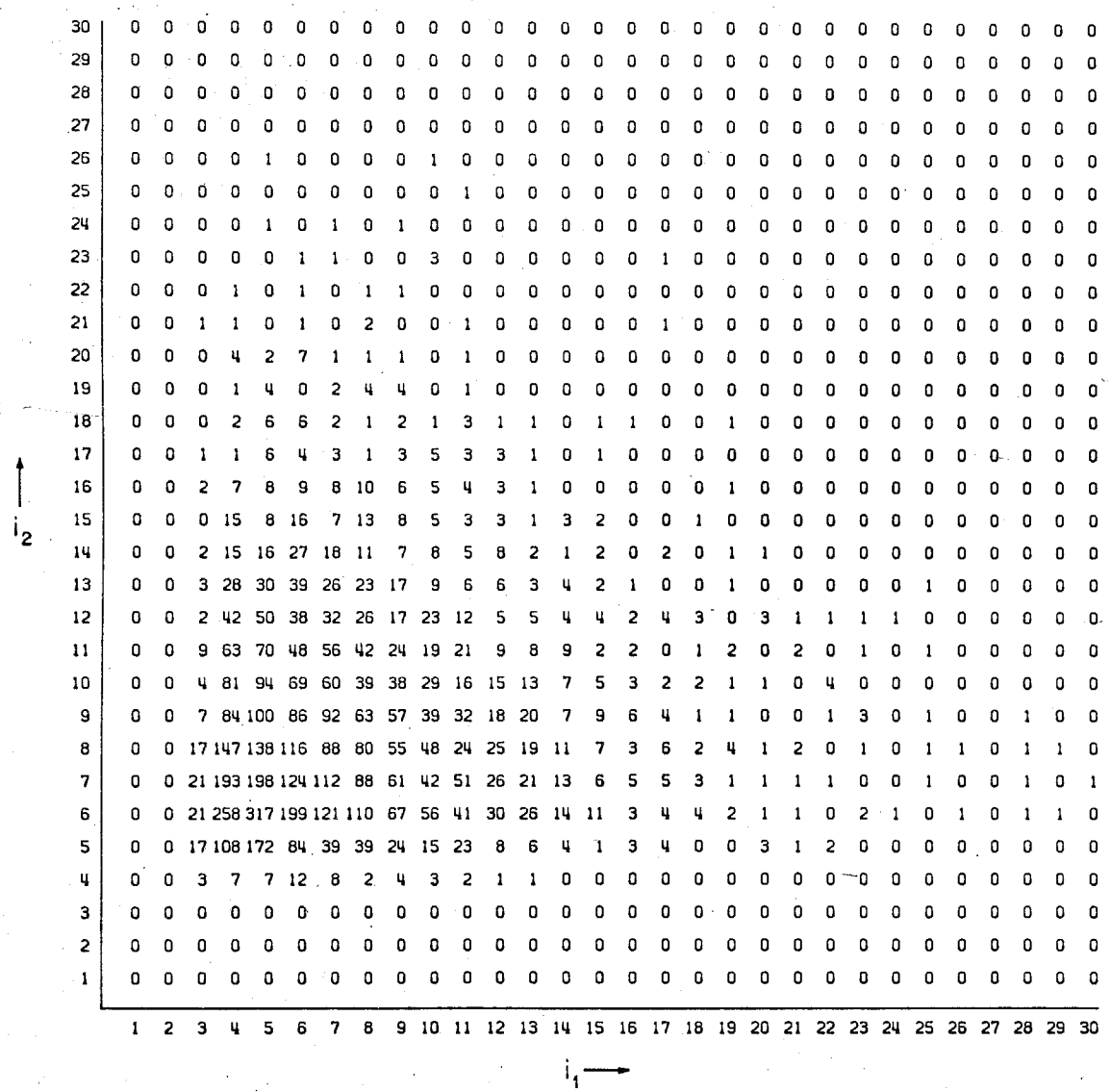


Figure 3.10 The Matrix $N(i_1, i_2)$, All Events of a Below-Threshold Run

are near cutoff. A technique for displaying this structure is introduced below; it forms the nucleus of the background fitting program.

We ascribe the observed decoupling in $i_1$ and $i_2$, for the background, to the predominance of events of the type (3.3). We are less certain about the origin of the observed "enhancement" above the decoupled spectrum where both $i_1$ and $i_2$ are small. The enhancement may be the result of single $\pi^o$ detection, or it may be that the incomplete detection of the 2 $\pi^o$ final state is not as independent in $i_1$ and $i_2$ as supposed -- neither possibility has been systematically investigated. We are able to show, however, that the enhancement is relatively localized, and that a term decoupled in $i_1$ and $i_2$ fits the background well, except in the region of the enhancement, which we therefore exclude from the fitting. What follows is an attempt to show that the enhancement is localizable, at least for the below-threshold data invoked above, after a brief detour to develop a minimal set of mathematical tools.

There is a simple and beautiful technique for "factoring" any spectrum into a product of lower-order spectra and normalizing that product to the parent spectrum. The result, it can be shown, is a maximum likelihood type of fit which is decoupled in the individual variables. For example, let us "factor" $N(i_1, i_2)$ over the set of bins defined by

$$(i_1, i_2) \in R \quad .$$

We call R the "background region." The simplest region is a rectangular block of bins:

$$i_1^L \le i_1 \le i_1^U$$

$$i_2^L \le i_2 \le i_2^U \quad .$$

For a rectangular background region, the factorized fit is written

$$F(i_1, i_2) = T^{-1} N_1(i_1) N_2(i_2)$$

By $N_1(i_1)$, we mean the spectrum of events in $i_1$ alone, for all events within R; similarly for $N_2(i_2)$. T is just the total number of counts in R. Explicitly,

$$N_1(i_1) = \sum_{n=i_2^L}^{i_2^U} N(i_1, n)$$

$$N_2(i_2) = \sum_{m=i_1^L}^{i_1^U} N(m, i_2)$$

$$T = \sum_{m=i_1^L}^{i_1^U} N_1(m) = \sum_{n=i_2^L}^{i_2^U} N_2(n)$$

The matrix F is normalized to N within every row and column independently. Therefore, the difference matrix (N - F) is normalized to zero in every row and column independently. We say that N is "uncorrelated" if (N - F) has no systematic structure.

Suppose that N is the sum of an uncorrelated spectrum and a localized peak. Then (N-F) will be positive in the vicinity of the peak, and elsewhere there will be smaller positive and negative "images" of the peak in order to satisfy the normalization requirement. The pattern in (N-F) will look like:

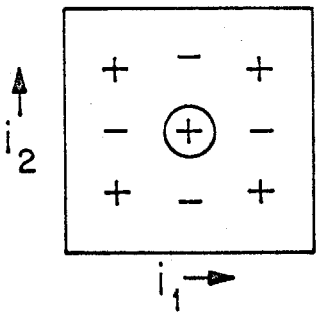


for a peak (circled above) centrally located in the background region. We anticipate a peak in the lower left-hand corner of the background region (above cutoffs), in which case the pattern would look like:

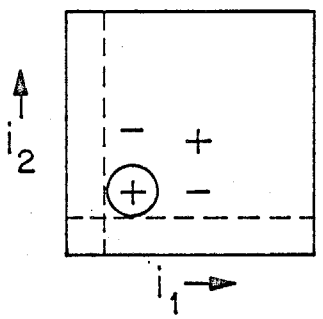


(3.4)

where the dotted lines indicate the cutoffs.

The matrix N displayed in Figure 3.10, for the below-threshold run, produces the pattern (3.4) in (N-F), as seen in Figure 3.11 . Here the background region includes all the bins displayed; of course, only the data above the cutoffs contribute to F. To the extent that (N-F) deviates systematically from zero, it is incorrect to characterize the background as an uncorrelated spectrum. Of greatest concern is the background in the region populated by eta events, when such events are

| $i_2$ \ $i_1$ | 1 | 2 | 3 | 4 | 5 | 6 | 7 | 8 | 9 | 10 | 11 | 12 | 13 | 14 | 15 | 16 | 17 | 18 | 19 | 20 | 21 | 22 | 23 | 24 | 25 | 26 | 27 | 28 | 29 | 30 |
|---|---|---|---|---|---|---|---|---|---|---|---|---|---|---|---|---|---|---|---|---|---|---|---|---|---|---|---|---|---|---|
| 30 | 0 | 0 | 0 | 0 | 0 | 0 | 0 | 0 | 0 | 0 | 0 | 0 | 0 | 0 | 0 | 0 | 0 | 0 | 0 | 0 | 0 | 0 | 0 | 0 | 0 | 0 | 0 | 0 | 0 | 0 |
| 29 | 0 | 0 | 0 | 0 | 0 | 0 | 0 | 0 | 0 | 0 | 0 | 0 | 0 | 0 | 0 | 0 | 0 | 0 | 0 | 0 | 0 | 0 | 0 | 0 | 0 | 0 | 0 | 0 | 0 | 0 |
| 28 | 0 | 0 | 0 | 0 | 0 | 0 | 0 | 0 | 0 | 0 | 0 | 0 | 0 | 0 | 0 | 0 | 0 | 0 | 0 | 0 | 0 | 0 | 0 | 0 | 0 | 0 | 0 | 0 | 0 | 0 |
| 27 | 0 | 0 | 0 | 0 | 0 | 0 | 0 | 0 | 0 | 0 | 0 | 0 | 0 | 0 | 0 | 0 | 0 | 0 | 0 | 0 | 0 | 0 | 0 | 0 | 0 | 0 | 0 | 0 | 0 | 0 |
| 26 | 0 | 0 | 0 | 0 | 1 | 0 | 0 | 0 | 0 | 1 | 0 | 0 | 0 | 0 | 0 | 0 | 0 | 0 | 0 | 0 | 0 | 0 | 0 | 0 | 0 | 0 | 0 | 0 | 0 | 0 |
| 25 | 0 | 0 | 0 | 0 | 0 | 0 | 0 | 0 | 0 | 0 | 1 | 0 | 0 | 0 | 0 | 0 | 0 | 0 | 0 | 0 | 0 | 0 | 0 | 0 | 0 | 0 | 0 | 0 | 0 | 0 |
| 24 | 0 | 0 | 0 | -1 | 0 | 0 | 1 | 0 | 1 | 0 | 0 | 0 | 0 | 0 | 0 | 0 | 0 | 0 | 0 | 0 | 0 | 0 | 0 | 0 | 0 | 0 | 0 | 0 | 0 | 0 |
| 23 | 0 | 0 | 0 | -1 | -1 | 0 | 0 | -1 | 0 | 3 | 0 | 0 | 0 | 0 | 0 | 0 | 1 | 0 | 0 | 0 | 0 | 0 | 0 | 0 | 0 | 0 | 0 | 0 | 0 | 0 |
| 22 | 0 | 0 | 0 | 0 | -1 | 0 | 0 | 1 | 1 | 0 | 0 | 0 | 0 | 0 | 0 | 0 | 0 | 0 | 0 | 0 | 0 | 0 | 0 | 0 | 0 | 0 | 0 | 0 | 0 | 0 |
| 21 | 0 | 0 | 1 | 0 | -1 | 0 | -1 | 1 | 0 | 0 | 1 | 0 | 0 | 0 | 0 | 0 | 1 | 0 | 0 | 0 | 0 | 0 | 0 | 0 | 0 | 0 | 0 | 0 | 0 | 0 |
| 20 | 0 | 0 | 0 | 1 | -1 | 5 | -1 | -1 | 0 | -1 | 0 | 0 | 0 | 0 | 0 | 0 | 0 | 0 | 0 | 0 | 0 | 0 | 0 | 0 | 0 | 0 | 0 | 0 | 0 | 0 |
| 19 | 0 | 0 | 0 | -2 | 1 | -2 | 0 | 3 | 3 | -1 | 0 | 0 | 0 | 0 | 0 | 0 | 0 | 0 | 0 | 0 | 0 | 0 | 0 | 0 | 0 | 0 | 0 | 0 | 0 | 0 |
| 18 | 0 | 0 | -1 | -3 | 0 | 2 | -1 | -2 | 0 | 0 | 2 | 0 | 0 | 0 | 1 | 1 | 0 | 0 | 1 | 0 | 0 | 0 | 0 | 0 | 0 | 0 | 0 | 0 | 0 | 0 |
| 17 | 0 | 0 | 0 | -5 | -1 | -1 | -1 | -2 | 1 | 3 | 2 | 2 | 0 | 0 | 1 | 0 | 0 | 0 | 0 | 0 | 0 | 0 | 0 | 0 | 0 | 0 | 0 | 0 | 0 | 0 |
| 16 | 0 | 0 | 1 | -4 | -5 | 0 | 1 | 4 | 2 | 2 | 1 | 1 | 0 | -1 | -1 | 0 | 0 | 0 | 1 | 0 | 0 | 0 | 0 | 0 | 0 | 0 | 0 | 0 | 0 | 0 |
| 15 | 0 | 0 | -2 | 0 | -9 | 4 | -3 | 5 | 2 | 1 | -1 | 1 | -1 | 2 | 1 | 0 | 0 | 1 | 0 | 0 | 0 | 0 | 0 | 0 | 0 | 0 | 0 | 0 | 0 | 0 |
| 14 | 0 | 0 | 0 | -7 | -10 | 8 | 4 | -1 | -1 | 2 | 0 | 5 | -1 | -1 | 1 | -1 | 1 | 0 | 1 | 1 | 0 | 0 | 0 | 0 | 0 | 0 | 0 | 0 | 0 | 0 |
| 13 | 0 | 0 | -1 | -7 | -10 | 10 | 4 | 5 | 4 | -1 | -2 | 1 | -1 | 1 | 0 | 0 | -1 | -1 | 1 | 0 | 0 | 0 | 0 | 0 | 1 | 0 | 0 | 0 | 0 | 0 |
| 12 | 0 | 0 | -3 | -6 | -6 | -3 | 1 | 1 | -1 | 9 | 1 | -2 | -1 | 0 | 2 | 1 | 2 | 2 | -1 | 2 | 1 | 1 | 1 | 1 | 0 | 0 | 0 | 0 | 0 | 0 |
| 11 | 0 | 0 | 2 | -5 | -9 | -9 | 12 | 6 | -2 | -1 | 5 | -1 | 0 | 4 | -1 | 0 | -2 | 0 | 1 | -1 | 1 | -1 | 0 | 0 | 1 | 0 | 0 | 0 | 0 | 0 |
| 10 | 0 | 0 | -5 | -4 | -4 | -2 | 6 | -5 | 6 | 4 | -4 | 2 | 3 | 1 | 1 | 1 | -1 | 1 | 0 | 0 | -1 | 3 | -1 | 0 | 0 | 0 | 0 | 0 | 0 | 0 |
| 9 | 0 | 0 | -5 | -27 | -29 | -7 | 21 | 5 | 15 | 6 | 6 | 1 | 7 | -1 | 3 | 3 | 1 | -1 | -1 | -1 | -1 | 0 | 2 | 0 | 0 | 0 | 0 | 1 | 0 | 0 |
| 8 | 0 | 0 | 2 | 7 | -24 | -1 | -1 | 7 | 3 | 7 | -9 | 4 | 2 | 1 | 0 | -1 | 2 | 0 | 2 | 0 | 1 | -1 | 0 | 0 | 0 | 1 | 0 | 0 | 1 | 0 |
| 7 | 0 | 0 | 3 | 22 | 0 | -19 | 3 | -2 | -3 | -8 | 11 | 0 | 0 | 1 | -3 | 0 | 0 | 0 | -1 | -1 | 0 | 0 | -1 | 0 | 0 | 0 | 0 | 0 | 0 | 1 |
| 6 | 0 | 0 | -3 | 32 | 54 | 9 | -24 | -9 | -18 | -11 | -12 | -4 | -1 | -2 | 0 | -3 | -3 | 0 | -1 | -1 | -1 | -2 | 0 | 1 | -1 | 1 | 0 | 0 | 1 | 0 |
| 5 | 0 | 0 | 7 | 11 | 60 | 3 | -23 | -12 | -12 | -13 | 0 | -7 | -6 | -3 | -4 | 0 | 1 | -2 | -1 | 2 | 0 | 1 | -1 | 0 | 0 | 0 | 0 | 0 | 0 | 0 |
| 4 | 0 | 0 | 2 | -2 | -3 | 5 | 2 | -3 | 1 | 0 | 0 | 0 | 0 | -1 | 0 | 0 | 0 | 0 | 0 | 0 | 0 | 0 | 0 | 0 | 0 | 0 | 0 | 0 | 0 | 0 |
| 3 | 0 | 0 | 0 | 0 | 0 | 0 | 0 | 0 | 0 | 0 | 0 | 0 | 0 | 0 | 0 | 0 | 0 | 0 | 0 | 0 | 0 | 0 | 0 | 0 | 0 | 0 | 0 | 0 | 0 | 0 |
| 2 | 0 | 0 | 0 | 0 | 0 | 0 | 0 | 0 | 0 | 0 | 0 | 0 | 0 | 0 | 0 | 0 | 0 | 0 | 0 | 0 | 0 | 0 | 0 | 0 | 0 | 0 | 0 | 0 | 0 | 0 |
| 1 | 0 | 0 | 0 | 0 | 0 | 0 | 0 | 0 | 0 | 0 | 0 | 0 | 0 | 0 | 0 | 0 | 0 | 0 | 0 | 0 | 0 | 0 | 0 | 0 | 0 | 0 | 0 | 0 | 0 | 0 |

Figure 3.11 The Matrix $(N-F)(i_1,i_2)$

kinematically allowed. This region is centered at relatively large values of $i_1$ and $i_2$, on the order of 15. From pattern (3.4), observed in Figure 3.11, the background is overestimated in this region. If eta events were present, their number would be underestimated.

Empirically, we observed that the systematic pattern in (N-F) vanishes as the background region is altered so as to exclude events with both $i_1$ and $i_2$ small (near the cutoffs). From studies of this kind, we were led to introduce a mass cut on the background region. For this purpose, we associated a mass to each $(i_1, i_2)$ bin, using Equation 3.1 to express the two-photon invariant mass for an event at the center of that bin. In addition, we excluded events having either $i_1$ or $i_2$ near cutoff, where the detection efficiency is poorly known (Section 6.7).

In order to demonstrate that a mass cut on the background region suffices to eliminate the observed pattern in (N-F), a more sophisticated formalism for generating F is required. This is presented in Section 6.6 ; we may present here the results of applying that formalism to the below-threshold run. Figure 3.12 displays N as before, except that the bins excluded from the background region are indicated as those within the closed border. This is a mass cut of 240 MeV; the resulting (N-F) appears as in Figure 3.13. Note that within the background region, the previous pattern of correlation is not discernible. What appears for (N-F) in the excluded bins has the nature of an extrapolation, since F may be evaluated there (even though the data there did not contribute to F). Pattern (3.4) has become

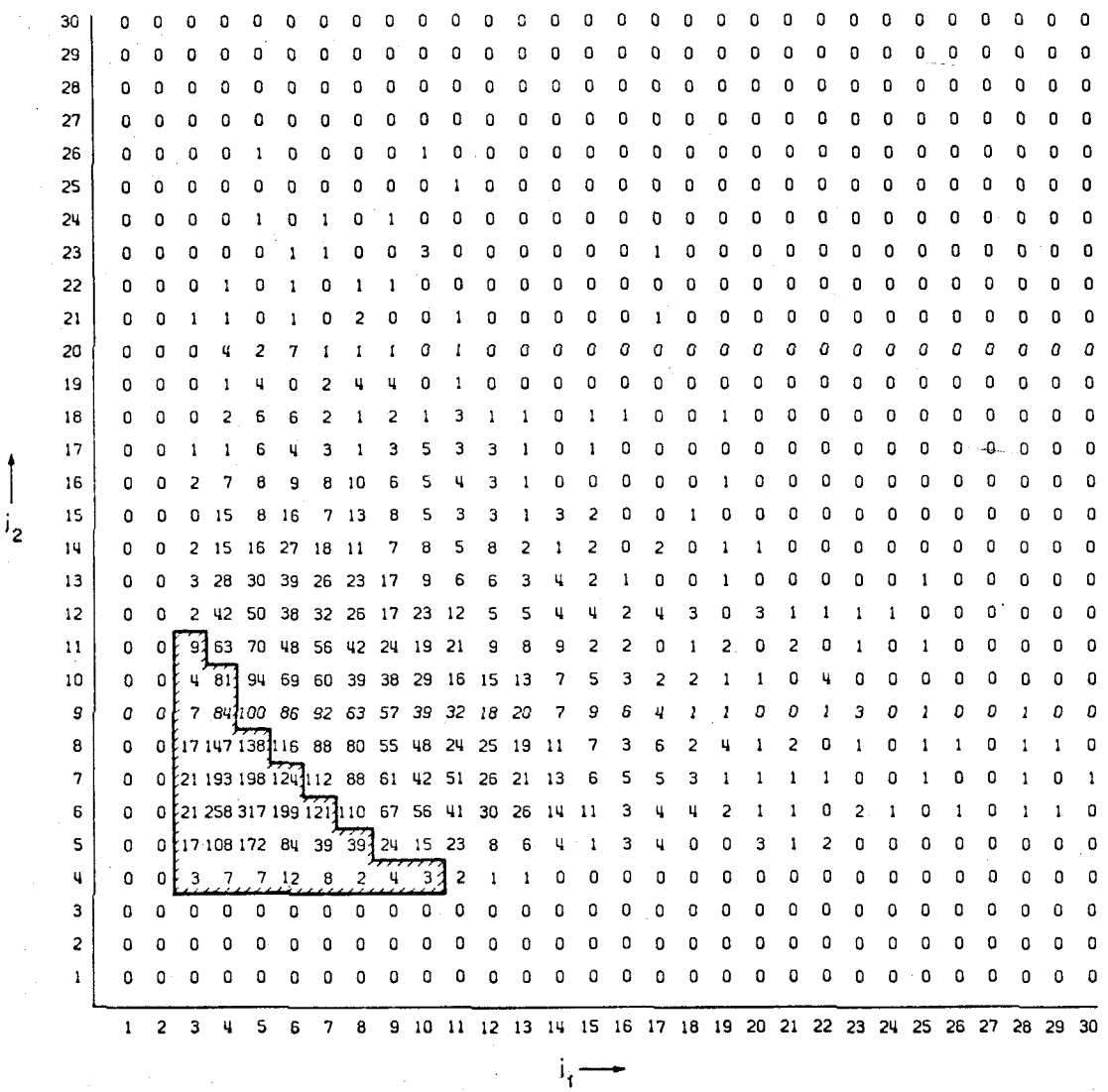


Figure 3.12 The Matrix $N(i_1, i_2)$ With a Mass Cut

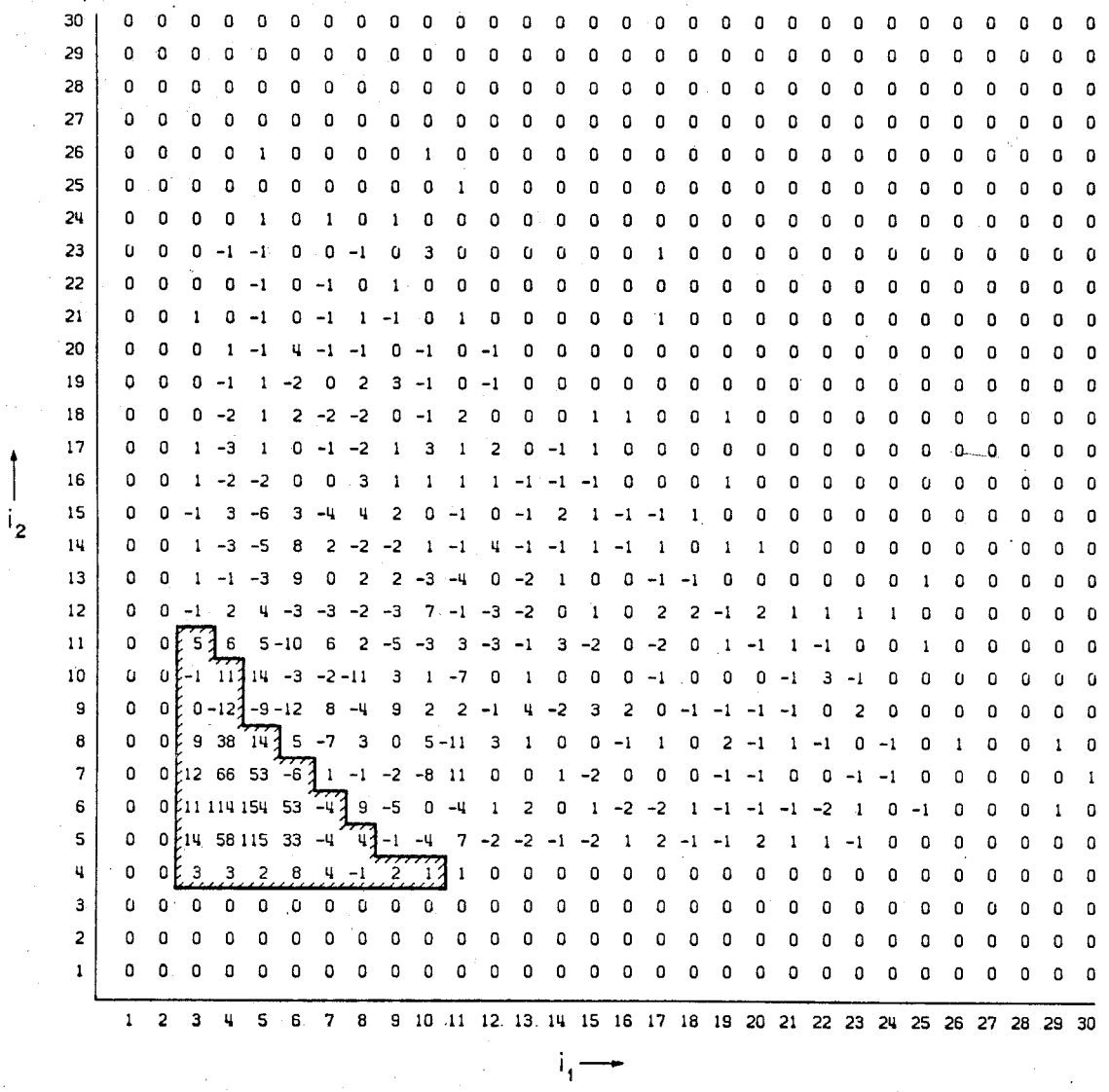


Figure 3.13 The Matrix $(N-F)(i_1, i_2)$ With a Mass Cut

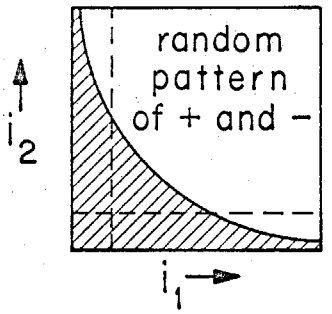


where the excluded region is indicated by shading.

The true test of any background description is in the estimated number of eta events. We return to the background fitting from that point of view in Section 6.10, where the estimated number of etas is examined with respect to reasonable changes in the fitting method, including changes in the boundary of the background region.

The quality of the fit is also informative. All indicators point to the conclusion that the background fitting, as outlined above, is a good description of the background in the vicinity of the eta peak. We turn now to a description of that peak.

## 3.4 Foreground Fitting

A term describing the $(E_1, E_2)$ distribution of eta events, i.e., the foreground, is required in the background fitting, as explained in Section 6.6. The same term also serves to estimate the number of etas, by way of an adjustable normalization parameter. Let $Y(i_1, i_2)$ denote the $(i_1, i_2)$ spectrum of this term, where we suppress writing the normalization parameter. Additional parameters are needed to describe the responses of the shower counters to incident photons. This section outlines the steps in constructing $Y(i_1, i_2)$ from the following ingredients: The Monte Carlo calculation for the detection efficiency, described in Section 6.7 ; a trial differential cross

section; and a parametrized version of the shower counter responses.

The starting point in constructing the matrix Y is a series of simulated eta events produced by the Monte Carlo calculation. Each such event carries the information

$k$ = incident primary photon energy

$\theta^*$ = center-of-mass angle

$E_{\gamma 1}$, $E_{\gamma 2}$ = eta decay photon energies

$\epsilon$ = statistical weight of event (detection efficiency).

There is an important distinction between the actual photon energies, $E_{\gamma 1}$ and $E_{\gamma 2}$, and the measured shower energies, $E_1$ and $E_2$. By analogy with the binned quantities $i_1$ and $i_2$, define

$i_{\gamma 1}$ = integer part of $(E_{\gamma 1}/20)$

and $i_{\gamma 2}$ = integer part of $(E_{\gamma 2}/20)$,

for $E_{\gamma 1}$ and $E_{\gamma 2}$ expressed in MeV. The expected number of events described by indices $i_{\gamma 1}$ and $i_{\gamma 2}$, denoted $Y_\gamma(i_{\gamma 1}, i_{\gamma 2})$, is calculable from

$$Y_\gamma(i_{\gamma 1}, i_{\gamma 2}) = C \int d\Omega \int_{k_o}^{E_o} dk \; \frac{d\sigma}{d\Omega}(k, \theta^*)\, N_\gamma(k, E_o)\, \epsilon(k, \theta^*; i_{\gamma 1}, i_{\gamma 2})$$

where $d\sigma/d\Omega$ = trial differential cross section

$N_\gamma$ = primary photon energy spectrum

$k_o$ = threshold energy ($\sim$.7 GeV)

$E_o$ = synchrotron endpoint energy

$C$ = constant

For a trial cross section, we chose a term with a "flat" $\theta^*$ dependence and a k dependence which roughly follows the world data for the cross section. As shown in Section 6.10, our final results are not strongly dependent on the exact form of this term. (Our methods are in principle not dependent on a prior knowledge of the cross section, because we might have "bootstrapped" the cross section by an iterative technique, requiring the output to be consistent with the input.)

Consider the distribution of the shower energies, $E_1$ and $E_2$, produced by eta decays constrained to have fixed values for $E_{\gamma 1}$ and $E_{\gamma 2}$. If $E_1$ and $E_2$ were perfectly calibrated quantities, their mean values would be $E_{\gamma 1}$ and $E_{\gamma 2}$, respectively. The factors $k_1$ and $k_2$ are introduced to describe a possible calibration error, as follows:

$$k_1\langle E_1\rangle = E_{\gamma 1}$$

$$k_2\langle E_2\rangle = E_{\gamma 2} \ .$$

We assume that the variances of $E_1$ and $E_2$ scale directly with energy, and we write (see Section 6.3B):

$$k_e\, k_1^2\, \sigma^2(E_1) = E_{\gamma 1}$$

$$k_e\, k_2^2\, \sigma^2(E_2) = E_{\gamma 2} \ ,$$

where we assume that one resolution factor, $k_e$, suffices to describe both counters. (In reality, the two counters were nearly matched in resolution.) The $(E_1, E_2)$ spectrum, denoted $Y(E_1, E_2)$, will have the form

$$Y(E_1,E_2) = \exp\left\{-\tfrac{1}{2}\left[(E_1-\langle E_1\rangle)^2/\sigma^2(E_1) + (E_2-\langle E_2\rangle)^2/\sigma^2(E_2)\right]\right\}$$

$$= \exp\left\{-\tfrac{1}{2}\, k_e\left[(k_1E_1 - E_{\gamma 1})^2/E_{\gamma 1} + (k_2E_2 - E_{\gamma 2})^2/E_{\gamma 2}\right]\right\} \quad ,$$

temporarily suppressing the question of normalization. In terms of energy-binned quantities,

$$Y(i_1,i_2) = \exp\left\{-\tfrac{1}{2}\, k_e\left[(k_1i_1 - i_{\gamma 1})^2/i_{\gamma 1} + (k_2i_2 - i_{\gamma 2})^2/i_{\gamma 2}\right]\right\} \quad .$$

This is the expected $(i_1, i_2)$ spectrum produced by eta events characterized by fixed values of $i_{\gamma 1}$ and $i_{\gamma 2}$. For eta events with $i_{\gamma 1}$ and $i_{\gamma 2}$ distributed in the spectrum $Y_\gamma(i_{\gamma 1}, i_{\gamma 2})$, the expected $(i_1, i_2)$ spectrum is

$$Y(i_1,i_2) = K \sum_{i_{\gamma 1}, i_{\gamma 2}} Y_\gamma(i_{\gamma 1},i_{\gamma 2})$$

$$\times \exp\left\{-\tfrac{1}{2}\, k_e\left[(k_1i_1 - i_{\gamma 1})^2/i_{\gamma 1} + (k_2i_2 - i_{\gamma 2})^2/i_{\gamma 2}\right]\right\} \quad , \qquad (3.5)$$

where K is a normalization factor. Denote the volume under Y, i.e., the number of eta events, by $T_\eta$ . K is then given by

$$K = T_\eta k_1 k_2 k_e / \left(2\pi \sum_{i_{\gamma 1}, i_{\gamma 2}} Y_\gamma(i_{\gamma 1},i_{\gamma 2}) \sqrt{i_{\gamma 1}\, i_{\gamma 2}}\right) \quad . \qquad (3.6)$$

Eqs. 3.5 and 3.6 express $Y(i_1, i_2)$ in terms of the Monte Carlo spectrum $Y_\gamma(i_{\gamma 1}, i_{\gamma 2})$ and the four parameters $T_\eta$, $k_1$, $k_2$, and $k_e$. The goal of the foreground and background fitting is to determine $T_\eta$, while the parameters $k_1$, $k_2$, and $k_e$ are quantities associated with the calibration and resolution of the shower counters. We find that the calibration and resolution measurements described in Section 6.3 are in conflict with the best values of $k_1$, $k_2$, and $k_e$ which emerge from the fitting program discussed in Section 3.5 . Faced with this conflict, we allow the best values of the fitting program to stand; in effect, we measure $k_1$, $k_2$, and $k_e$ from the experimental distribution of eta events.

## 3.5 Combined Background and Foreground Fitting

The background is described by an uncorrelated spectrum, $F_1(i_1)\ F_2(i_2)$, and the foreground is described by the Monte Carlo simulated eta peak, $Y(i_1, i_2; T_\eta, k_1, k_2, k_e)$. The sum of these two terms is used to describe the matrix of counts, $N(i_1, i_2)$, where the free parameters are $T_\eta$, $k_1$, $k_2$, $k_e$, and each element of the vectors $F_1$ and $F_2$. The strictly correct fitting method would vary all these free parameters simultaneously, but we divide the fitting into two parts: we determine the background parameters with the foreground parameters held fixed, and vice versa. We alternate between background fitting and foreground fitting, using the results of one as input for the other, until further iterations lead to an acceptable level of change in the estimated number of eta events, $T_\eta$. This

Section is a discussion of that fitting program, including the correction for intrinsic bias and the need for occasional external guidance of the fitting parameters.

Section 6.6 presents the mathematical details of a maximum likelihood determination of the background when the fitting model is

$$F(i_1,i_2) = F_1(i_1)F_2(i_2) + Y(i_1,i_2; T_\eta,k_1,k_2,k_e) \quad ,$$

where Y is considered a constant term. This fit applies to a certain set of $(i_1, i_2)$ bins called the "background region," R. This region is chosen so as to exclude events of too low invariant mass as well as those near the $i_1$ and $i_2$ cutoffs, as described previously in Section 3.3 . We now introduce an "eta cut" on R, i.e., we exclude from R events in the immediate vicinity of the eta peak. The background is necessarily an extrapolation within the excluded part. This provides a degree of separation of the background and foreground fitting problems, which is desirable from any of several viewpoints. For one, the background determination is less influenced by errors in the foreground description; for another, the background term is not given an opportunity to participate in describing eta events. The convergence of our two-part fitting method is also more rapid and definite with an eta cut on R. In the following sketch, R is the unshaded region of the $(i_1, i_2)$ plane:

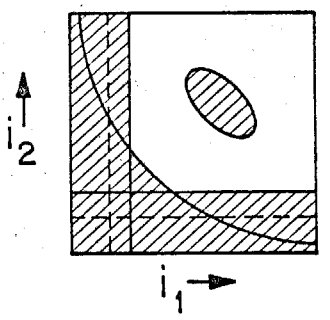


The boundary of the eta cut was fixed on the basis of the matrix Y, i.e., the simulated eta peak, after an initial determination of the free parameters in Y. The bins in the eta cut are those for which the value of Y is more than 20% of its maximum value, with one exception: certain bins located just above the boundary of R and parallel to it, were reserved to R even if the value of Y there was more than 20% maximum. (This was necessary to avoid the background indeterminacy problem mentioned in Section 6.6 .)

The eta peak parameters, $T_\eta$, $k_1$, $k_2$, and $k_e$ are determined using a computer program called SOLVE.[23] This is a minimum chi-squared fitting package, although our usage converts it to a maximum likelihood fitting program. For this problem, the background is considered a constant term, and the fitting is confined to a set of bins that we call the "eta region," denoted $R_\eta$. We fixed the boundary of $R_\eta$ using the 10% level line of Y, with no exception made for any bins reserved to R. In most cases, there was a sufficiently clear eta peak in the spectrum $N(i_1, i_2)$ that the eta peak parameters could be determined without difficulty. Recall that $k_1$ and $k_2$ are associated with the energy calibration of shower counters 1 and 2, respectively. Referring to Section 6.3A, $k_1$ and $k_2$ may be considered correction factors for the energy calibration of the corresponding Bi-207 Auger

electron peak in the scintillator spectrum ($E_S$). An initial determination of $k_1$ and $k_2$ was the basis for a reassignment of those source-scintillator equivalent shower energies. In succeeding passes, $k_1$ and $k_2$ were determined to be near unity to within 5% for most runs, and no subsequent recalibration was performed. The energy calibration, since it is locally corrected within each run via $k_1$ and $k_2$, may differ from run to run. However, we desired an approximate calibration in order to calculate the invariant mass from $E_1$ and $E_2$, for the purpose of applying the mass cut to the background region.

The parameter $k_e$ is associated with the energy resolution, assumed to be identical for each shower counter. From Section 6.3B, using the positron beam, $k_e$ is expected to be near 0.35 $MeV^{-1}$ for either counter. From the fitting, using the methods described above, the best value for $k_e$ was not constant from run to run, but rather it showed a variation with the shower counter opening angle. This variation ranged from about 0.15 at an opening angle of $40^\circ$ to 0.25 at $90^\circ$, with typical statistical errors of 0.03. This is at variance with the notion that $k_e$ is a constant, and the discrepancy with the positron beam value is particularly severe for small counter opening angles. This indicates that the energy resolution is not as good as expected from phototube statistics alone, although we are at a loss to pinpoint the source of the additional fluctuations. Of all mechanisms considered to explain this situation, the most plausible was that soft photons were sufficiently abundant that the phototube signals were contaminated with an almost continuous noise. (This

hypothesis could have been easily checked during the experiment, had we known of the problem.) The dependence on shower counter opening angle is seen, in this view, to be connected more with the counting rates than with the geometry of the counters. A superficial study, however, revealed no evidence for a counting rate dependence of $k_e$ for a given counter geometry. In any case, we do not impose the positron beam measurements on $k_e$, since the data quite definitely indicate the inapplicability of those measurements in the fitting problem. In Section 6.10, we describe a test which indicates that a negligible error is made by letting $k_e$ describe an additional broadening of the eta peak beyond that expected from phototube statistics alone.

The eta peak was occasionally so obscured by the background that the SOLVE program was unable to determine values for the eta peak parameters. When this occurred, we manually intervened by "guiding" SOLVE toward plausible values of the parameters. This, of course, amounts to biasing the outcome, although the alternative is to abandon the data, which is unacceptable. We adopted a scheme which applies an adjustable degree of pressure on the parameters to converge toward predetermined values. For each parameter, we add an extra artificial point. For that point, the parameter itself is required to fit its predetermined value, subject to a predetermined weighting factor. That weighting factor, which controls the pressure, was chosen on the basis of how well the parameter in question was determined from other runs.

The intrinsic bias of the fitting method, apart from the deliberate bias described above, had to be considered. In general, a fit will be biased if the free parameters do not enter linearly. Our conception of a fitting "bias" is the following. The experimental data determine a fit. That fit may be used to generate artificial data at the same points as the experimental data, if the form of the statistical fluctuations are known (e.g., Poisson statistics). The artificial data may then be fitted. On the average, the fit to the artificial data will differ from the fit to the experimental data, which constitutes a bias. This definition lends itself to a computer method for bias compensation. For our work, however, the bias was compensated using an approximate analytical expression developed by S. J. Yellin[5]. The expression gave that the number of etas, $T_\eta$, was overestimated by typically 0.5%. Similarly, $k_1$ and $k_2$ were wrongly estimated by a negligible amount, but $k_e$ was overestimated by around 5% in most cases. The latter is analogous to the systematic error in estimating the variance of a distribution, when one divides the sum of the squared deviations by N rather than by (N-1), where N is the number in the distribution.

## 3.6 Cross Section Evaluation

The following is an outline of the steps leading from the estimated number of eta events to the cross section. Sub-Section A relates the cross section to the eta "yield," which is defined as the number of eta events produced by one unit of integrated photon energy

from the primary beam. Two different paths to the cross section, both of them developed by S. J. Yellin, are described in Sub-Sections B and C, and the results appear in Section 4.

When the incident photon energy, k, is not well resolved, as in this experiment, it is conventional to extricate the cross section using the well-known technique of endpoint subtraction. The method of Sub-Section B is an extension of that technique, in which the geometry of the photon telescopes, characterized by the beam-to-telescope angle, is considered on an equal footing with the synchrotron endpoint energy. The output of such a program is the cross section at more or less localized values of k and $\theta^*$, where $\theta^*$ is the eta center of mass production angle.

Sub-Section C describes a fit to the cross section, parameterized as a smooth function of k and a finite power series in $(\cos \theta^*)$. This method has the disadvantage that the cross section is not measured at separated points in k and $\theta^*$, but it is more powerful in measuring the $(\cos \theta^*)$ moments of the cross section.

The calibration of the synchrotron endpoint energy is important to any evaluation of the cross section which uses the data produced by this experiment. Since there existed conflicting measurements of the energy calibration constant for the Caltech synchrotron, we attempted to resolve that question using data taken just above threshold: This had to be done prior to fitting all the data. Section 6.9 describes that program in more detail.

A. General Considerations

For each experimental run, the estimated number of eta events has been produced using the previously described background-foreground fitting program. We convert this number to an eta yield, dividing by the total beam energy for the run, using the beam monitoring system described in Section 6.1. The individual eta yields are then corrected for electronic dead time and empty target contribution, as described in Section 6.8 . Finally, we combine the eta yields for runs which had the same experimental configuration, producing the experimental eta yield, $Y_\eta^{exp}$ , for each distinct configuration. This quantity bears a statistical weight, described by the standard deviation, $\sigma_\eta^{exp}$ , which uses the results of the foreground fitting package SOLVE.

Associated with each $Y_\eta^{exp}$ and $\sigma_\eta^{exp}$ is a <u>resolution function</u>, R, defined as

$$R\ (k,\ \theta^*;\ E_o,\ \theta_o) \ =\ \Gamma\ N_p N_\gamma(k,E_o)\ \epsilon(k,\ \theta^*;\ E_o,\ \theta_o)$$

where

$E_o$ = synchrotron endpoint energy

$\theta_o$ = angle between beam line and either photon telescope

$\Gamma$ = branching ratio for $(\eta \rightarrow \gamma\gamma)/(\eta \rightarrow \text{all}) = 0.375 \pm 0.016$ [20]

$N_p$ = number of protons per unit area in target

$N_\gamma$ = density of incident photons in k , normalized to one unit of integrated beam energy

$\epsilon$ = detection efficiency.

The detection efficiency calculation is outlined in Section 6.7, and the bremsstrahlung photon energy spectrum is calculated using the computer program BPAK I, written by F. B. Wolverton.[22] From the cross section and the resolution function, we may calculate the expected value of the eta yield, $Y_\eta^{calc}$, corresponding to the values of $E_o$ and $\theta_o$. That calculation uses the relationship

$$Y_\eta^{calc} = 2\pi \int_{-1}^{+1} d(\cos\theta^*) \int_{k_o}^{E_o} dk \, \frac{d\sigma}{d\Omega}(k,\theta^*) \, R(k,\theta^*; E_o, \theta_o) , \tag{3.7}$$

where

$\frac{d\sigma}{d\Omega}$ = differential cross section

$k_o$ = threshold energy in k .

The comparison between $Y_\eta^{calc}$ and $Y_\eta^{exp}$, over all experimental configurations (labelled by $E_o$ and $\theta_o$), is the basis for extricating the cross section. This would be a simple operation if the resolution function were sharply localized in k and $\theta^*$. While the $\theta^*$ localization is good (on the basis of the typical rate of change of the cross section in $\theta^*$), the k localization is not sufficiently favorable for a point-by-point extraction of the cross section. One approach to this problem is to take linear combinations of the $Y_\eta^{calc}$ expression, Eq. 3.7, with respect to the various experimental configurations. Certain linear combinations of the resolution functions will be well localized in k, and the cross section may then sensibly be taken outside the integrand in Eq. 3.7. As might be expected, the number of

useful linear combinations is less than the number of experimental configurations. This approach is described in Sub-Section B below. Alternatively, $Y_\eta^{calc}$ may be compared with $Y_\eta^{exp}$ using a parameterized cross section in Eq. 3.7 , and the cross section measurement becomes a fitting problem: This is the approach of Sub-Section C.

B. Method of Linear Combinations

We take linear combinations of the relation for $Y_\eta^{calc}$, Eq. 3.7, with respect to the various experimental configurations labelled by $E_o$ and $\theta_o$. In the endpoint subtraction technique, one takes linear combinations with respect to the synchrotron endpoint, $E_o$; we extend that technique to include $\theta_o$. For convenience, denote an experimental configuration by the index i instead of by $E_o$ and $\theta_o$. Then the eta yields comprise a vector with respect to i, denoted $\vec{Y}_\eta^{exp}$ and $\vec{Y}_\eta^{calc}$, and similarly for the resolution functions, $\vec{R}$. Expressing the coefficients of the linear combination by the vector $\vec{a}$, we have that

$$\vec{a}\cdot\vec{Y}_\eta^{calc} = 2\pi \int_{-1}^{+1} d(\cos\theta^*) \int_{k_o}^{E_o} dk \, \frac{d\sigma}{d\Omega}(k, \theta^*)\, \vec{a}\cdot\vec{R}(k,\theta^*) \, .$$

Define the cross section, averaged over the resolution function $\vec{a}\cdot\vec{R}$ by $\langle d\sigma/d\Omega \rangle_{\vec{a}}$ . Then

$$\left\langle \frac{d\sigma}{d\Omega} \right\rangle_{\vec{a}} = \frac{\vec{a}\cdot\vec{Y}_\eta^{calc}}{2\pi \int_{-1}^{+1} d(\cos\theta^*) \int_{k_o}^{E_o} \vec{a}\cdot\vec{R}(k,\theta^*)} \, . \qquad (3.8)$$

One replaces $\vec{Y}_{\eta}^{calc}$ by $\vec{Y}_{\eta}^{exp}$ in Eq. 3.8 in order to measure the cross section.

The theory for optimizing the resolution by manipulating $\vec{a}$ has been developed by S. J. Yellin and embodied in a computer program called BLUBOX.[5] That program was applied independently to two subsets of the data, defined by whether eta production was localized to $0^{\circ}$ or $180^{\circ}$, with some overlap for the data which were not well localized in $\theta^*$. The results are shown in Section 4.

C. Method of Parametrization

As an alternative to localizing the cross section measurement in k and $\theta^*$, one may parametrize the cross section in those variables and seek a good fit between the calculated and experimental yields. We take the following parametrization for the cross section:

$$\frac{d\sigma}{d\Omega}(k, \theta^*) = \sum_{n=0}^{M} \sigma_n(k) \cos^n\theta^* \quad .$$

The functions $\sigma_n(k)$ are determined by the exotic criteria described below. We are primarily interested in the first ($\cos\theta^*$) moment of the cross section, since that moment is a measure of the interference between S and P waves (see Section 5). Thus, our primary interest is in determining $\sigma_o(k)$ and $\sigma_1(k)$ for the cross section parametrized by

$$\frac{d\sigma}{d\Omega}(k, \theta^*) = \sigma_o(k) + \sigma_1(k) \cos\theta^* \quad .$$

For this form, we can define a cross section asymmetry

$$A(k) = \frac{\frac{d\sigma}{d\Omega}(k,0^o) - \frac{d\sigma}{d\Omega}(k, 180^o)}{\frac{d\sigma}{d\Omega}(k,0^o) + \frac{d\sigma}{d\Omega}(k, 180^o)} = \frac{\sigma_1(k)}{\sigma_o(k)} \quad .$$

One would like reasonably smooth functions of k for the cross section. Intuitively, a function is "smooth" if its second derivative is small in absolute value. Consider the functional $I(d\sigma/d\Omega)$, defined by

$$I(\frac{d\sigma}{d\Omega}) \equiv \int d\Omega \int_{k_o}^{k_1} dk \left[\frac{\partial^2}{\partial k^2} \frac{d\sigma}{d\Omega}(k,\Omega)\right]^2 ,$$

where $k_o$ is the threshold energy and $k_1$ is the highest endpoint energy used in the experiment. The absolute minimum of this functional is zero, which occurs when $(d\sigma/d\Omega)$ is linear in k. Suppose, however, that $(d\sigma/d\Omega)$ is required to satisfy some constraint in terms of the calculated eta yields; the minimization of I may not be so trivial in that case. A natural type of constraint is one in terms of chi-squared, which is written

$$\chi^2 = \sum_i \left[\frac{(Y_\eta^{exp} - Y_\eta^{calc})^2}{(\sigma_\eta^{exp})^2}\right]_i ,$$

where the index i labels the experimental configurations. The fitting program BLKBOX (for "Black Box"), written by S. J. Yellin,[5] minimizes I with respect to $(d\sigma/d\Omega)$, subject to the constraint $\chi^2$ = constant. In the calculus of variations, those criteria suffice to determine $(d\sigma/d\Omega)$ uniquely. The only arbitrary parameter is the constant to

which the value of $\chi^2$ is constrained, denoted C. One might expect that a reasonable choice for C is the number of degrees of freedom in the fit, but that number is not well defined for this fitting method. There is no unambiguous rule by which to choose C; one must simply examine a family of solutions for various C. There is an informative tradeoff between C and the value of I. The solution behaves more erratically as a function of k when C is small. At the other extreme, the solution becomes linear in k for a certain value of C, and higher values of C cannot be reached. The results of using this fitting program on the experimental data, using the cross section parametrization described above, are shown in Section 4.

# 4. RESULTS

Two different methods for evaluating the cross section were introduced in Section 3.6. The results are presented in this Section, although it is seen that the "method of parametrization" is somewhat unsatisfactory in its present formulation. From attempts to salvage that potentially more powerful method, the cross section results are also presented in a hybrid form which borrows from both the "method of parametrization" and the "method of linear combinations."

Table 4.1 presents the results from the method of linear combinations. As mentioned in Section 3.6B, this method was applied separately to two subsets of the experimental data, determined according to whether eta production was predominantly in the forward or backward directions, hence the "forward" and "backward" categories in Table 4.1. (The method might have been generalized to simultaneously measure the sum and difference of the forward and backward cross sections, however.)

It should be stressed that the cross section values of Table 4.1 are weighted averages of those cross section values obtainable from the individual measurements of the eta yield. It is therefore statistically possible for the reported value to be negative, which actually occurs in the case of the point for forward production near 970 MeV. The error on that point, however, makes the reported value easily consistent with a small positive value for the physical cross section. The reported errors are from the diagonal elements of the

TABLE 4.1

CROSS SECTION FOR FORWARD AND BACKWARD PHOTOPRODUCTION

Forward

| $\langle k \rangle$ (MeV) | $\Delta k$ (MeV) | $\langle \cos \theta^* \rangle$ | $\Delta \cos \theta^*$ | $\frac{d\sigma}{d\Omega}$ ($\mu$b/sr) | $\Delta \frac{d\sigma}{d\Omega}$ ($\mu$b/sr) | $(\frac{d\sigma}{d\Omega})_{\gamma\gamma}$ ($\mu$b/sr) | $\Delta(\frac{d\sigma}{d\Omega})_{\gamma\gamma}$ ($\mu$b/sr) |
|---|---|---|---|---|---|---|---|
| 722 | 10 | 0.02 | 0.52 | 0.76 | 0.02 | 0.285 | 0.008 |
| 743 | 6 | 0.74 | 0.19 | 0.77 | 0.04 | 0.289 | 0.015 |
| 773 | 16 | 0.79 | 0.19 | 1.04 | 0.05 | 0.390 | 0.019 |
| 805 | 13 | 0.87 | 0.13 | 1.02 | 0.05 | 0.383 | 0.019 |
| 841 | 22 | 0.91 | 0.09 | 0.77 | 0.09 | 0.289 | 0.034 |
| 883 | 21 | 0.94 | 0.07 | 0.53 | 0.05 | 0.199 | 0.019 |
| 971 | 31 | 0.86 | 0.14 | -0.04 | 0.07 | -0.015 | 0.026 |

TABLE 4.1 (continued)

CROSS SECTION FOR FORWARD AND BACKWARD PHOTOPRODUCTION

Backward

| $\langle k \rangle$ (MeV) | $\Delta k$ (MeV) | $\langle \cos \theta^* \rangle$ | $\Delta \cos \theta^*$ | $\frac{d\sigma}{d\Omega}$ (μb/sr) | $\Delta \frac{d\sigma}{d\Omega}$ (μb/sr) | $(\frac{d\sigma}{d\Omega})_{\gamma\gamma}$ (μb/sr) | $\Delta(\frac{d\sigma}{d\Omega})_{\gamma\gamma}$ (μb/sr) |
|---|---|---|---|---|---|---|---|
| 721 | 7 | 0.13 | 0.49 | 0.72 | 0.02 | 0.270 | 0.008 |
| 743 | 8 | -0.73 | 0.20 | 0.89 | 0.05 | 0.334 | 0.019 |
| 771 | 11 | -0.77 | 0.17 | 0.92 | 0.08 | 0.345 | 0.030 |
| 809 | 24 | -0.80 | 0.17 | 1.07 | 0.11 | 0.401 | 0.041 |
| 843 | 30 | -0.91 | 0.06 | 1.21 | 0.09 | 0.454 | 0.034 |
| 985 | 65 | -0.92 | 0.05 | 0.35 | 0.03 | 0.131 | 0.011 |

covariance matrix, which we do not present here. The errors do not reflect any of the possible systematic effects discussed in Section 6.10. We return to the question of systematic uncertainties near the conclusion of this Section.

The cross section evaluation makes use of the branching ratio for eta decay into two photons, taken as 0.375±0.16 from reference 20. For convenience, we also tabulate the cross section with this factor suppressed; this entry of Table 4.1 is denoted $(\frac{d\sigma}{d\Omega})_{\gamma\gamma}$ . Other entries in Table 4.1 are the mean values of the photon energy and cos $\theta^*$, where $\theta^*$ is the center-of-mass eta production angle, along with the errors on both quantities. These, of course, refer to linear combinations of the resolution in the various experimental configurations, corresponding to the particular weighted average reported as the cross section.

The cross section points in Table 4.1 are displayed in Figure 4.1, where the smooth curves will be explained below. The "forward" points are labelled $\sigma$ $(0^o)$, with the understanding that although the experimental resolution peaks at $0^o$, the average value of $\theta^*$ will be greater than $0^o$, with similar comments for the "backward" points. Table 4.1 lists the average values for cos $\theta^*$. Note that only the top of the error flag appears for the "forward" point near 970 MeV, since the central value of that point is negative.

In the method of parametrization, the cross section is parametrized as

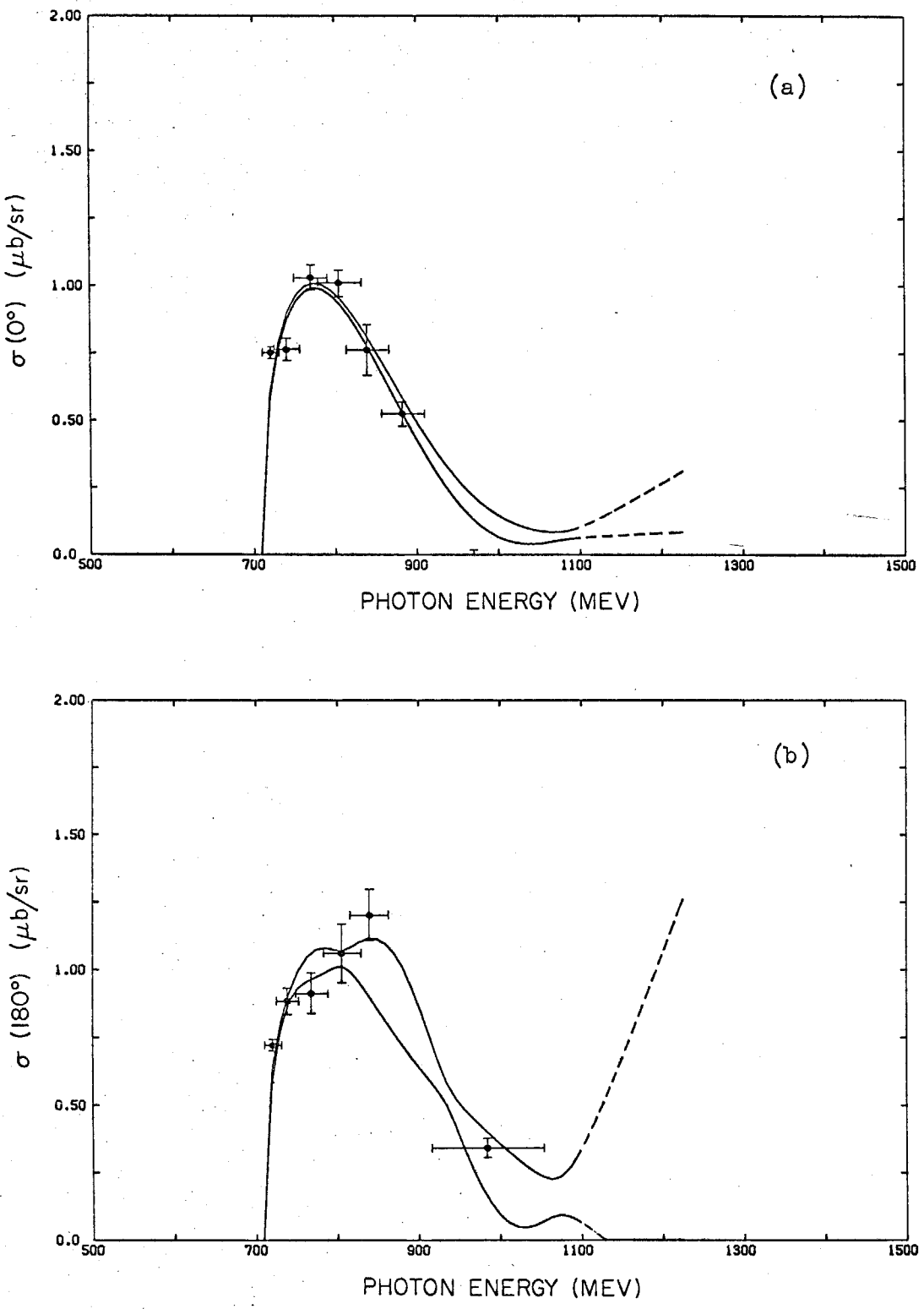


Figure 4.1 Cross Section for (a) Forward and (b) Backward Photoproduction.

$$\frac{d\sigma}{d\Omega}(k, \Theta^*) = \sigma_o(k) + \sigma_1(k) \cos \Theta^* \qquad (4.1)$$

where k is the photon energy and $\Theta^*$ is the center-of-mass eta production angle. We actually determine $\sigma_o(k)$ and $\sigma_1(k)$ with the threshold factor $(q^*/k^*)$ factored out, where $q^*$ and $k^*$ are, respectively, the center-of-mass momenta of the eta meson and incident photon. This relieves the fitting program from describing the rapid energy variation of the cross section near threshold, concentrating instead on the energy dependence of the squared amplitude. When the cross section is parametrized as above, the experimental eta yield data are not separated into "forward" and "backward" categories. If, however, the cross section were parametrized as simply $\sigma_o(k)$, then such a separation would be necessary in order to measure the forward and backward cross sections independently, just as in the method of linear combinations. When we apply the simple $\sigma_o(k)$ parametrization to the same "forward" and "backward" data which went into the method of linear combinations, then we obtain the solutions for $\sigma_o(k)$ shown in Figure 4.1 by the smooth curves. Each pair of curves represents the "error envelope" of the corresponding solution. The "forward" and "backward" solutions are seen to be in fairly good agreement with the discrete cross section points which emerge from the method of linear combinations. The error envelopes are represented by dashed lines above 1100 MeV to indicate that the physical measurements of the cross section do not sensibly extend into that region.

Returning to the parametrization (4.1), $\sigma_o(k)$ and $\sigma_1(k)$ have

been determined for a family of values for $\chi^2$. (As explained in Section 3.6C, one does not know unequivocally what value to take for $\chi^2$, since the number of degrees of freedom is undefined for this fitting method.) For 24 linear combinations of the experimental data (not to be confused with those of the method of linear combinations), the value of $\chi^2$ has been fixed variously at 60, 20, and 4 to obtain the solutions displayed in Figures 4.2, 4.3, and 4.4 respectively. In those figures, the scales for $\sigma_o(k)$ and $\sigma_1(k)$ are labelled $\frac{1}{2}(\sigma(0^o) + \sigma(180^o))$ and $\frac{1}{2}(\sigma(0^o) - \sigma(180^o))$ respectively.

Several points will be noted about the solutions for $\sigma_o(k)$ and $\sigma_1(k)$. There are effectively 24 "points" being fitted, and there is an unspecified but presumably positive number of degrees of freedom. The case of $\chi^2 = 60$ represents a weak $\chi^2$ constraint, and the resulting solutions, Figure 4.2, are relatively smooth functions of photon energy. For $\chi^2 = 20$, the solutions shown in Figure 4.3 fit the experimental data better at the expense of smoothness. The solutions for $\chi^2 = 4$, Figure 4.4, fit the experimental data even better, but the energy dependence is wildly erratic. Although the solutions for $\chi^2 = 20$ are probably closer to the ideal fit in terms of $\chi^2$ per degree of freedom, we feel that the solutions for $\chi^2 = 60$ more reliably estimate the physical cross section.

The solutions have been permitted to assume physically meaningless negative values for the cross section. In the case of the solutions for $\chi^2 = 60$, this occurs in the vicinity of 1000 MeV. This did not occur for the separate "forward" and "backward" solutions

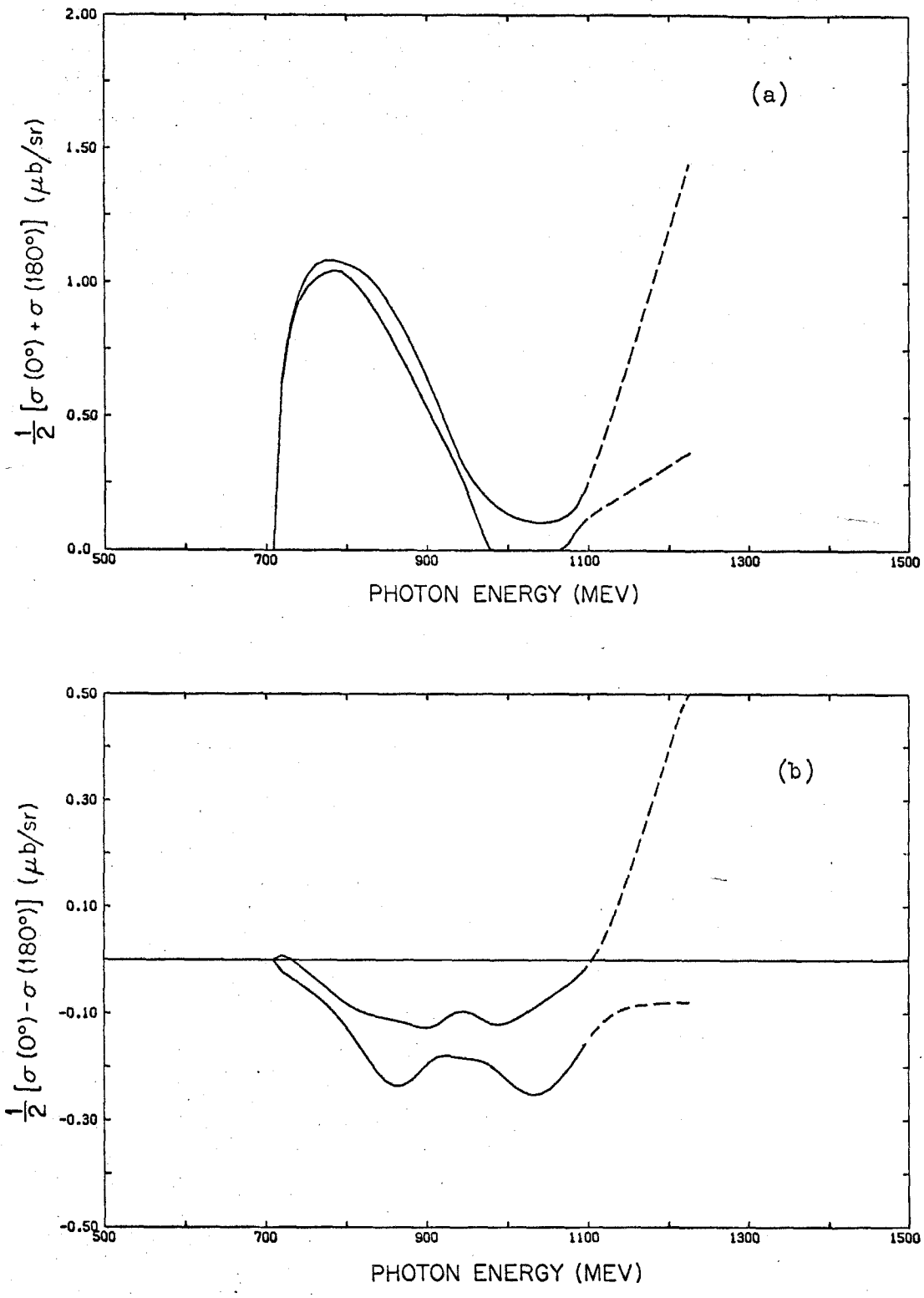


Figure 4.2 Error Envelope of (a) $\sigma_o(k)$ and (b) $\sigma_1(k)$, $\chi^2 = 60$.

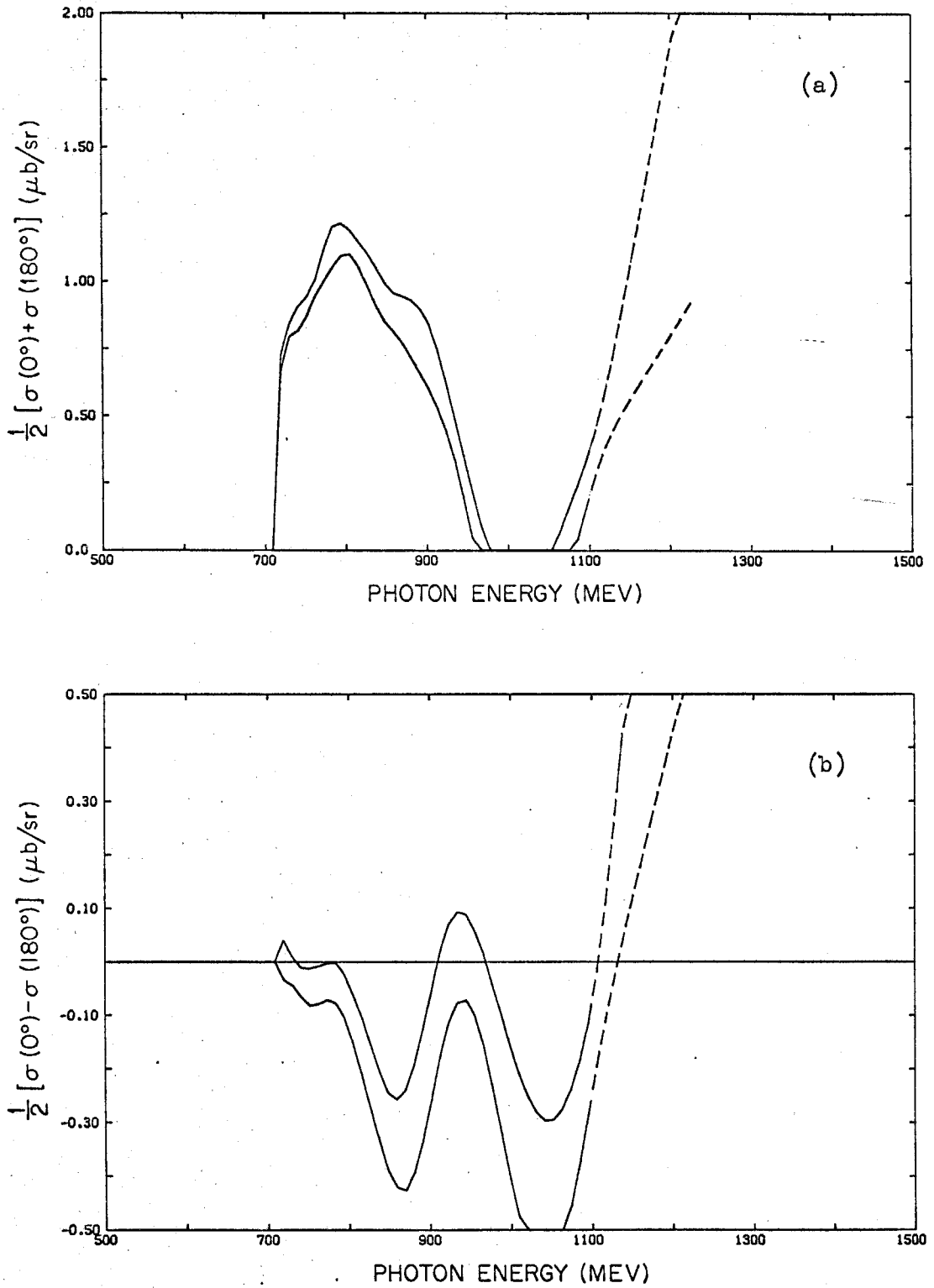


Figure 4.3 Error Envelope of (a) $\sigma_o(k)$ and (b) $\sigma_1(k)$, $\chi^2 = 20$.

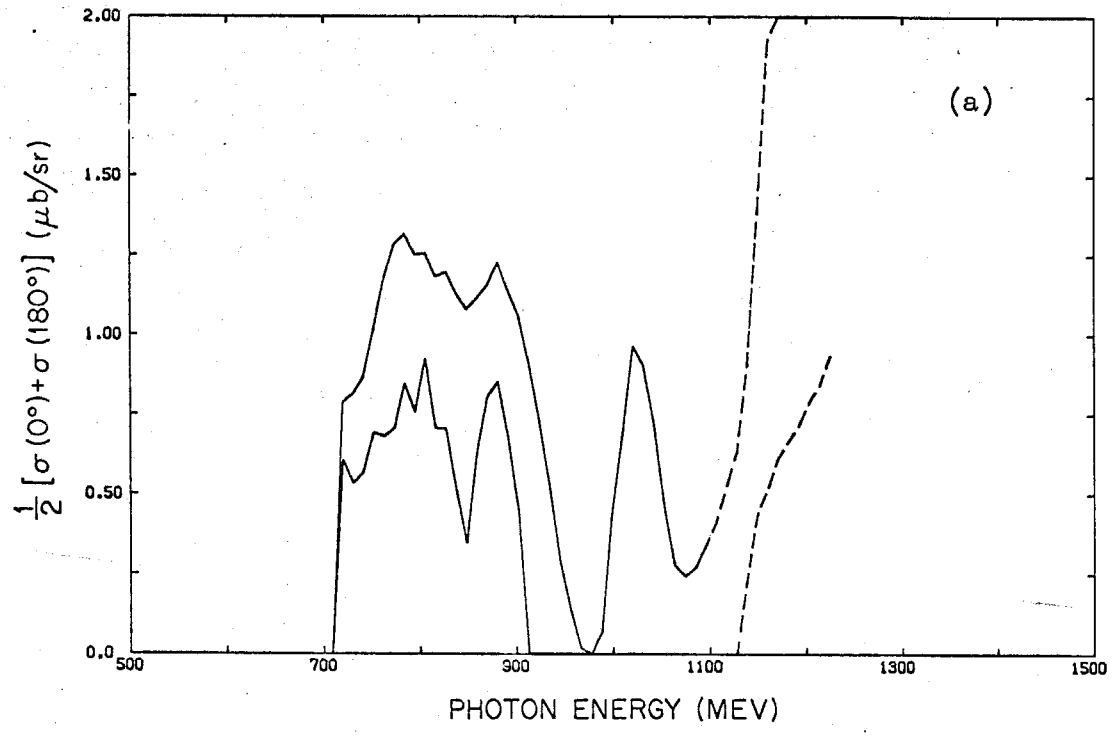


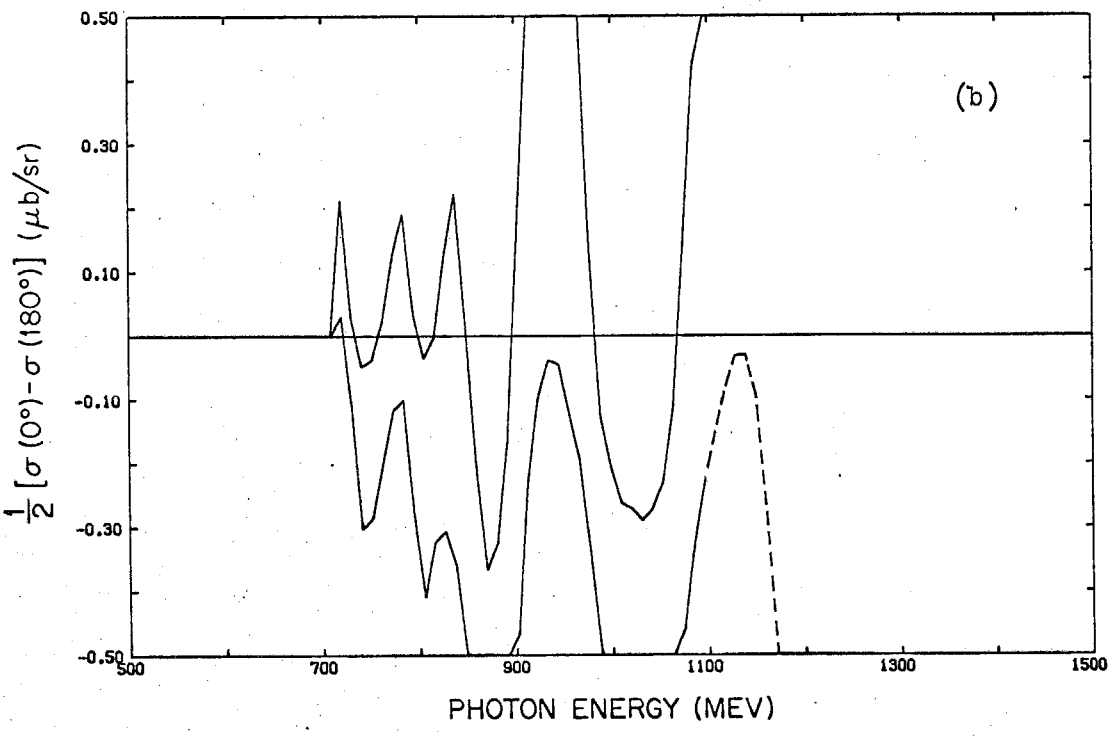


Figure 4.4 Error Envelope of (a) $\sigma_o(k)$ and (b) $\sigma_1(k)$, $\chi^2 = 4$.

displayed in Figure 4.1 for the term $\sigma_o(k)$ alone. Those solutions were obtained with a relatively weak $\chi^2$ requirement in order to be comparable with the $\chi^2 = 60$ solution for both $\sigma_o(k)$ and $\sigma_1(k)$. (The "forward" solution, Figure 4.1a, was obtained with $\chi^2 = 45$ for 12 input data. The "backward" solution, Figure 4.1b, had $\chi^2 = 45$ for 13 input data.) Although we do not display them here, the solutions for $\sigma_o(k)$ alone also assume negative values near 1000 MeV for more stringent $\chi^2$ requirements. It appears that the input data are not sufficiently dense near and above 1000 MeV to determine both $\sigma_o(k)$ and $\sigma_1(k)$ simultaneously, nor to determine $\sigma_o(k)$ alone for a stringent $\chi^2$ requirement. We thus take the solutions for $\sigma_o(k)$ alone, with a weak $\chi^2$ requirement, as best representing the method of parametrization.

Table 4.2 lists the separate "forward" and "backward" solutions for $\sigma_o(k)$ at 10-MeV intervals, along with the errors and certain other quantities which are explained below. From Figure 4.1, one notices immediately that the errors on $\sigma_o(k)$ are smaller than the errors on the discrete points produced by the method of linear combinations. The reason is that the solutions for $\sigma_o(k)$ have an intrinsic resistance to change, the degree of which is controlled by the setting of $\chi^2$. Recall that the threshold behavior of $\sigma_o(k)$ is externally constrained, so that the solution has an especially high resistance to change near threshold. One should refer to the discrete points for a less method-dependent idea of the cross section error. We are forced to turn to the discrete points for information on $\langle\cos\theta^*\rangle$ and the error, $\Delta\cos\theta^*$. The reported values for those

TABLE 4.2

CROSS SECTION FOR FORWARD AND BACKWARD PHOTOPRODUCTION, HYBRID RESULTS

| | Forward | | | | Backward | | | | Hybrid $\sigma_o$ and $\sigma_1$ | | | |
|---|---|---|---|---|---|---|---|---|---|---|---|---|
| k (MeV) | $\langle\cos\theta\rangle$ | $\Delta\cos\theta$ | $\frac{d\sigma}{d\Omega}$ (μb/sr) | $\Delta\frac{d\sigma}{d\Omega}$ (μb/sr) | $\langle\cos\theta\rangle$ | $\Delta\cos\theta$ | $\frac{d\sigma}{d\Omega}$ (μb/sr) | $\Delta\frac{d\sigma}{d\Omega}$ (μb/sr) | $\sigma_o^H$ (μb/sr) | $\Delta\sigma_o^H$ (μb/sr) | $\sigma_1^H$ (μb/sr) | $\Delta\sigma_1^H$ (μb/sr) |
| 710 | -0.38 | 0.70 | 0.073 | 0.001 | 0.59 | 0.65 | 0.075 | 0.004 | 0.073 | 0.002 | 0.002 | 0.004 |
| 720 | -0.04 | 0.54 | 0.605 | 0.009 | 0.20 | 0.51 | 0.621 | 0.023 | 0.608 | 0.008 | 0.069 | 0.105 |
| 730 | 0.30 | 0.39 | 0.786 | 0.011 | -0.20 | 0.38 | 0.802 | 0.015 | 0.796 | 0.010 | -0.031 | 0.036 |
| 740 | 0.63 | 0.24 | 0.890 | 0.011 | -0.60 | 0.24 | 0.902 | 0.014 | 0.896 | 0.009 | -0.010 | 0.014 |
| 750 | 0.75 | 0.19 | 0.955 | 0.010 | -0.74 | 0.19 | 0.964 | 0.028 | 0.960 | 0.015 | -0.007 | 0.020 |
| 760 | 0.77 | 0.19 | 0.994 | 0.010 | -0.75 | 0.18 | 1.005 | 0.042 | 0.999 | 0.022 | -0.007 | 0.028 |
| 770 | 0.79 | 0.19 | 1.010 | 0.009 | -0.77 | 0.17 | 1.028 | 0.050 | 1.019 | 0.026 | -0.012 | 0.033 |
| 780 | 0.81 | 0.18 | 1.009 | 0.009 | -0.78 | 0.17 | 1.041 | 0.049 | 1.025 | 0.025 | -0.020 | 0.031 |
| 790 | 0.83 | 0.16 | 0.995 | 0.009 | -0.79 | 0.17 | 1.049 | 0.041 | 1.023 | 0.022 | -0.033 | 0.025 |
| 800 | 0.86 | 0.14 | 0.970 | 0.010 | -0.80 | 0.17 | 1.052 | 0.031 | 1.012 | 0.017 | -0.049 | 0.020 |
| 810 | 0.88 | 0.12 | 0.936 | 0.011 | -0.81 | 0.17 | 1.050 | 0.034 | 0.995 | 0.019 | -0.068 | 0.021 |
| 820 | 0.89 | 0.11 | 0.895 | 0.013 | -0.84 | 0.14 | 1.045 | 0.055 | 0.972 | 0.029 | -0.087 | 0.033 |
| 830 | 0.90 | 0.10 | 0.848 | 0.015 | -0.87 | 0.10 | 1.034 | 0.084 | 0.943 | 0.043 | -0.105 | 0.048 |
| 840 | 0.91 | 0.09 | 0.797 | 0.018 | -0.90 | 0.07 | 1.017 | 0.111 | 0.908 | 0.056 | -0.122 | 0.062 |
| 850 | 0.91 | 0.09 | 0.744 | 0.020 | -0.91 | 0.06 | 0.992 | 0.132 | 0.868 | 0.067 | -0.137 | 0.073 |
| 860 | 0.92 | 0.08 | 0.688 | 0.023 | -0.91 | 0.06 | 0.960 | 0.145 | 0.825 | 0.074 | -0.149 | 0.081 |
| 870 | 0.93 | 0.08 | 0.632 | 0.026 | -0.91 | 0.06 | 0.920 | 0.150 | 0.777 | 0.077 | -0.157 | 0.083 |
| 880 | 0.93 | 0.07 | 0.576 | 0.028 | -0.91 | 0.06 | 0.874 | 0.147 | 0.727 | 0.076 | -0.162 | 0.081 |
| 890 | 0.93 | 0.08 | 0.520 | 0.031 | -0.91 | 0.06 | 0.821 | 0.135 | 0.672 | 0.070 | -0.163 | 0.075 |
| 900 | 0.92 | 0.09 | 0.466 | 0.034 | -0.91 | 0.06 | 0.763 | 0.116 | 0.615 | 0.061 | -0.162 | 0.066 |
| 910 | 0.91 | 0.09 | 0.415 | 0.036 | -0.91 | 0.06 | 0.701 | 0.092 | 0.558 | 0.049 | -0.157 | 0.054 |
| 920 | 0.90 | 0.10 | 0.366 | 0.039 | -0.92 | 0.05 | 0.638 | 0.067 | 0.501 | 0.039 | -0.150 | 0.043 |
| 930 | 0.89 | 0.11 | 0.320 | 0.040 | -0.92 | 0.05 | 0.575 | 0.046 | 0.446 | 0.031 | -0.141 | 0.034 |

TABLE 4.2 (continued)

CROSS SECTION FOR FORWARD AND BACKWARD PHOTOPRODUCTION, HYBRID RESULTS

| | Forward | | | | Backward | | | | Hybrid $\sigma_o$ and $\sigma_1$ | | | |
|---|---|---|---|---|---|---|---|---|---|---|---|---|
| k (MeV) | $\langle\cos\theta\rangle$ | $\Delta\cos\theta$ | $\frac{d\sigma}{d\Omega}$ (μb/sr) | $\Delta\frac{d\sigma}{d\Omega}$ (μb/sr) | $\langle\cos\theta\rangle$ | $\Delta\cos\theta$ | $\frac{d\sigma}{d\Omega}$ (μb/sr) | $\Delta\frac{d\sigma}{d\Omega}$ (μb/sr) | $\sigma_o^H$ (μb/sr) | $\Delta\sigma_o^H$ (μb/sr) | $\sigma_1^H$ (μb/sr) | $\Delta\sigma_1^H$ (μb/sr) |
| 940 | 0.89 | 0.11 | 0.277 | 0.042 | -0.92 | 0.05 | 0.513 | 0.043 | 0.393 | 0.030 | -0.130 | 0.033 |
| 950 | 0.88 | 0.12 | 0.239 | 0.043 | -0.92 | 0.05 | 0.453 | 0.059 | 0.343 | 0.036 | -0.119 | 0.041 |
| 960 | 0.87 | 0.13 | 0.204 | 0.044 | -0.92 | 0.05 | 0.397 | 0.080 | 0.298 | 0.045 | -0.108 | 0.051 |
| 970 | 0.86 | 0.14 | 0.173 | 0.044 | -0.92 | 0.05 | 0.346 | 0.100 | 0.257 | 0.053 | -0.097 | 0.061 |
| 980 | 0.85 | 0.14 | 0.147 | 0.044 | -0.92 | 0.05 | 0.300 | 0.116 | 0.220 | 0.060 | -0.086 | 0.070 |
| 990 | 0.84 | 0.15 | 0.124 | 0.042 | -0.92 | 0.05 | 0.260 | 0.128 | 0.189 | 0.065 | -0.077 | 0.076 |
| 1000 | 0.83 | 0.16 | 0.106 | 0.041 | -0.93 | 0.05 | 0.227 | 0.134 | 0.163 | 0.067 | -0.069 | 0.079 |
| 1010 | 0.82 | 0.17 | 0.091 | 0.038 | -0.03 | 0.05 | 0.200 | 0.134 | 0.142 | 0.066 | -0.062 | 0.079 |
| 1020 | 0.81 | 0.17 | 0.080 | 0.035 | -0.93 | 0.05 | 0.179 | 0.128 | 0.126 | 0.063 | -0.057 | 0.076 |
| 1030 | 0.81 | 0.18 | 0.072 | 0.032 | -0.93 | 0.05 | 0.164 | 0.118 | 0.115 | 0.057 | -0.053 | 0.070 |
| 1040 | 0.80 | 0.19 | 0.068 | 0.028 | -0.93 | 0.04 | 0.156 | 0.104 | 0.108 | 0.050 | -0.051 | 0.062 |
| 1050 | 0.79 | 0.19 | 0.066 | 0.024 | -0.93 | 0.04 | 0.153 | 0.088 | 0.106 | 0.042 | -0.051 | 0.053 |
| 1060 | 0.78 | 0.20 | 0.066 | 0.020 | -0.93 | 0.04 | 0.155 | 0.074 | 0.107 | 0.036 | -0.052 | 0.045 |
| 1070 | 0.77 | 0.21 | 0.068 | 0.016 | -0.93 | 0.04 | 0.161 | 0.069 | 0.110 | 0.033 | -0.055 | 0.042 |
| 1080 | 0.76 | 0.22 | 0.073 | 0.015 | -0.94 | 0.04 | 0.172 | 0.080 | 0.117 | 0.037 | -0.058 | 0.048 |
| 1090 | 0.75 | 0.22 | 0.078 | 0.016 | -0.94 | 0.04 | 0.185 | 0.104 | 0.126 | 0.047 | -0.063 | 0.062 |
| 1100 | 0.74 | 0.23 | 0.085 | 0.020 | -0.94 | 0.04 | 0.202 | 0.138 | 0.137 | 0.062 | -0.070 | 0.083 |
| 1110 | 0.74 | 0.24 | 0.092 | 0.026 | -0.94 | 0.04 | 0.221 | 0.179 | 0.149 | 0.080 | -0.077 | 0.108 |
| 1120 | 0.73 | 0.25 | 0.101 | 0.032 | -0.94 | 0.04 | 0.242 | 0.222 | 0.162 | 0.099 | -0.085 | 0.135 |
| 1130 | 0.72 | 0.25 | 0.109 | 0.039 | -0.94 | 0.04 | 0.265 | 0.269 | 0.177 | 0.118 | -0.093 | 0.164 |
| 1140 | 0.71 | 0.26 | 0.118 | 0.047 | -0.94 | 0.04 | 0.288 | 0.317 | 0.191 | 0.139 | -0.103 | 0.194 |
| 1150 | 0.70 | 0.27 | 0.128 | 0.054 | -0.94 | 0.04 | 0.313 | 0.367 | 0.207 | 0.160 | -0.112 | 0.226 |
| 1160 | 0.69 | 0.27 | 0.137 | 0.062 | -0.95 | 0.03 | 0.337 | 0.418 | 0.222 | 0.180 | -0.122 | 0.258 |

quantities in Table 4.2 were obtained from the discrete points (cf. Table 4.1) by linear interpolation in k.

For each value of k, we have the value of $\sigma_o(k)$ for two values of $\langle \cos \theta^* \rangle$, which amounts to two points of the full angular distribution. Those two points determine a straight line, parametrized here as $\sigma_o^H(k) + \sigma_1^H(k) \cos \theta^*$. This is a non-simultaneous version of the solution for $\sigma_o$ and $\sigma_1$ in the parametrization $\sigma_o(k) + \sigma_1(k)\cos\theta^*$, and it is presented in Table 4.2 under the heading "Hybrid $\sigma_o$ and $\sigma_1$." Figure 4.5 displays $\sigma_o^H$ and $\sigma_1^H$ after making the following small cosmetic alteration. Near threshold, the interpolated values for $\langle \cos \theta^* \rangle$ are not meaningful, since the resolution there becomes a flat function of $\cos \theta^*$. We have somewhat arbitrarily imposed the conditions

$$\begin{aligned} &\text{Forward} \quad \langle \cos \theta^* \rangle \geq +0.5 \\ &\text{Backward} \quad \langle \cos \theta^* \rangle \leq -0.5 \quad , \end{aligned}$$

which affect $\sigma_o^H$ and $\sigma_1^H$ only between threshold and about 735 MeV.

The cross section errors presented here are statistical only and do not reflect any of the systematic uncertainties discussed in Section 6.10. The overall systematic uncertainty was estimated as 8 percent, most of which applies equally to forward and backward measurements of the cross section. Up to 2 percent of this uncertainty, it was estimated, affects forward and backward measurements in opposite directions. This implies that, in the parametrization $\sigma_o(k) + \sigma_1(k)\cos \theta^*$, the systematic uncertainty on $\sigma_o$ is approximately 6 percent. The sys-

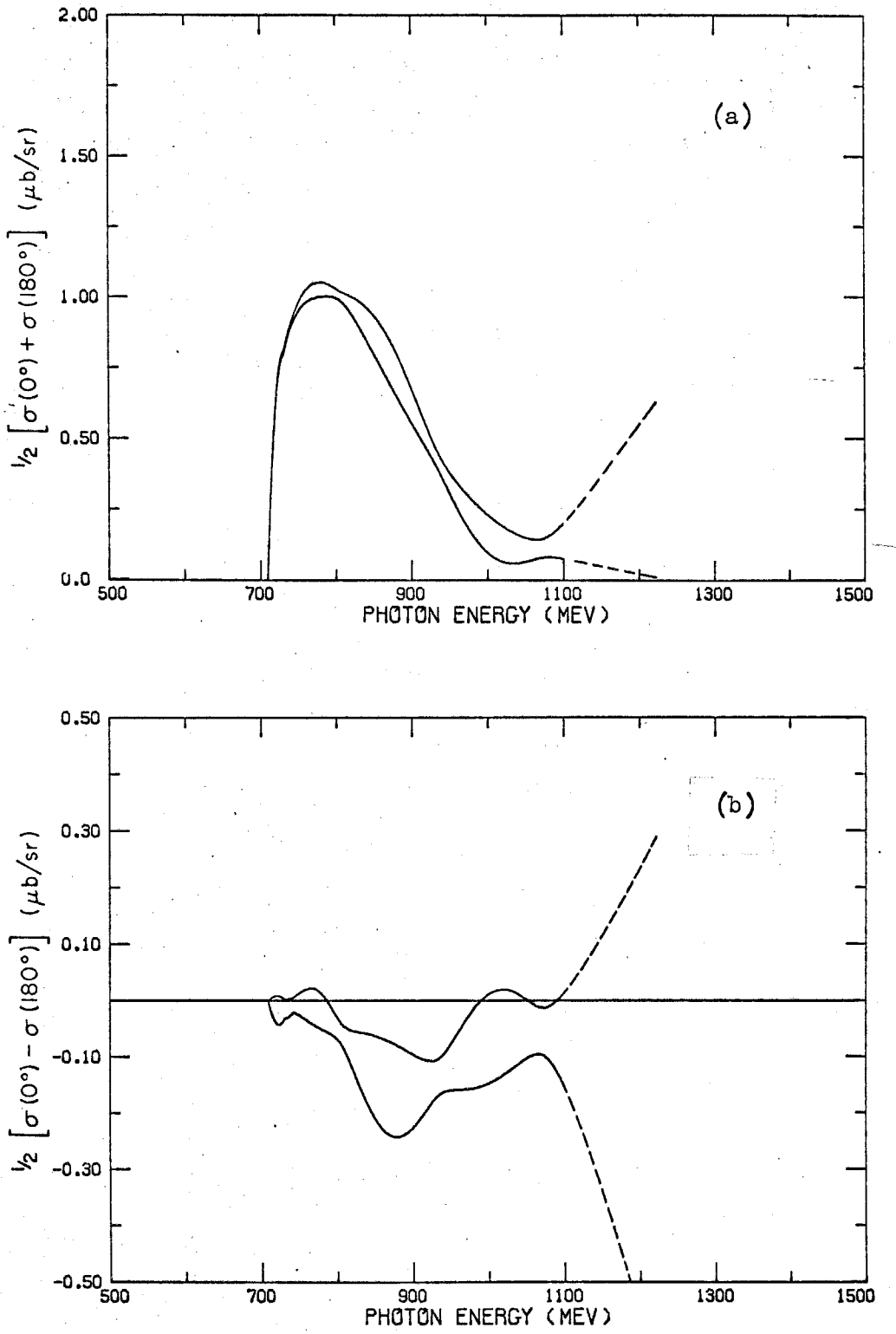


Figure 4.5 Hybrid Results for (a) $\sigma_o(k)$ and (b) $\sigma_1(k)$

tematic uncertainty on $\sigma_1$ is approximately 6 percent plus 2 percent of the value for $\sigma_o$. To apply this information, we say that the cross section values in Table 4.1 bear a systematic uncertainty of the same magnitude as a statistical standard deviation. As for $\sigma_o$ and $\sigma_1$, as represented by the "hybrid" results, we say that $\sigma_o^H$ is also about as uncertain as a statistical standard deviation, while the uncertainty in $\sigma_1^H$ is at most 0.02 μb/sr, which, by comparison with statistical errors, is negligible above, say, 825 MeV.

A final note about the method of linear combinations is in order. The originator of that evaluation program, S. J. Yellin, gives less weight to that method than we have given it here, on the basis of the greater effort that went into the development of the method of parametrization.[5] The hybrid form of the results is our attempt to combine the most reliable features of both methods. The basic cross section values for the hybrid results are taken from the separate forward and backward solutions for $\sigma_o(k)$ alone, which agree rather well with the discrete points from the method of linear combinations, with possibly one exception. The forward point near 970 MeV, with a value of $(-0.04 \pm 0.07)$, is about three standard deviations from the value of $(0.17 \pm 0.04)$ for the forward $\sigma_o$ at 970 MeV. On the grounds that it is more reliable, we take the value for $\sigma_o$ as the more nearly correct estimate.

# 5. DISCUSSION

Our measurements of the cross section at forward and backward angles show a significant departure from angular isotropy, starting at about 0.8 GeV and persisting to the highest energies covered by this experiment (about 1.1 GeV). Isotropy prevails between threshold and about 0.8 GeV. The departure from isotropy consistently favors the backward cross section over the forward cross section. To quote a typical figure, the backward cross section dominates the forward by about (30 ± 15) percent at 0.9 GeV. We interpret our results in a simple phenomenological model below. First, however, we wish to briefly compare our data with those from previous experiments.

## 5.1 Comparison with Previous Measurements

As mentioned in the Introduction, no firm evidence for a departure from isotropy has been reported prior to this experiment. To give substance to this statement, we have taken the liberty of fitting certain world data with a cross section of the form $\sigma_o(k) + \sigma_1(k) \cos \theta^*$, where k is the photon energy in the laboratory frame and $\theta^*$ is the center-of-mass production angle. (Note that $\sigma_o$ and $\sigma_1$ are half the sum and difference, respectively, of the forward and backward cross sections.) The results of this experiment are conveniently expressed as smooth functions of k for the terms $\sigma_o$ and $\sigma_1$, as determined in the "hybrid" formulation (Section 4). The results of previous experiments are more logically presented by fitting the distribution of cos $\theta^*$, thereby determining $\sigma_o$ and $\sigma_1$ for only those values of k where angular

distributions exist. The bottom frame of Figure 5.1 shows the comparison, where the pair of smooth curves represents the one-standard-deviation limits for the measurement of $\sigma_1(k)$ in this experiment. The data points shown there were obtained by fitting the angular distributions taken at Frascati,[2,28] Orsay,[3] and Stanford.[6] It is clear that the errors on the data taken prior to this experiment are too large to say that there is agreement with our data, but we note that the highest-energy Frascati point, at 0.85 GeV, is 1.5 standard deviations from isotropy and in the same direction as our result. In using the Orsay data, we omitted the forward-most measurements at 0.835 and 0.865 GeV, since the reported cross section there is too low and too high, respectively, for credibility. Finally, we compare our result for $\sigma_o(k)$ directly with various world data at intermediate angles. (In our parametrization, the cross section at $90^o$ is just $\sigma_o$.) This is shown in the top frame of Figure 5.1 The agreement here is sufficiently definite to give us a measure of confidence in our result for $\sigma_1$.

## 5.2 Phenomenological Analysis

We wish to describe the data from this experiment, along with certain other data on eta photoproduction, using a simple "isobar model." We circumvent the difficulties involved in the cross section evaluation (Section 4) by fitting directly to the measurements of the eta yield. Regrettably, we cannot present here the enormous amount of efficiency data needed to reproduce our fits to the eta yield. We have checked, however, that fitting the cross section data of

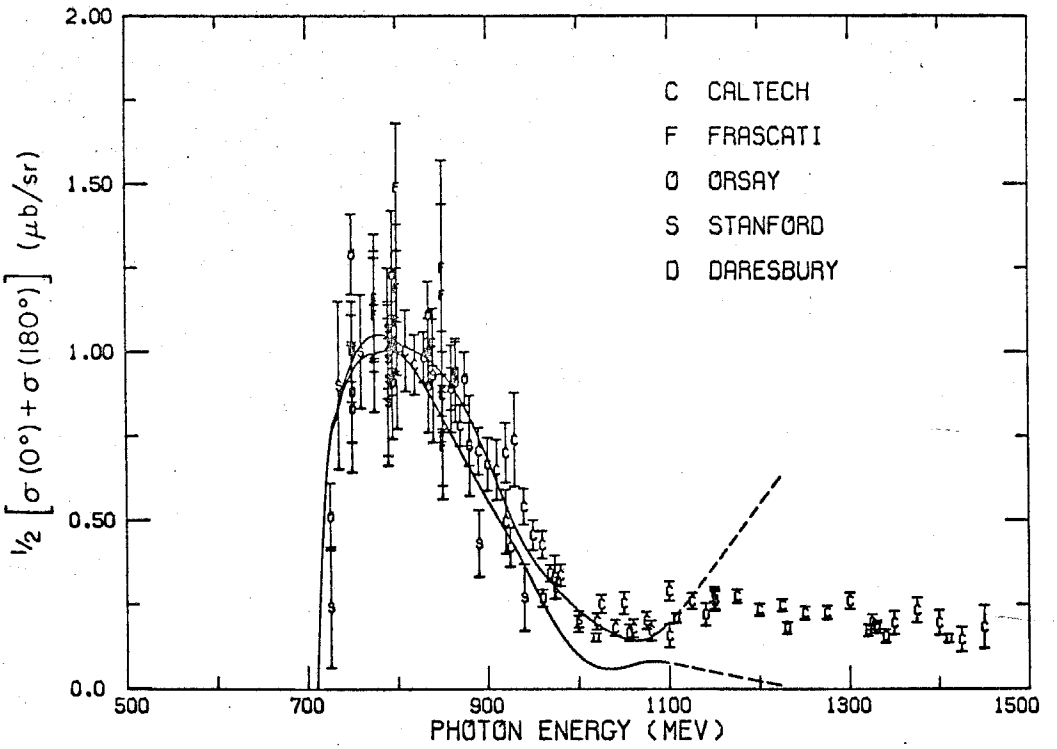


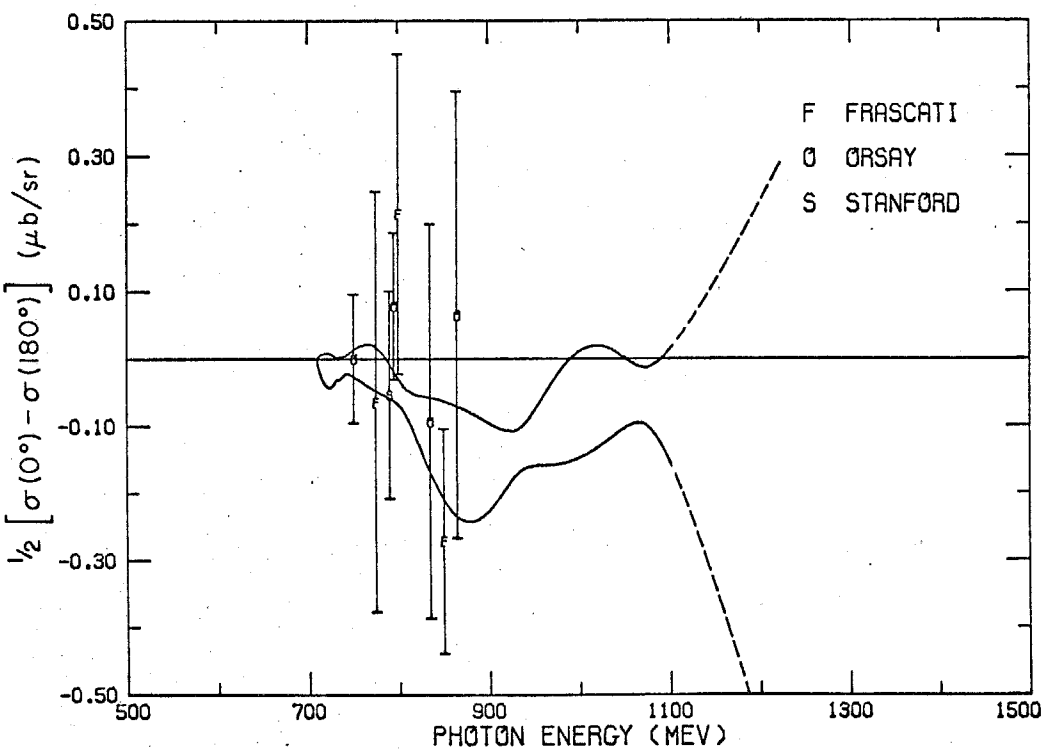


Figure 5.1 Comparison with Previous Measurements :
(a) $\sigma_o(k)$ and (b) $\sigma_1(k)$

Section 4 gives results which closely agree with those reported here. The additional data which we consider are measurements of the recoil proton polarization[1] and cross section measurements at intermediate angles and somewhat higher energies than were covered by the experiment.[26,27] For the most part, we limit our attention to photon energies between threshold and 1.1 GeV, or between about 1.5 and 1.7 GeV in the center-of-mass energy. We will see that the best description for data below 1.1 GeV does not extrapolate well to higher energy. We briefly describe a fit which does extend to higher energy tolerably well.

A. Scope of the Analysis

We have mentioned the sources of our input data, and now we outline the framework of the isobar model. We restrict our consideration to the $I = 1/2$, $J = 1/2$ states $P_{11}(1460)$, $S_{11}(1550)$, $S_{11}(1710)$, and $P_{11}(1780)$. We neglect higher partial-wave resonances for the reasons given in the Introduction. We avail ourselves of the Born approximation for the proton pole in the s and u channels ($\eta$ exchange is excluded), including both electric and magnetic couplings explicitly. We include no process which contributes in the t channel, since pion exchange is forbidden and higher-mass meson exchange (e.g. $\rho$, $\omega$, B) should be important only at higher energies than we consider here. Finally, we include highly empirical terms for the non-resonant background in both the $s_{11}$ and $p_{11}$ partial waves.

Our strategy is to seek as simple a description as possible, starting from the states $S_{11}(1550)$ and $P_{11}(1780)$ alone, represented

by Breit-Wigner terms with relatively real coefficients. We then seek to improve the description by making use of the other ingredients of our model, namely, the states $P_{11}(1460)$ and $S_{11}(1710)$, the Born approximation, the background terms, and complex coefficients for the Breit-Wigner terms.

We are dealing with an inelastic, coupled-channel type of reaction, in which the important channel $\pi N$ is accessible at all energies above threshold. Our description, however, extends only to eta photoproduction, or to just one off-diagonal element of the full T-matrix. Let us outline what would be involved in a more complete treatment, one which satisfies unitarity (and time-reversal symmmetry). The appropriate framework for such a treatment is the K-matrix formalism of nuclear physics, as adapted for elementary particle physics along the lines described by Dalitz.[29] Chau, Dombey, and Moorhouse[7] discuss a K-matrix formalism containing the channels $\pi N$, $\eta N$, and $\gamma N$, where the channel $\gamma N$ is in the nature of a perturbation on the K-matrix for the channels $\pi N$ and $\eta N$ alone, and where the three channels are considered sufficient to saturate unitarity in the medium-energy range of the analysis. Davies and Moorhouse, in a treatment confined to the physical channels $\pi N$ and $\eta N$, simulate inelastic multiparticle processes with a two-body pseudo-channel $\sigma N$, where the pseudo-meson $\sigma$ is somewhat arbitrarily chosen to have a mass of 390 MeV.[30]

K-matrix phenomenology necessarily involves the introduction of many free parameters to describe a limited amount of data for the various elastic and inelastic reactions involved. Even with the

constraints provided by unitarity and time-reversal symmetry, and ignoring the matrix element for $\gamma N \rightarrow \gamma N$ on the basis of interaction strength, only tentative and non-unique descriptions may be reached in present K-matrix analyses. Our approach, treating only eta photoproduction, probably affords as good a description of our data as one can reasonably expect at this time.

B. Formalism

We use a helicity formalism for the eta photoproduction amplitude. In terms of the conventional parity-conserving helicity amplitudes $H_i$, $(i = 1, \ldots, 4)$, the angular distributions for the cross section, $d\sigma/d\Omega\,(\theta^*)$, and the recoil proton polarization in the direction of $\vec{k} \times \vec{q}$, $P(\theta^*)$, are given by[13]

$$\frac{d\sigma}{d\Omega}(\theta^*) = \frac{1}{2}\,\frac{q^*}{k^*} \sum_{i=1}^{4} |H_i|^2$$

and

$$P(\theta^*)\frac{d\sigma}{d\Omega}(\theta^*) = -\frac{q^*}{k^*}\,\mathrm{Im}\,(H_1 H_3^* + H_2 H_4^*) \quad .$$

We are primarily interested in the $s_{11}$ and $p_{11}$ partial waves, which correspond to electric and magnetic dipole transitions, respectively. If higher partial waves can be ignored, then the cross section and recoil proton polarization are given by

$$\frac{d\sigma}{d\Omega}(\theta^*) = \frac{q^*}{k^*}\left(|s_{11}|^2 + |p_{11}|^2 - 2\,\mathrm{Re}\,(s_{11}\,p_{11}^*)\cos\theta^*\right)$$

and

$$P(\theta^*)\frac{d\sigma}{d\Omega}(\theta^*) = \frac{q^*}{k^*}\left(\quad 0 \quad + 2\,\mathrm{Im}(s_{11}\,p_{11}^*)\sin\theta^*\right). \tag{5.1}$$

The proton pole, of course, brings in higher partial waves. As we will see, however, the Born approximation is of limited usefulness to our analysis and is explicitly omitted from many of our fits.

Resonances are represented by Breit-Wigner terms of the variety used by Walker.[13] The amplitude, A, as a function of center-of-mass energy, W, is given by

$$A(W) = A(W_o)\left(\frac{k_o\,q_o}{k\,q}\right)^{\frac{1}{2}} \frac{W_o\,\Gamma^{\frac{1}{2}}\,\Gamma_\gamma^{\frac{1}{2}}}{W_o^2 - W^2 - i\,W_o\,\Gamma} \tag{5.2}$$

where

$$\Gamma = \Gamma_o\, f(q, q_o, \ell, X),$$

$$\Gamma_\gamma = \Gamma_o\, f_\gamma\,(k, k_o, j_\gamma, X),$$

where $f$ and $f_\gamma$ are given by

$$f\,(q, q_o, \ell, X) = \left(\frac{q}{q_o}\right)^{2\ell+1}\left(\frac{1_o^2 + X^2}{q^2 + X^2}\right)^{\ell}$$

and

$$f_\gamma\,(k,\,k_o,\,j_\gamma,\,X) \;=\; \left(\frac{k}{k_o}\right)^{2j_\gamma} \left(\frac{k_o^2 + X^2}{k^2 + X^2}\right)^{j_\gamma} \quad .$$

All energy and momenta above are center-of-mass quantities, and the zero-subscripted quantities denote the values at resonance peak. $A(W_o)$ is an adjustable complex parameter. We give X the value 250 MeV. For $s_{11}$ resonances, $\ell = 0$, while for $p_{11}$ resonances, $\ell = 1$, and in either case, the total photon angular momentum is $j_\gamma = 1$. $\Gamma_o$ is the total width. The energy dependence of $\Gamma$ in the denominator of (5.2) is inappropriate for an inelastic reaction near threshold. As a simple ansatz, we replace $\Gamma$ in the denominator by

$$\Gamma \;=\; \Gamma_\eta\, f(q,\, q_o,\, \ell,\, X) \;+\; \Gamma_\pi\, f(q^\pi,\, q_o^\pi,\, \ell,\, X) \quad ,$$

with $\Gamma_o = \Gamma_\eta + \Gamma_\pi$ ,

where $q^\pi$ is the momentum in the $\pi N$ channel. It remains to choose values for $\Gamma_\eta$ and $\Gamma_\pi$ for each resonance which appears in our model, making the approximation that the channels $\pi N$ and $\eta N$ saturate unitarity. Since our modification has little impact for resonances with peaks far from threshold, we set $\Gamma_\pi = 0$ for both $S_{11}(1710)$ and $P_{11}(1780)$. We set $\Gamma_\pi = 0.5\,\Gamma_\eta$ for $S_{11}(1550)$,[20] and we empirically set $\Gamma_\pi = 5.0\,\Gamma_\eta$ for $P_{11}(1460)$. In the case of a resonance peak below threshold, such as for $P_{11}(1460)$, we have to take $q_o \to i|q_o|$, and we rewrite

$$f(q,\, q_o,\, \ell,\, X) \;=\; \left(\frac{q}{|q_o|}\right)^{2\ell+1} \left(\frac{-q_o^2 + X^2}{q^2 + X^2}\right)^{\ell} \quad .$$

The highly empirical term for the non-resonant background in the $\ell$th partial wave is given by

$$(\text{Background})_\ell = B_\ell \left\{ \frac{k_o q_o}{kq} \; f(q, q_o, \ell, X) \; f_\gamma(k, k_o, j_\gamma, X) \right\}^{\frac{1}{2}} ,$$

where $B_\ell$ is an adjustable complex parameter. The resonance values for $q_o$ and $k_o$ are arbitrarily taken from $S_{11}(1550)$ or $P_{11}(1780)$, depending on whether $\ell$ is 0 or 1, respectively.

In our expressions for the Born approximation, the eta-nucleon coupling constant, $G_\eta$, is an adjustable parameter. From the $SU_{6W}$ quark model, $G_\eta$ is related to the pion-nucleon coupling constant, $G_\pi$, according to[31]

$$\frac{G_\eta}{G_\pi} = \frac{\sqrt{3}}{5} \approx 0.35 \quad .$$

Numerically, $G_\pi$ has the value $(14.4 \pm 0.4)$.[24] We will see that the best fits are obtained with considerably smaller values for $G_\eta/G_\pi$ than that predicted by the quark model.

C. Numerical Results

The framework for our results has been outlined above. The free parameters are the complex coefficients $A(W_o)$ for each resonance, the quantity $G_\eta$ for the Born approximation, and the complex background coefficients $B_o$ and $B_1$. The "masses" and total widths of the resonances were taken as

| Resonance | $W_o$ (GeV) | $\Gamma_o$ (GeV) |
|---|---|---|
| $S_{11}(1550)$ | 1.550 | 0.130 |
| $P_{11}(1780)$ | 1.780 | 0.250 |
| $P_{11}(1460)$ | 1.460 | 0.240 |
| $S_{11}(1710)$ | 1.710 | 0.250 |

Table 5.1 presents the results of minimizing $\chi^2$ for various combinations of the resonances and other terms. For convenience, we refer to the solutions according to the number assigned them in the left-most column. A quantity is underlined when the corresponding parameter was not allowed to vary, or the quantity is omitted altogether if the fixed value of the inactive parameter was trivially zero. We report the value for $A(W_o)$ in units of $(\mu b/sr)^{\frac{1}{2}}$, where the quantity in parentheses is the phase angle of $A(W_o)$, relative to that for $S_{11}(1550)$. The units of $B_o$ and $B_1$ are also $(\mu b/sr)^{\frac{1}{2}}$.

Before discussing the individual solutions, a few comments on $\chi^2$ are in order. The right-most column lists $\chi^2$ per degree of freedom, denoted $\chi^2_{df}$. If only random statistical errors are involved, and if those errors are accurately estimated, then $\chi^2_{df} \approx 1$ for a good fit. However, it appears that all parties contributing data to our fits are guilty of inaccurately estimating their errors, and systematic effects are typically not included. Thus, we attach no absolute significance to the value of $\chi^2_{df}$ here, but rather we use that quantity in comparing solutions.

TABLE 5.1

VALUES OF THE PARAMETERS IN THE PHENOMENOLOGICAL ANALYSIS

| Solution | $S_{11}(1550)$ | $P_{11}(1780)$ | $P_{11}(1460)$ | $S_{11}(1710)$ | $G_\eta/G_\pi$ | $B_o$ | $B_1$ | $\chi^2$ | $\chi^2_{df}$ |
|---|---|---|---|---|---|---|---|---|---|
| 1 | 2.08 | 0.18($\underline{0}^o$) | | | | | | 326.6 | 4.87 |
| 2 | 2.10 | 0.34($\underline{31}^o$) | | | | | | 260.6 | 3.95 |
| 3 | 2.09 | | | | -0.007 | | | 347.7 | 5.19 |
| 4 | 2.09 | 0.41($\underline{31}^o$) | | | 0.020 | | | 251.4 | 3.81 |
| 5 | 2.11 | 0.30($\underline{31}^o$) | 0.08($\underline{0}^o$) | | | | | 256.4 | 3.88 |
| 6 | 2.10 | 0.35($\underline{31}^o$) | 0.02($\underline{60}^o$) | | | | | 260.4 | 3.95 |
| 7 | 2.11 | 0.24($\underline{31}^o$) | -0.12($\underline{120}^o$) | | | | | 254.8 | 3.86 |
| 8 | 2.08 | 0.33($\underline{31}^o$) | | 0.03($\underline{0}^o$) | | | | 260.2 | 3.94 |
| 9 | 2.10 | 0.35($\underline{31}^o$) | | -0.01($\underline{60}^o$) | | | | 260.4 | 3.95 |
| 10 | 2.09 | 0.33($\underline{31}^o$) | | 0.01($\underline{120}^o$) | | | | 260.6 | 3.95 |
| 11 | 2.23 | 0.40($\underline{31}^o$) | | | | (0.008 -0.071i) | | 241.3 | 3.71 |
| 12 | 2.11 | | | | | | (0.085 +0.199i) | 234.1 | 3.55 |
| 13 | 2.44 | 0.60($\underline{31}^o$) | | -0.44($\underline{45}^o$) | | | | 256.0 | 3.82 |

We now consider the solutions represented in Table 5.1. We assume that $S_{11}(1550)$ dominates the amplitude just above threshold, and we further assume that the broad peak in the cross section at higher energies is most likely the effect of $P_{11}(1780)$. For a first solution, then, we try a model containing only those two states, using relatively real coefficients for the Breit-Wigner terms. The value of $\chi^2_{df}$ for this solution (solution 1 of Table 5.1) establishes a reference point for the other solutions. We now consider various ways of improving the fit. The most obvious first step is to allow a freely varying relative phase for the two Breit-Wigner coefficients, and the result (solution 2) is a distinct drop in the value of $\chi^2_{df}$. The best value for the phase angle, as returned by the $\chi^2$-minimization computer program, is (31 ± 3) degrees. For the rest of the solutions involving the $P_{11}(1780)$, we fix its phase angle (relative to $S_{11}(1550)$) to that value. As we will see, this simple two-state model, with a specific relative phase, provides about as good a fit to the data as we were able to attain here.

The Born term proved to be relatively useless for improving the fit. Solution 3 was the combination of $S_{11}(1550)$ and the Born term, with $P_{11}(1780)$ temporarily suppressed. The best value for $G_\eta/G_\pi$ was found to be -0.007, compared with the $SU_{6W}$ prediction of 0.35. The value for $\chi^2_{df}$ is higher than before, showing that the Born term is a poor replacement for $P_{11}(1780)$. When we tried the Born term in addition to both the $S_{11}(1550)$ and $P_{11}(1780)$, the best value for $G_\eta/G_\pi$ was 0.02, and the fit showed a rather small improvement (solution 4).

We then tried bringing in the states $P_{11}(1460)$ and $S_{11}(1710)$, again with no clear evidence for an improvement on the basic model of $S_{11}(1550)$ and $P_{11}(1780)$ with a relative phase angle of 31 degrees. The results are solutions 5, 6, and 7 for the admixture of $P_{11}(1460)$, solutions 8, 9, and 10 for $S_{11}(1710)$. In each case, we tried values of $0^{\circ}$, $60^{\circ}$ and $120^{\circ}$ for the phase angle of the state being introduced. In the case of $P_{11}(1780)$, the largest admixture was obtained with a phase angle of $120^{\circ}$, for which $A(W_o)$ had a best value of -0.12. The largest admixture of $S_{11}(1710)$ was 0.03, obtained with a phase angle of $0^{\circ}$.

Solutions 11 and 12 are the results of allowing the background terms to vary. The amount of each background in the fit is described by the complex parameters $B_o$ and $B_1$. When we added the S-wave background alone, solution 11, the best value for $B_o$ was negligible in absolute value (compared with the resonance parameters $A(W_o)$), and the quality of the fit was unaffected. When we added the P-wave background alone, or both S- and P-wave backgrounds, the $\chi^2$-minimization program could find no solution. A solution was found only when $P_{11}(1780)$ was taken out of the fit. Thus, solution 12 is the result for $S_{11}(1550)$ and the P-wave background. The best value for $B_1$ is comparable in absolute value with the typical value of $A(W_o)$ for $P_{11}(1780)$, and the fit shows a small improvement.

So far, we have restricted our attention to developing a fit in the photon energy range from threshold to 1.1 GeV, without regard to how the fit extrapolates to higher energy, where there is a broad peak

in the cross section (cf. Figure 5.1a). We have assumed that that peak is a consequence of the resonance $P_{11}(1780)$, but we have not used the cross section data in the vicinity of the peak to determine the amount of the $P_{11}(1780)$ term which appears in our fit. That burden has fallen instead on the data of this experiment and those of the recoil proton polarization measurements, via Eqs. (5.1). The amount of $P_{11}(1780)$ in our fit is actually insufficient, by about a factor of 5 in the cross section, to satisfactorily describe the cross section above 1.1 GeV. When we include higher-energy data in our fit, the amount of $P_{11}(1780)$ increases to a plausible level, but the fit still does not describe the broad peak satisfactorily, and the problem may be traced to the sign of the $S_{11}$-$P_{11}$ interference term in the cross section. Solution 13 in Table 5.2 represents one attempt to formulate a fit which extrapolates well to higher energy, using the three states $S_{11}(1550)$, $P_{11}(1780)$ and $S_{11}(1710)$. The relative phase between the two $S_{11}$ states has been adjusted to give destructive interference in the $S_{11}$ wave over as broad an energy range as possible, leaving the $P_{11}(1780)$ to describe the broad peak in the cross section, and the troublesome interference between $s_{11}$ and $p_{11}$ waves is minimized. Although we have used the $S_{11}(1710)$, other mechanisms could account for the presence of less $s_{11}$-wave in the tail of the Breit-Wigner peak describing the $S_{11}(1550)$, including a different type of Breit-Wigner term.

Figure 5.2 shows, in three frames, the quantities $\sigma_o(k)$, $\sigma_1(k)$, and $P(90^o)$ formerly defined (Section 5.1), for solutions 2 and 13. The

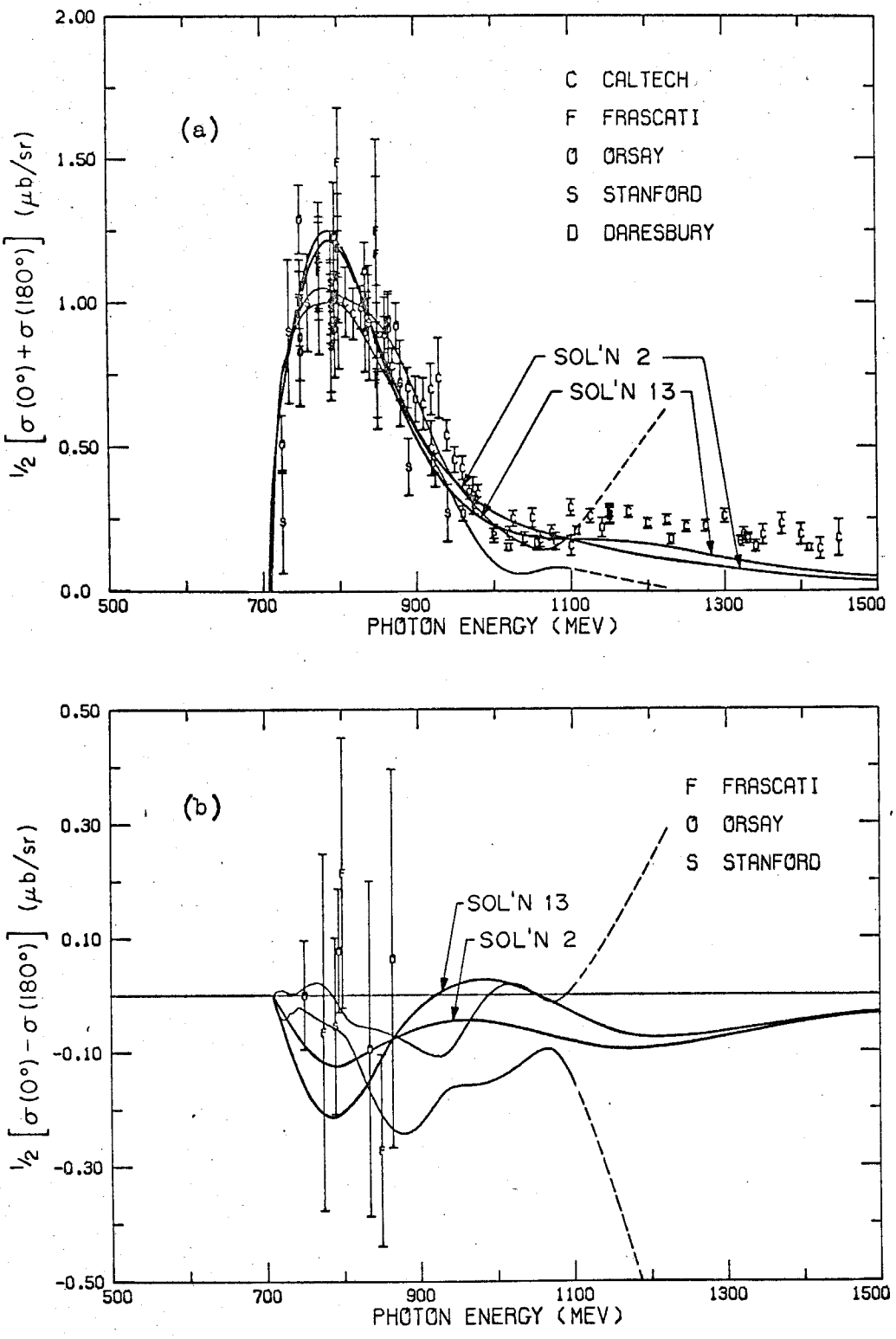


Figure 5.2 Resonance Model Solutions for (a) $\sigma_o(k)$, (b) $\sigma_1(k)$, and (c) $P(90^o)$

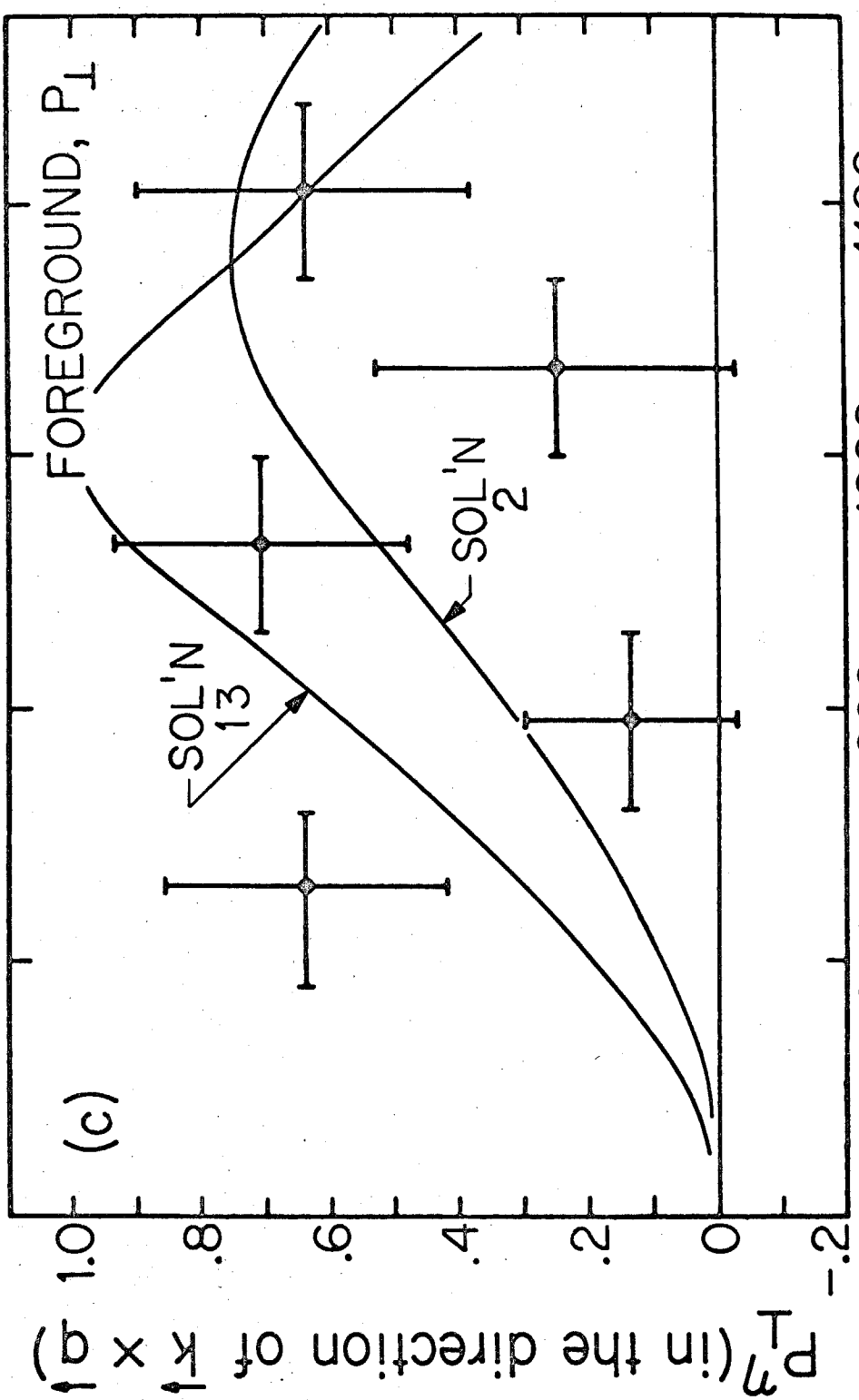


Figure 5.2 (Continued) Resonance Model Solutions for (a) $\sigma_o(k)$, (b) $\sigma_1(k)$, and (c) $P(90^o)$

former solution is representative of the best fit obtainable with a two-state model, and the latter represents a step in the direction of fitting cross section data at energies above 1.1 GeV in a three-state model.

## 5.3 Conclusions

The simple resonance model containing the states $S_{11}(1550)$ and $P_{11}(1780)$ may furnish an adequate description of eta photoproduction in the photon energy region from threshold to 1.1 GeV, but our results show that a relative phase angle of about 30 degrees between those resonances is required for an optimum description. In the context of that model, with the restriction to photon energy below 1.1 GeV, we find little in the way of evidence for either $P_{11}(1460)$ or $S_{11}(1710)$. The extrapolation to higher energy, however, requires the addition of some mechanism, such as another $S_{11}$ resonance, to modify the interference effects in the cross section due to the presence of both $s_{11}$ and $p_{11}$ partial waves. To recall a point mentioned in the Introduction, the $S_{11}(1710)$ is forbidden in the non-relativistic quark model, unless there is mixing between that state and the $S_{11}(1550)$.

There is an obvious need for additional measurements, particularly for complete angular distributions of the cross section at photon energies above 1 GeV. Recoil proton polarization data are also needed to completely determine the photoproduction amplitude in the $s_{11}$ and $p_{11}$ partial waves. Information from polarized target and polarized photon beam experiments should prove rewarding, especially if the amplitude is richer in higher partial waves than anticipated.

# 6. APPENDIX

## 6.1 Primary Photon Beam; Beam Monitoring

Electrons accelerated within the synchrotron collide with an internal target made of 1/32 inch tantalum (Z = 73), and the bremsstrahlung photon beam leaves the synchrotron through a 105.5 inch straight section of vacuum pipe capped with a mylar window at the exit port. As seen in Figure 2.1 , the emerging beam first encounters the primary collimator, which has a diameter of 0.347 inch and nominally confines the beam divergence to an angular radius of 1.5 mr. The beam halo is attenuated downstream by scrapers, and two 1-kg permanent magnets sweep charged particles out of the beam and into the 4 inch lead wall containing the final scraper. The beam suffers an insignificant degree of absorption in the hydrogen target and continues through to the ion chamber and beam catcher where it is finally absorbed. The lead wall in front of the beam catcher is a backscatter shield and has a liberal aperture for the beam. The beam diameter at the center of the target is about 0.8 inch and comfortably fits inside the 1.5 inches diameter of the mylar cup containing the liquid hydrogen.

The elements of the beam monitoring system are: the ion chamber; a current integrator, and associated with it, a precision pulser; and a quantameter (for calibration purposes). The current integrator scaled the integrated beam energy in units called BIP's (Beam Integrator Pulses):

$$1 \text{ BIP} \cong 1.21 \times 10^{13} \text{ MeV} \quad .$$

Each time a BIP was registered, the PDP-5 computer inserted a special marker in the data. Independently, a mechanical scaler totaled the number of BIP's and ended the run at a preset number of BIP's.

A gas mixture of 90% Ne and 10% He inside the ion chamber is irradiated and partially ionized by the photon beam, and a 15 Kv/m electric field inside the chamber induces a measurable current in the closed path connecting the chamber electrodes. A Littauer type current integrator[15] measured the charge of ionization, which is proportional to the total energy of the beam. Before each run, the integrator was calibrated by recording its response to a number of pulses from the precision pulser, allowing us to convert BIP's to coulombs of charge. The relation between charge of ionization and integrated beam energy depends on properties of the ion chamber. Let $U_I$ denote the integrated energy per unit charge for the ion chamber: $U_I$ depends on photon energy, which we may indicate by writing $U_I(E_o)$, where $E_o$ is the synchrotron endpoint energy. As described below, we experimentally measured $U_I$ for several endpoint energies by comparison with a Wilson type quantameter[16]. Unlike an ion chamber, the quantameter calibration constant, $U_Q$, is virtually independent of photon energy and has the advantage of being known theoretically at least as well as experimentally[17].

The ion chamber was removed from the experiment occasionally and taken to another area of the synchrotron for calibration against the "South Beam" quantameter there. The photon beam passed through a

thin wall ion chamber and, further downstream, a lead aperture. Our procedure involved locating either the ion chamber or the quantameter squarely behind the lead aperture; we used the thin wall ion chamber to deliver the same amount of integrated beam energy to either device. We irradiated each device separately and measured the charge produced, using the same current integrator each time. For equal amounts of integrated beam energy, the ratio of the charges, $q_Q/q_I$, is the inverse of the ratio of the calibration constants, or $U_I/U_Q$. Figure 6.1 shows the results from one calibration session, where the ratio $U_I/U_Q$ is plotted versus $E_o$.

Gas leakage from the ion chamber made it necessary to replenish the gas mixture every four or five months. The pressure was deliberately maintained above atmospheric pressure to minimize contamination and to monitor the leakage. The time dependence of $U_I/U_Q$ was checked by taking measurements, as described above, both before and after each ion chamber refilling. Let $t_o$ denote the time of refilling. Linearizing $U_I/U_Q$ in both the time, t, and the endpoint energy, $E_o$, for $t_o < t <$ ($t_o$ of next refilling):

$$U_I(E_o,t)/U_Q = A(E_o - 0.9\ \text{GeV}) + B(t - t_o) + C,$$

where

$$A = 1.5\ /\ \text{GeV}$$

$$B = -0.0010\ /\ \text{day}.$$

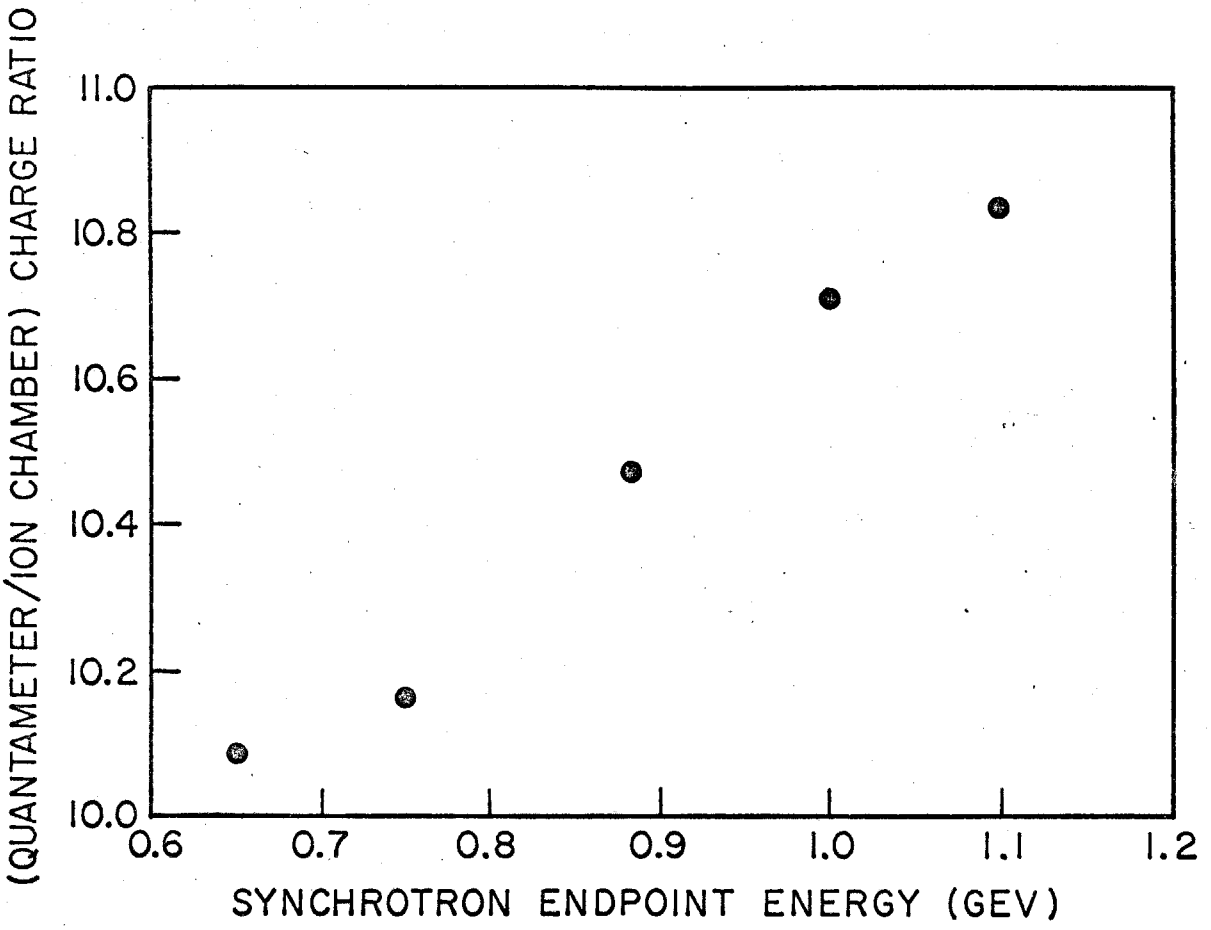


Figure 6.1 Charge Ratio, Quantameter to Ion Chamber, as a Function of Endpoint Energy

C is a constant characteristic of the time period between refillings:

| $t_o$ | C |
|---|---|
| 2/20/69 | 10.60 |
| 3/3/69 | 10.62 |
| 5/15/69 | 10.42 |
| 11/13/69 | 10.48 |

We use the theoretical value for $U_Q$, which is, for the South Beam quantameter at standard temperature and pressure,[17]

$$U_Q^{STP} = (4.80 \pm 0.15) \times 10^{18} \text{ MeV/coul} \quad .$$

The actual temperature and pressure for the quantameter were observed to be 25.8°C and 677 mm Hg (on November 11, 1969). The corrected value of $U_Q$, and the one we used in calibrating the ion chamber, is

$$U_Q = U_Q^{STP} \frac{(p/T)^{STP}}{p/T}$$

$$= (5.78 \pm 0.18) \times 10^{18} \text{ MeV/coul} \quad .$$

Let us now trace the steps in converting the number of BIP's, denoted B, to the corresponding amount of integrated beam energy, W. The latter is needed in any cross section measurement. The first step is to convert B to ion chamber charge, using the results of the current integrator calibration. Before each run, the current integrator was temporarily disconnected from the ion chamber and reconnected to a

precision pulser. The standard procedure was to record the number of BIP's produced by exactly 200 pulses, each pulse of which carried a charge of $503.75 \times 10^{-10}$ coulomb. Denoting the number of BIP's thus produced as $B_{200}$, we have the following expression for the ion chamber charge, $q_I$, in terms of the corresponding number of BIP's, B:

$$q_I = (200)(503.75 \times 10^{-10})B/B_{200} \text{ coul.}$$

The next step is to convert $q_I$ to $q_Q$, the charge expected for the quantameter in the same experimental configuration. This follows from the above parametrization for $U_I(E_o,t)/U_Q$ :

$$q_Q = q_I(q_Q/q_I) = q_I(U_I(E_o,t)/U_Q) .$$

Finally, $q_Q$ is converted to integrated beam energy via the theoretical value for $U_Q$. Collecting the above results, the integrated beam energy W, as a function of $B_{200}$, $E_o$, and t, is expressed in terms of B as follows:

$$W(B_{200}, E_o, t) = U_Q q_Q$$

$$= (5.78 \pm .18) \times 10^{18} \left(\frac{U_I(E_o,t)}{U_Q}\right) 200 \times 503.75 \times 10^{-10} B/B_{200} \text{ MeV.}$$

## 6.2 The Hydrogen Target

Two distinct types of target design were used in the course of the experiment. The earlier one was a simple type in which $LH_2$ (liquid hydrogen) is fed into the appendix from below and allowed to boil there at atmospheric pressure. An automatic cycling system

kept the appendix filled. Later on, a closed system, condensing type target suitable for hydrogen or deuterium was installed.

The construction of the original target is shown schematically in Figure 6.2 . The appendix, made of 0.005 inch clear mylar, is 6.050 inches long and 1.5 inches in diameter. The outer casing is made of 1/16 inch aluminum with 0.005 inch mylar beam windows. The space exterior to the appendix is pumped down to about 10 millimicrons pressure, while the appendix interior is at atmospheric pressure. Surrounding the appendix, with cutouts for the beam, is an aluminized mylar heat shield maintained at a temperature of $90^{\circ}K$ by conduction with a $LN_2$ (liquid nitrogen) jacket located above the appendix. In operation, $LH_2$ is forced up into the appendix by gaseous nitrogen at about two pounds overpressure. When the $LH_2$ fills the appendix and reaches a point on the appendix stem where a resistor is attached, the feed valve for the gaseous nitrogen is automatically closed.

The condensing target construction is shown in Figure 6.3. The length of the appendix was initially 6.639 inches, but was soon changed to 6.390 inches. It was later changed to 3.270 inches in order to improve kinematical resolution (at the expense of counting rate). Otherwise, the construction of the appendix, outer casing, $LN_2$ jacket and heat shield are the same as in the pressure fed target. The new features are a central condensing tube which attaches to the top of the appendix and an $LH_2$ jacket which surrounds the condensing tube. Gaseous hydrogen is introduced under pressure into the condensing tube, condensation proceeds on the tube wall, and the condensate collects in the appendix. To speed condensation, the

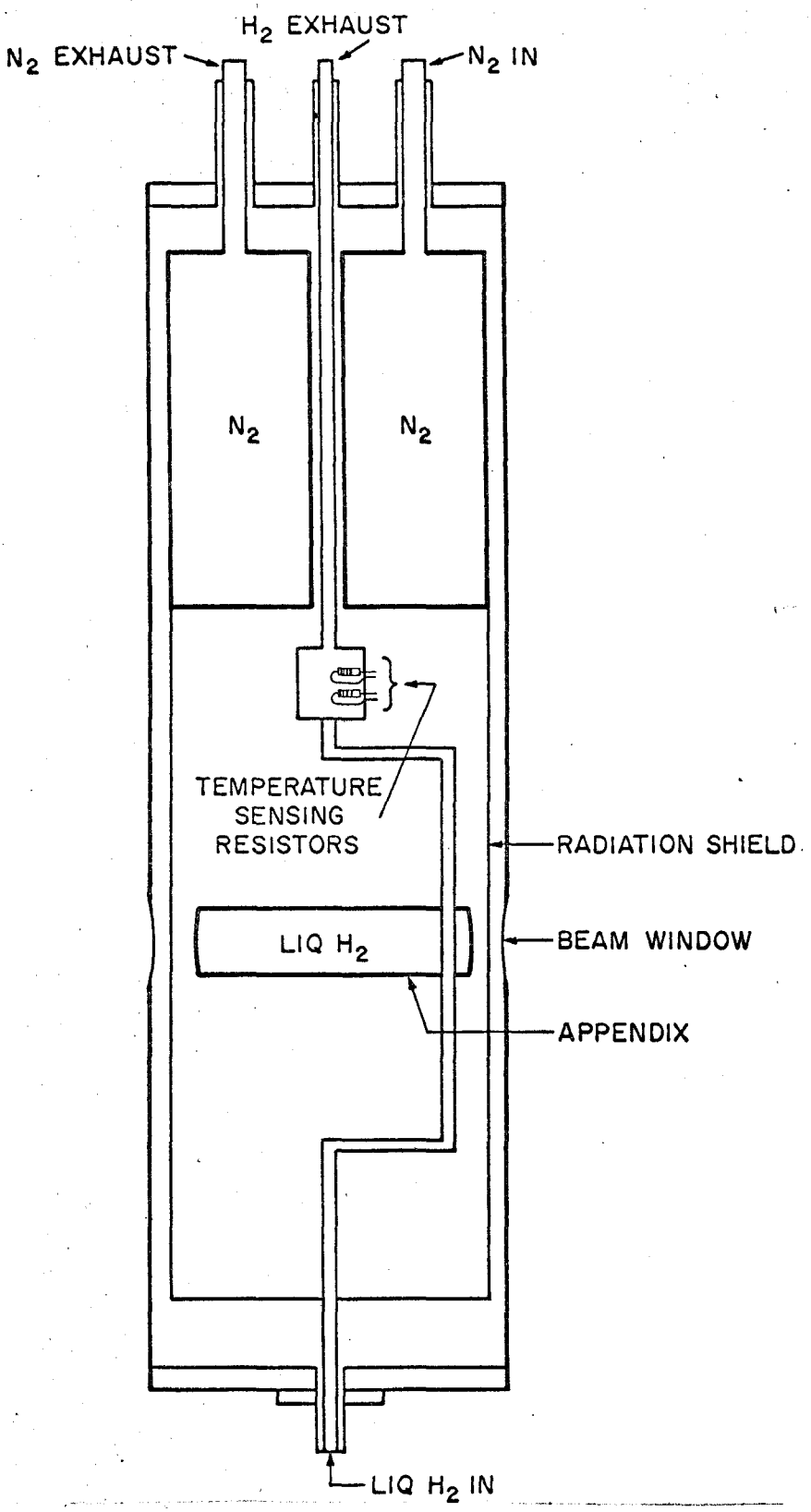


Figure 6.2 Force Fed Hydrogen Target

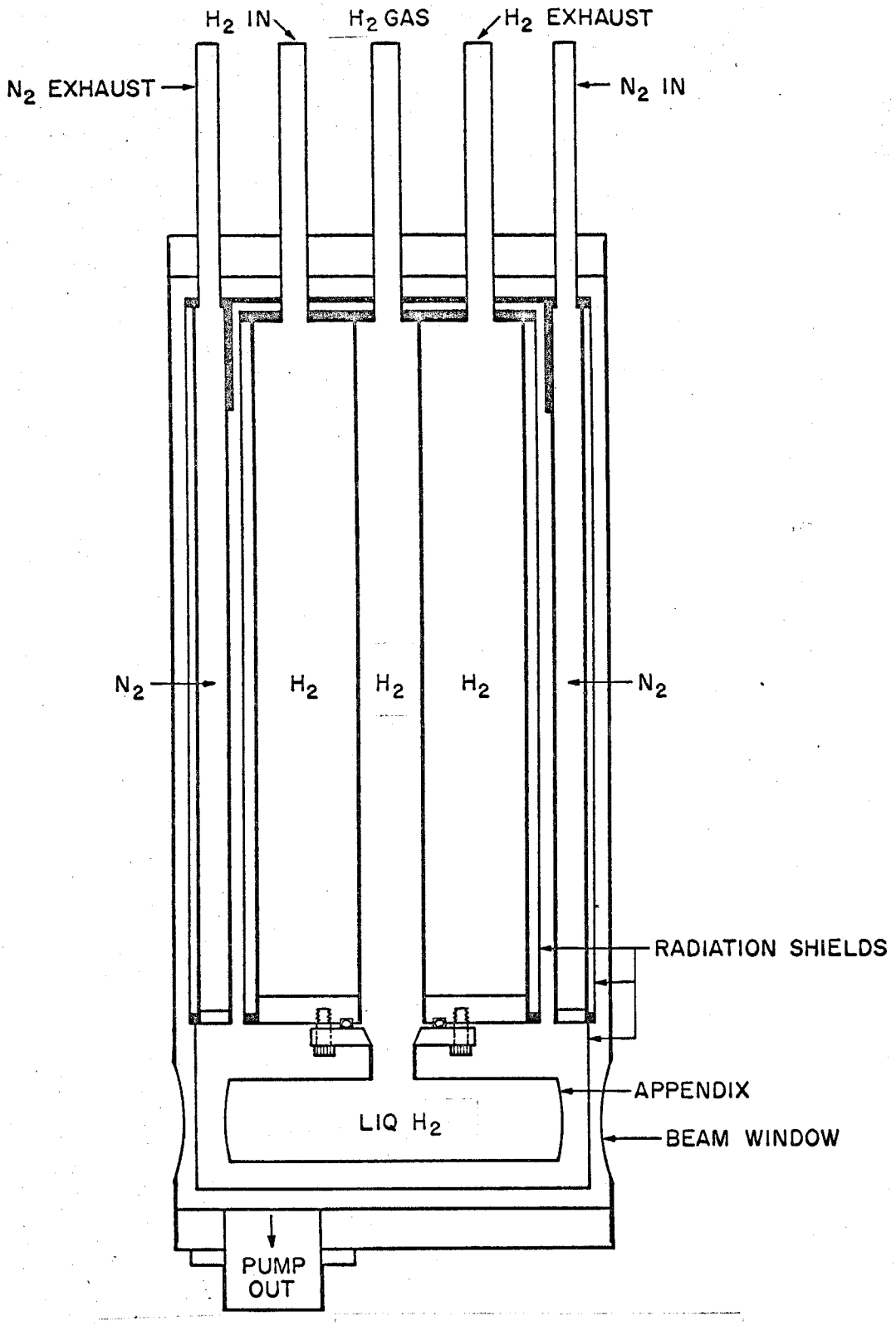


Figure 6.3 Condensing Type Hydrogen Target

boiling point of the $LH_2$ inside the jacket is lowered slightly by pumping down its vapor pressure. The filling time is about 20 minutes.

The aluminum outer casing had two cutouts for the beam windows, each 2 inches in diameter, and a 1 inch diameter cutout for the $30^{o}$ line surveying window. A photon from eta decay, unless it passed through one of these mylar windows, had to penetrate the 1/16 inch aluminum casing; for normal incidence, this amounts to about 0.018 radiation length.

The primary photon beam passed through four layers of 0.005 inch mylar, two layers from the appendix and two from the target beam windows. Each layer in the appendix, however, had been pressure formed and presented a thickness of about 0.003 mylar to the beam. The total empty target matter in the beam represents about 4% of the total number of nucleons presented to the beam by the filled target.

## 6.3 The Photon Telescopes

Each photon telescope consists of a lead aperture, veto counter and Cherenkov shower counter arranged as in Figure 2.1 . The lead apertures had a vertical width of 8 inches, and the horizontal width was variable. The horizontal width was variously 7 inches and 3.5 inches, and the thickness of the lead was 1.25 inches. The veto counter was made from 1/2 inch scintillator, in front of which was a 1/2 inch lucite shield to absorb soft electrons. The veto counter was in back of, and overlapped, the lead aperture, so that most photons which converted in the lead would be vetoed. The shower counter was positioned squarely behind the aperture and veto counter. The entire

unit was mounted on a trolley which could be rolled on a circular rail. An aluminum platform supported the telescopes. The trolleys had pointers attached to them which could be aligned with marks on the platform.

Each shower counter is constructed as shown in Figure 6.4. Two 14X14X6 inch blocks are joined with RTV compound to make a 14X14X12 inch block. The RTV does not provide an optical match, so that the joined blocks are optically distinct, but the combined phototube signal is rather insensitive to shower origin over the face of the block: a test of this point revealed less than 5% variation of mean shower pulse height for normal incidence. Seven XP1040 phototubes, each 5 inches in useful diameter, are joined to the back surface of the block using RTV compound, arranged as in Figure 6.5. Each phototube is shielded from stray magnetic fields with a jacket of Netic and Conetic metals. The soft iron box housing the lead glass provides additional magnetic shielding, although it was found necessary to wrap the box with about 40 windings of 0.020 inch transformer laminations.

A. Calibration

The energy calibration of the two shower counters was performed in another area of the experimental hall, using a momentum-selected positron beam located there.[18] The positrons were pair-produced at an auxiliary outlet of the synchrotron's "South Beam," and a magnetic spectrometer defined a beam with a momentum width of about 3%. A final defining counter restricted the beam spatially to

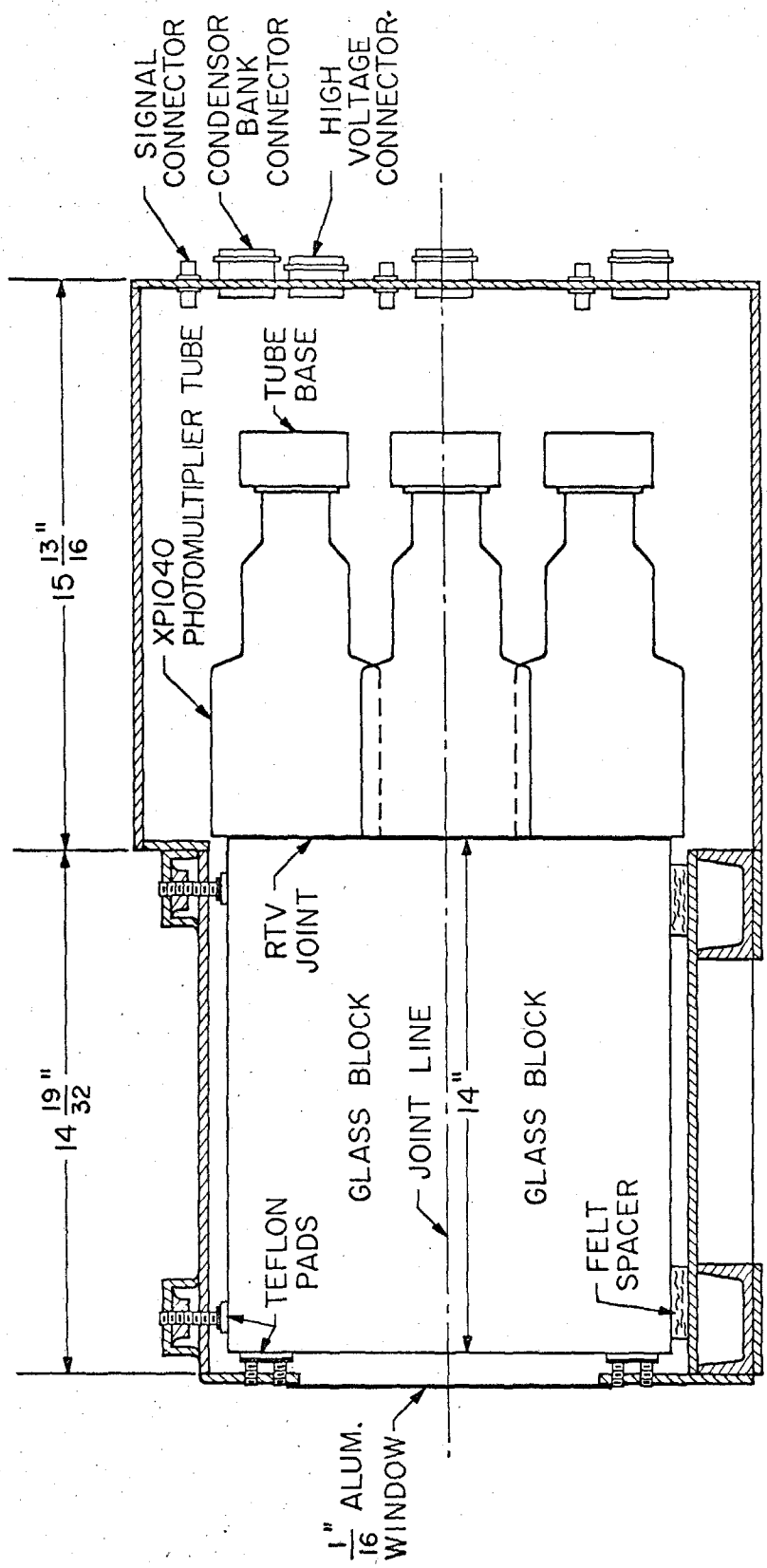


Figure 6.4 Shower Counter, Side View

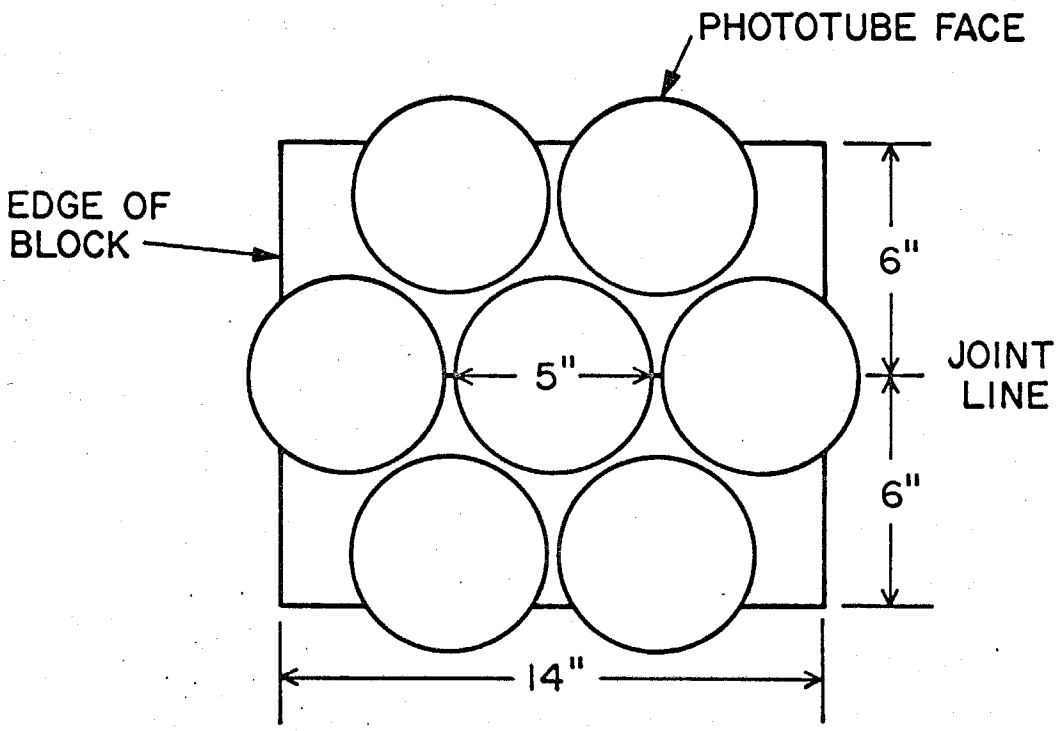


Figure 6.5 Phototube Arrangement in Shower Counter

a 1 $cm^2$ cross section, and the shower counter to be calibrated was placed immediately downstream. For each shower counter, the signals from the seven phototubes were passively averaged, and the averaged signal was pulse height analyzed. About $10^4$ counts were collected for each of various settings of the positron energy (controlled by the magnet current). The mean pulse height is plotted against the energy in Figure 6.6, where the straight line is a linear fit to the data.

We desired a secondary energy standard to retain the results of the positron beam calibration. Thus, a light source was constructed by attaching a Bi-207 radioactive source to a small cube of scintillator material. One source-scintillator was fashioned for each shower counter and glued to the front surface of the lead glass, straddling the joint line of the two smaller lead glass blocks. It was necessary, of course, to locate the source-scintillator in the shadow of the lead aperture. When a shower counter was triggered on its own internal light, the pulse height spectrum was dominated by the source-scintillator, as seen in Figure 6.7. The peak in that spectrum, caused by Auger electrons, served as a secondary energy standard by comparison with positron-induced showers; the light output is comparable to a 200-MeV shower.

Let $E_S$ denote the shower energy which corresponds to the Auger peak, and let $\mu_S$ denote the corresponding mean pulse height. We express the linear fit seen in Figure 6.6 by writing

$$E_+ = (E_s - E_o)\, \mu/\mu_S + E_o \qquad (6.1)$$

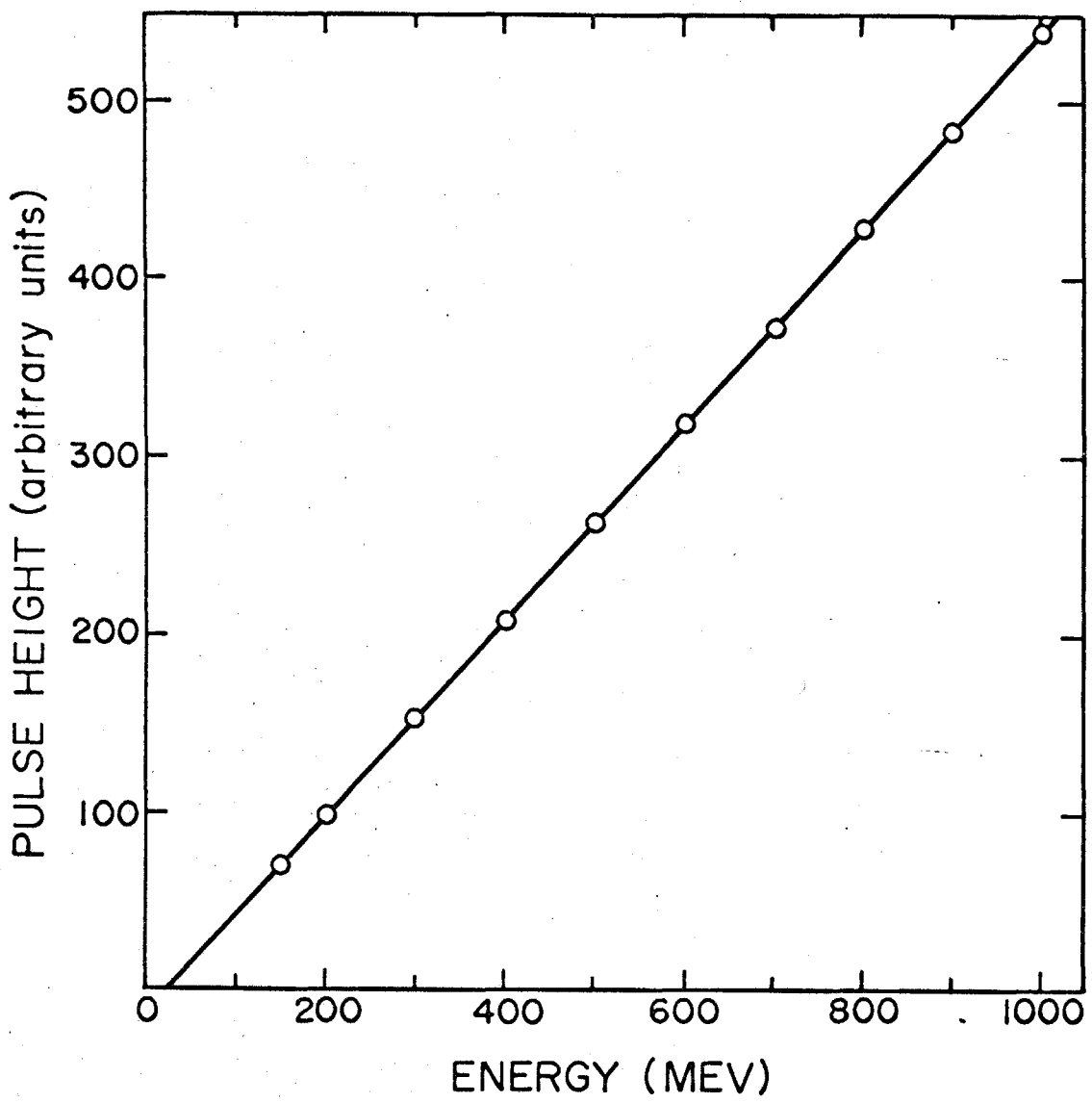


Figure 6.6 Mean Pulse Height as a Function of Shower Energy

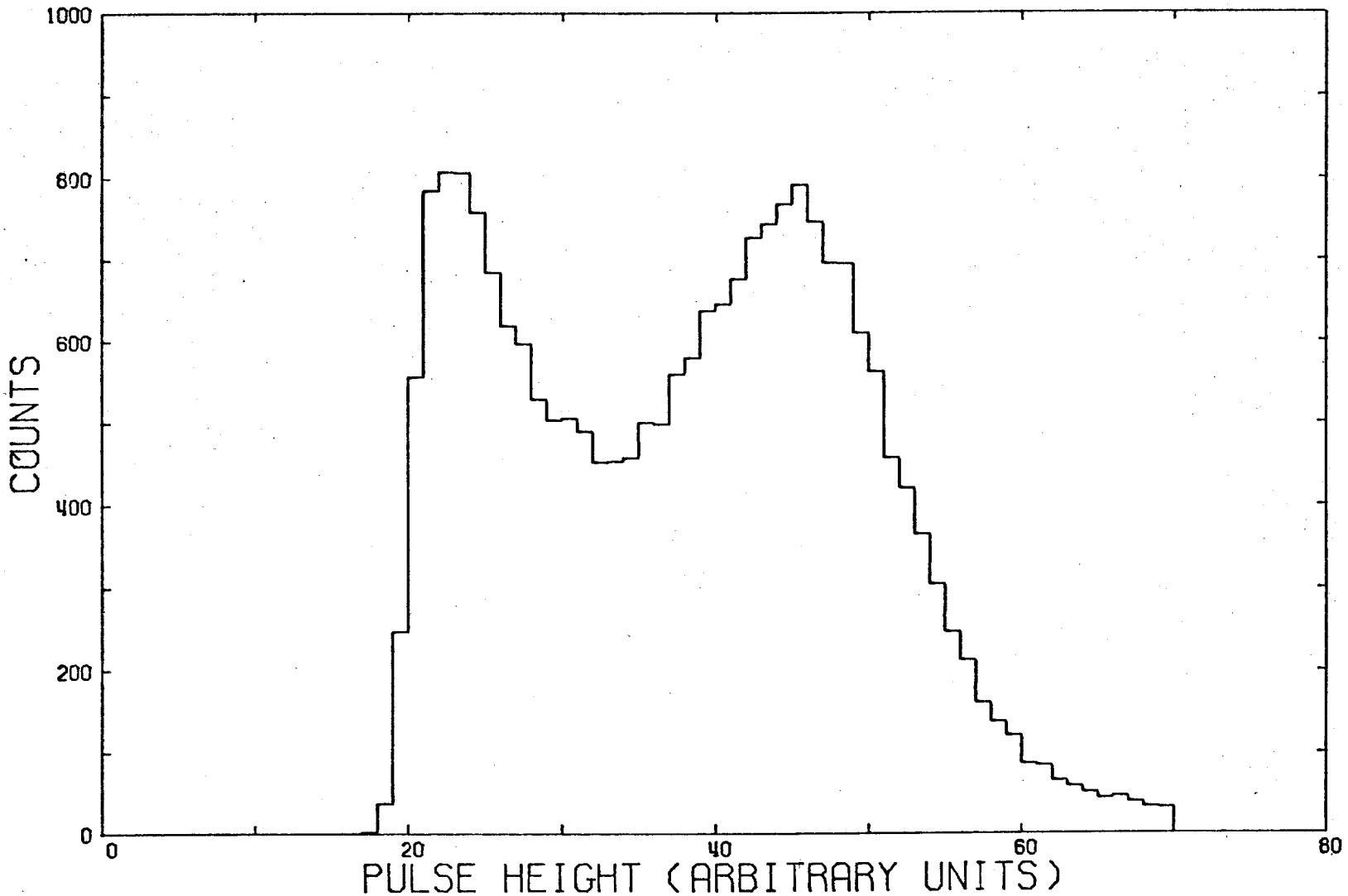


Figure 6.7 Pulse Height Spectrum of Bi-207 Source

where

$E_+$ = positron energy

$\mu$ = mean pulse height

$E_o$ = constant.

$E_S$ was determined to be 170 MeV for one counter and 215 MeV for the other, but different values were obtained in different calibration sessions. The "energy pedestal," $E_o$, suffered similar fluctuations in repeated measurements, but a value of 10 MeV was typical. Since incident photons produce showers quite similar to those of positrons, Eq. 6.1 provided a tentative calibration for the pulse heights obtained in the experiments, where $E_+$ is replaced by the photon energy, $E_\gamma$. Before each run, the value for $\mu_S$ was measured for each counter by examining the source-scintillator spectrum.

The calibration described above proved inadequate for any sensible data analysis. As described in Section 3.5 , it proved possible to re-determine values for $E_S$ within the data analysis; these came out as 150 MeV for one counter and 175 for the other, with errors of about 5 MeV.

B. Resolution

The energy resolution of the shower counters was examined using the positron beam, although the 3% momentum width of that beam must be taken into account. Let $n_e$ denote the mean number of photoelectrons, summed over the seven phototubes of a shower counter. As explained below, the averaged signal for the seven phototubes will behave like that of a single phototube with $n_e$ photoelectrons, provided

that the individual phototube gains are equalized. By "gain" we mean the constant which converts the number of photoelectrons to a pulse height. Denoting the gain by g and the mean pulse height by $\mu$, we have that

$$\mu = g n_e \ . \tag{6.2}$$

If the number of photoelectrons were distributed in a Poisson spectrum from random phototube fluctuations, then the variance of the pulse height, $\sigma^2$, would be given by

$$\sigma^2 = g^2 n_e \ , \tag{6.3}$$

and the following relation would obtain:

$$\left(\frac{\mu}{\sigma}\right)^2 = n_e \ .$$

Figure 6.8 is a plot of $(\mu/\sigma)^2$ against positron energy. The shower counters were so designed that $n_e$ should be proportional to incident particle energy[19], but Figure 6.8 shows a marked deviation from that rule. However, Eq. 6.3 neglects the finite beam momentum width. This width, denoted $\sigma_p/p$, modifies the expression for the variance to read

$$\sigma^2 = g^2 n_e + \mu^2 (\sigma_p/p)^2 \ ,$$

and

$$\left(\frac{\mu}{\sigma}\right)^2 = \frac{n_e}{1 + n_e(\sigma_p/p)^2} \ .$$

Since we believe that $n_e$ is proportional to energy, we write

$$n_e = k_e E_+ \ ,$$

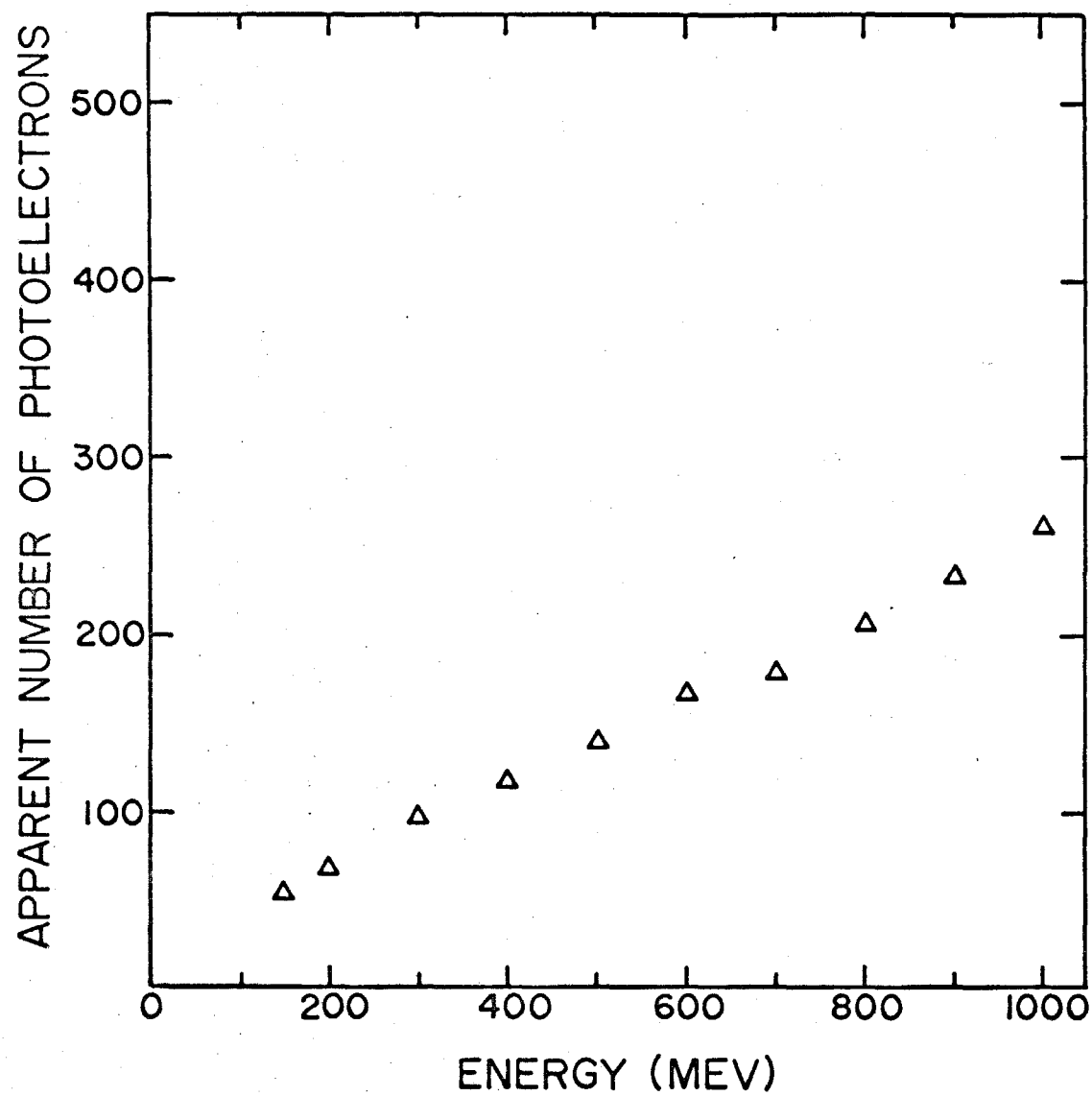


Figure 6.8 Apparent Number of Photoelectrons as a Function of Photon Energy

where $E_+$ is the positron energy. Not trusting the figure of 3% for the momentum width, we sought to measure both $k_e$ and $(\sigma_p/p)^2$ by fitting the data of Figure 6.8 with the above parametrization for $(\mu/\sigma)^2$. The results were, for shower counters "1" and "2",

| | 1 | 2 |
|---|---|---|
| $k_e$ $(MeV^{-1})$ | 0.352 | 0.344 |
| $\sigma_p/p$ | 0.035 | 0.040 |

These values for $k_e$ do not suffice to describe the observed resolution of eta events, as explained in Section 3.5. Assuming that one value describes both shower counters, we determine $k_e$ within the data analysis.

C. Gain Matching

For each shower counter, the signals of the seven phototubes were averaged into one signal for pulse height analysis. As shown below, the resolution of the averaged signal is optimized by equalizing the individual phototube gains, a process we refer to as gain matching.

The light source for gain matching was a set of light-emitting diodes connected in series and driven by an SKL type fast pulser. Each shower counter had such a string of light-emitting diodes taped to the front surface of the lead glass. The gain matching procedure involved analyzing the pulse height spectrum of each phototube individually and adjusting the voltage of that phototube until the gain was near a desired common value. The PDP-5 computer assisted in this task.

We matched the gains at the rate of about once a week, and the phototubes were sufficiently stable that only minor voltage corrections were necessary.

The following argument is due to S. J. Yellin[5]: consider the vectors A and B, defined by

$$A_i = \sigma_i$$

$$B_i = \mu_i/\sigma_i$$

where subscript i denotes the $i^{th}$ individual phototube for one shower counter (non-subscripted quantities refer to the summed signal). Thus,

$$A \cdot A = \sum_i \sigma_i^2 = \sigma^2$$

$$B \cdot B = \sum_i (\mu_i/\sigma_i)^2 = \sum_i n_{e_i}$$

$$A \cdot B = \sum_i \mu_i = \mu \quad .$$

Using Schwartz's inequality,

$$(A \cdot B)^2 \leq A^2 B^2 ,$$

or

$$\mu^2 \leq \sigma^2 \sum_i n_{e_i}$$

$$\left(\frac{\mu}{\sigma}\right)^2 \leq \sum_i n_{e_i} \qquad (6.4)$$

The number of photoelectrons is independent of the phototube voltage, so that the right side of 6.4 is a constant. The equality holds

when vectors A and B are parallel, for which case $(\mu/\sigma)^2$ is maximum and equal to the total number of photoelectrons, as for a single phototube. This occurs when

$$A_i = \alpha B_i$$

or

$$\sigma_i = \alpha \frac{\mu_i}{\sigma_i}$$

$$\frac{\sigma_i^2}{\mu_i} = \alpha \quad ,$$

where $\alpha$ is any constant. But, from Eqs. 6.2 and 6.3, $(\sigma^2/\mu)_i$ is just the gain of the $i^{th}$ phototube. Therefore, the individual gains must be set to some common value in order that the summed (or averaged) phototube signal have optimum resolution, for which case

$$(\mu/\sigma)^2 = \sum_i n_{e_i} \quad . \tag{6.5}$$

The light-output width of the light-emitting diodes was unknown, but an indirect measure was afforded by checking Eq. 6.5 after the gains had been matched: For one such check, the number of photoelectrons was 154 for the left-hand side and 160 for the right-hand side.

## 6.4 Operating Procedure

Before beginning a data collection run, the synchrotron was adjusted to operate at the desired endpoint energy, and then the shower counters were moved to the desired angle with respect to the beam line. Polaroid film was exposed by the synchrotron beam at a point downstream

of the hydrogen target, in order to check that the maximum photon intensity (the "hot spot") was properly centered within the beam envelope. If necessary, the internal radiator was re-oriented by remote control in order to center the hot spot.

The current integrator which measured the ion chamber charge was calibrated by measuring its response to a known amount of charge. The phototube voltages for the shower counters were set to values determined from the most recent gain measurement session, and the veto counter voltages were set to values from the most recent observation of the veto counter spectra. The various electronic bias adjustments were similarly set and the transistor power supplies were adjusted to standard voltages. The pulse height analyzing system was calibrated in a two-part procedure. First, an SKL fast pulser was operated so as to generate a number of artificial events ("fiducial" events) for two settings of the SKL output voltage, and the mean pulse heights for the two settings were recorded for both channels of the Nuclear Data pulse height analyzer. Second, the source-scintillator pulse height spectrum was exhibited for each shower counter in turn, and the pulse height associated with the Auger electron peak in that spectrum was recorded.

The PDP-5 computer assisted in the above pulse height measurements, and the results became part of the first record to be transferred to magnetic tape for the run in question. Further information for the first record was automatically requested by the computer, and it was supplied manually through a teletype. That information included

the integrator calibration, the endpoint energy, the shower-counter-to-beam-line angle, the date and time, and any comments. After it had written the first record on tape, the computer was started in the data collection mode, all scalers were set to zero, and the synchrotron was started. Data collection began as soon as one unit of beam (one "BIP") had been registered.

The synchrotron produced a square well type of dump lasting about 60 ms or 120 ms, depending on whether the cycle rate was 2/sec or 1/sec, respectively. When the endpoint energy was less than about 900 MeV, the shorter dump was used, while the longer dump was used at higher energies. The beam intensity typically varied by a factor of two from one dump to another. The peak intensity was controlled by the synchrotron tuning, and it was necessary to de-tune the synchrotron for some runs, when the counting rate was especially high. The dump occassionally developed undesirable spikes, resulting in events with especially large pulse heights. The experimental apparatus for detecting two-gamma events was gated on a signal which encompassed the period of the dump.

The PDP-5 computer was programmed to remotely fire the SKL pulser, so as to inject a fiducial event into the electronics, every time a preset number of gates had been registered. Such an event always preceded the build-up of the dump, so as not to contribute to the dead time. Fiducial events were tagged as such by the computer, by switching on an unused bit of the word containing the time difference pulse height. In a table of pulse heights collected experimentally,

the fiducial events stand out in the tagged time difference by displaying only minor changes in each of the three pulse heights which define an event. Each time another unit of beam was registered, the PDP-5 inserted a special marker in the collected data at that point; these markers similarly stand out in a table of pulse heights, by having special unchanging values for each of the three pulse heights. The computer data buffer had room for a certain number of events, variously 340 and 210, and when the buffer became filled, it was transferred to magnetic tape and cleared for refilling.

When the computer was not busy with incoming data, it calculated points for an oscilloscope display. Three pictures taken from actual running are reproduced in Figure 2. 3 . The top two pictures are pulse height tables, where the index runs from left to right, for those events currently contained in the data buffer. The bottom picture is a four-in-one histogram display for the three pulse heights in each event plus the geometric mean of the two pulse heights representing the shower energies. The latter quantity scales like the two-photon invariant mass, and eta events are visible in this spectrum as a peak (see Figure 3. 9 ). The top picture is a pulse height table for the time difference. The pulse height values cluster at about half way along the ordinate for true coincidences, while accidental coincidences are scattered over the ordinate. The very tight cluster near the top is due to the fiducial events. About half way between these clusters is a tenuous cluster of five points, caused by the special beam unit markers. The middle picture is a pulse height table for one of the

shower counter signals, with similar but obscured features as the time difference table above. The histograms in the bottom picture display, from left to right, the geometric mean of the shower signals, the time difference, the shower signal for one counter, and the same signal for the other counter.

The oscilloscope displays were valuable in spotting equipment failures, and it was most helpful to have an on-line display which exhibited the eta mass peak. The displays, as well as the scalers, were given spot checks throughout a run, and a Polaroid picture of the histogram display was taken at the end of the run.

At the end of a run, the computer transferred its data buffer to magnetic tape and requested certain information through the teletype. That information, which was written on tape as the final record of the run, included the scaler readings, the date and time, and any comments.

## 6.5 Timing Optimization

As mentioned in Section 3.2, zero-crossing discriminators were used at strategic points in the electronics to minimize discriminator "slewing" in the time difference measurement system. We might have compensated for the residual slewing by direct measurement, but this was not done. Instead, we deduced, and compensated for, the amount of residual slewing using the data produced by the two shower counters. The slewing-compensated timing spectrum shows a narrower coincidence peak, as seen in Figure 6.9b for the uncompensated data of Figure 6.9a. We now explain how the slewing correction is made.

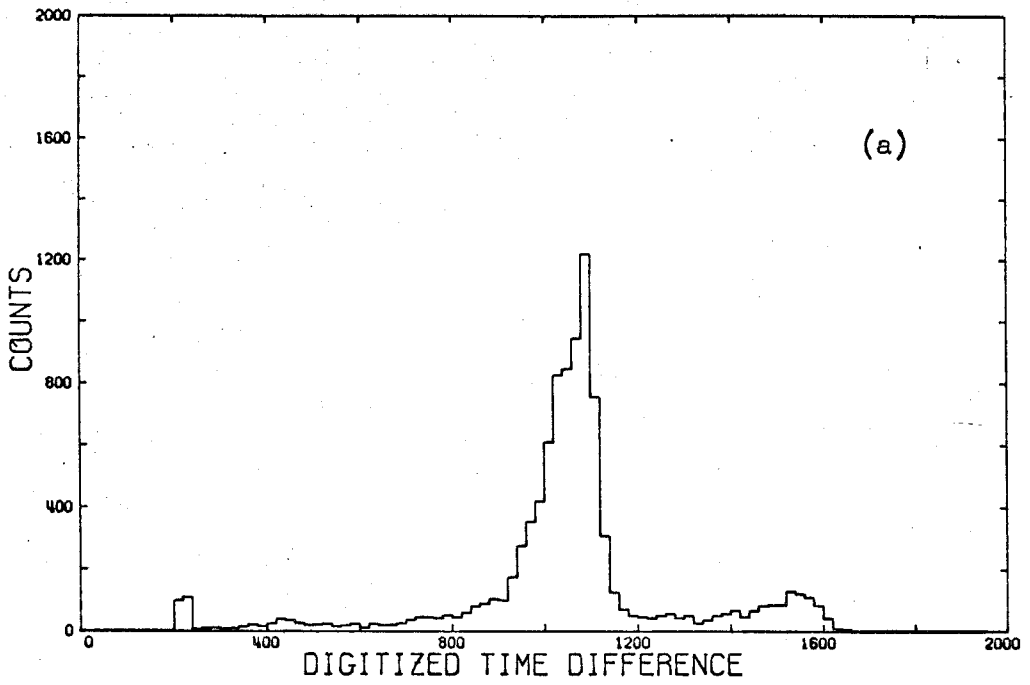


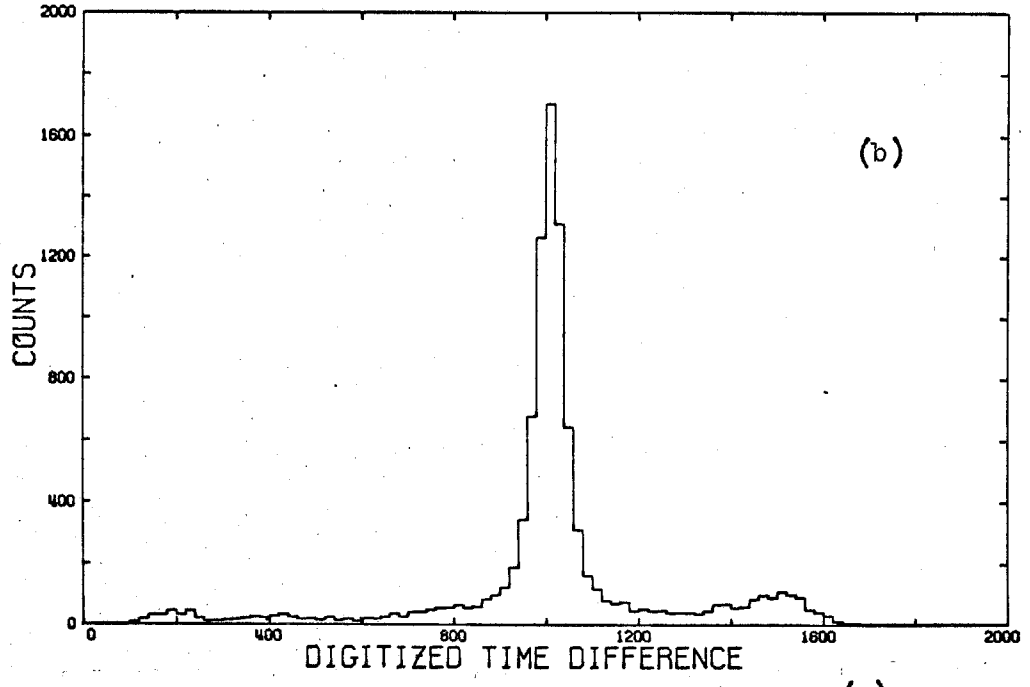


Figure 6.9 Time Difference Spectrum, Before(a) and after (b) Slewing Compensation

Slewing makes the timing pulse height, $t_{12}$, dependent on the shower counter pulse heights, $e_1$ and $e_2$, as follows:

$$t_{12} = t_{12}^{(true)} + T(e_1, e_2) .$$

The matrix T, which describes the effect of slewing, separates in $e_1$ and $e_2$:

$$T(e_1, e_2) = T_1(e_1) + T_2(e_2) , \qquad (6.6)$$

where the vectors $T_1$ and $T_2$ describe the slewing in the individual arms of the circuitry which produces the time difference signal (see the electronics block diagram, Figure 2.2 ). The matrix T was experimentally measured by examining the $t_{12}$ spectrum for events with fixed values of $e_1$ and $e_2$ (actually, $e_1$ and $e_2$ after a coarser binning); the maximum in the $t_{12}$ spectrum was studied as a function of $e_1$ and $e_2$. Denote the value of $t_{12}$ at maximum by $T^{exp}(e_1, e_2)$. We fit $T^{exp}$ by a term of the form (6.6), where each element of vectors $T_1$ and $T_2$ is a free variable; we minimize S, where S is given by

$$S = \sum_{e_1, e_2} N(e_1,e_2) \, (T^{exp}(e_1,e_2) - T_1(e_1) - T_2(e_2))^2 ,$$

where the weighting factor, $N(e_1, e_2)$, is the number of events in the $(e_1, e_2)$ bin. Minimizing S with respect to each element of $T_1$ and $T_2$ independently, leads to the coupled conditions

$$T_1(e_1) = \frac{\sum_n N(e_1,n)(T^{exp}(e_1,n) - T_2(n))}{\sum_n N(e_1,n)}$$

$$T_2(e_2) = \frac{\sum_m N(m,e_2)(T^{exp}(m,e_2) - T_1(m))}{\sum_m N(m,e_2)} \qquad (6.7)$$

The solutions for $T_1$ and $T_2$ are not unique with respect to the trivial transformation

$$T_1 \rightarrow T_1 + C$$

$$T_2 \rightarrow T_2 - C \ ,$$

where C is a constant. Approximate solutions for $T_1$ and $T_2$ were obtained by iterating Eqs. 6.7 starting from a trial guess. This approach is very similar to, and was in fact motivated by, the background fitting method described in Section 3.3. Figure 6.10 displays the results for $T_1$ and $T_2$ (the "slewing functions") in a typical case, where the abscissa is either $e_1$ or $e_2$ after calibration in terms of the corresponding photon energies.

## 6.6 Maximum Likelihood Method

In this section, the simple "spectrum factoring" technique introduced in Section 3.3 is extended to apply to a wider class of fitting regions than the simple rectangular region employed there. It is shown that this approach amounts to a maximum likelihood description in terms of binned quantities. Finally, the maximum likelihood

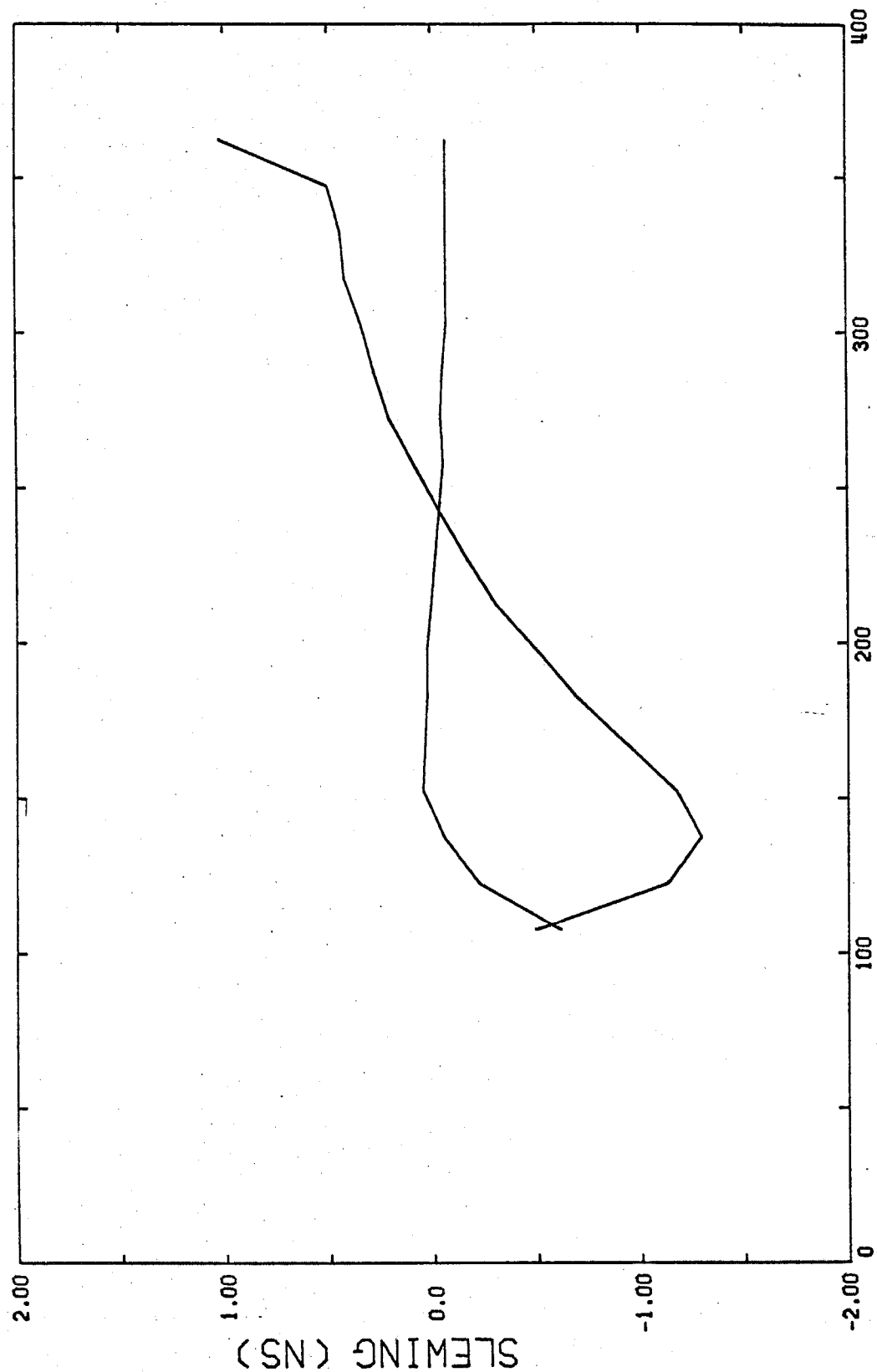


Figure 6.10 Slewing Compensation as a Function of Photon Energy

formulation is augmented with a term describing eta events, for fitting data containing a mixture of background and eta events. To begin, we consider the problem of describing background data alone.

For the set of bins defined by

$$(i_1, i_2) \epsilon R,$$

we wish to describe the matrix $N(i_1, i_2)$ with another matrix, $F(i_1, i_2)$, defined by

$$F(i_1, i_2) = F_1(i_1) F_2(i_2) \quad .$$

The vectors $F_1$ and $F_2$ are to be determined by some fitting criterion. Suppose that F is required to be normalized to N within each row and column independently, consistent with the region R. To express this idea more precisely, consider the following subsets of R:

$$R(i_1) = \{ n \mid (i_1, n) \epsilon R \}$$

$$R(i_2) = \{ m \mid (m, i_2) \epsilon R \} \quad .$$

For each $i_1$ such that $R(i_1)$ is not empty, normalization within $R(i_1)$ requires that

$$\sum_{n \epsilon R(i_1)} F(i_1, n) = F_1(i_1) \sum_{n \epsilon R(i_1)} F_2(n) = \sum_{n \epsilon R(i_1)} N(i_1, n), \quad R(i_1) \neq \{0\}$$

Similarly, normalization within $R(i_2)$ requires that

$$\sum_{m\epsilon R(i_2)} F(m,i_2) = F_2(i_2) \sum_{m\epsilon R(i_2)} F_1(m) = \sum_{m\epsilon R(i_2)} N(m,i_2), \; R(i_2) \neq \{0\} .$$

These are coupled relations for $F_1$ and $F_2$, or at least for those elements of $F_1$ and $F_2$ which correspond to non-empty sub-regions of R. One way to find $F_1$ and $F_2$ is by iteration of those relations, rewritten as

$$F_1(i_1) = \frac{\sum_{n\epsilon R(i_1)} N(i_1,n)}{\sum_{n\epsilon R(i_1)} F_2(n)} \tag{6.8a}$$

$$F_2(i_2) = \frac{\sum_{m\epsilon R(i_2)} N(m,i_2)}{\sum_{m\epsilon R(i_2)} F_1(m)} \tag{6.8b}$$

For example, one may start with a trial guess for $F_2$. Then (6.8a) furnishes a guess for $F_1$. This guess for $F_1$ may be used to improve the guess for $F_2$ using (6.8b) and so on. The solution will not be unique, but the product of $F_1$ and $F_2$, i.e., F, will be unique.

Instead of a normalization requirement, suppose that F is to represent the expectation value for N, bin by bin. Then $F_1$ and $F_2$ which maximize the likelihood of this description can be found. From the Poisson distribution, the probability, P, that an experiment will produce N, as it actually appeared within the region R, is given by

$$P = \prod_{(m,n)\epsilon R} \frac{e^{-F(m,n)}[F(m,n)]^{N(m,n)}}{N(m,n)!}$$

$$= \prod_{(m,n)\epsilon R} \frac{e^{-F_1(m)\,F_2(n)}[F_1(m)\,F_2(n)]^{N(m,n)}}{N(m,n)!} \qquad (6.9)$$

The value of $F_1(i_1)$ which maximizes P is determined by

$$\sum_{n\epsilon R(i_1)} \left[\frac{N(i_1,n)}{F_1(i_1)} - F_2(n)\right] = 0 \qquad (6.10a)$$

and the value of $F_2(i_2)$ which maximizes P is determined by

$$\sum_{m\epsilon R(i_2)} \left[\frac{N(m,i_2)}{F_2(i_2)} - F_1(m)\right] = 0 \quad . \qquad (6.10b)$$

The above relations in $F_1$ and $F_2$ are seen to be formally equivalent to those of the normalization approach, Eqs. 6.8.

Either of the above approaches, normalization or maximum likelihood, is suitable for describing the matrix $N(i_1, i_2)$ if N contains only an uncorrelated background spectrum. Suppose, however, that there is an eta peak in the spectrum of N, and that a term to describe that peak, denoted $Y(i_1, i_2)$, is added to F:

$$F(i_1,i_2) = F_1(i_1)F_2(i_2) + Y(i_1,i_2)$$

The problem of finding $F_1$ and $F_2$, where Y is considered a constant term, distinguishes the normalization approach from the maximum likelihood approach. The normalization approach amounts to fitting $(F_1\ F_2)$ to $(N - Y)$; the maximum likelihood approach, while more complicated, furnishes the better description. The expression for P, Eq. 6.9, becomes

$$P = \prod_{(m,n)\in R} e^{-[F_1(i_1)\ F_2(i_2) + Y(i_1,i_2)]}$$

$$\times \frac{[F_1(i_1)\ F_2(i_2) + Y(i_1,i_2)]^{N(i_1,i_2)}}{N(i_1,i_2)!}$$

and the relations in $F_1$ and $F_2$, Eqs. 6.10, become

$$\sum_{n\in R(i_1)} \left[\frac{N(i_1,n)\ F_2(n)}{F_1(i_1)\ F_2(n) + Y(i_1,n)} - F_2(n)\right] = 0$$

(6.11)

and $$\sum_{m\in R(i_2)} \left[\frac{N(m,i_2)\ F_1(m)}{F_1(m)\ F_2(i_2) + Y(m,i_2)} - F_1(m)\right] = 0 \quad .$$

The presence of the eta term, $Y(i_1, i_2)$, makes it impossible to isolate $F_1$ and $F_2$ in the manner of Eqs. 6.8. However, it is still feasible to iterate these relations as a way of finding $F_1$ and $F_2$. Simple manipulation of Eqs. 6.11 leads to

$$F_1(i_1) = \frac{\sum_{n\epsilon R(i_1)} \frac{N(i_1,n)\, F_2(i_1)\, F_2(n)}{F_1(i_1)\, F_2(n) + Y(i_1,n)}}{\sum_{n\epsilon R(i_1)} F_2(n)}$$

$$F_2(i_2) = \frac{\sum_{m\epsilon R(i_2)} \frac{N(m,i_2)\, F_1(m)\, F_2(i_2)}{F_1(m)\, F_2(i_2) + Y(m,i_2)}}{\sum_{m\epsilon R(i_2)} F_1(m)} \qquad (6.12)$$

Actually, this "simple manipulation" has an important effect on the solutions. For example, one must stipulate that the solution of Eqs. 6.11 may not allow F to be negative, since F is an expectation value. On the other hand, if one begins with positive $F_1$ and $F_2$ in Eqs. 6.12, then F will automatically be restricted from being negative. One may verify that, had F been defined as

$$F(i_1, i_2) = F_1^2(i_1)\, F_2^2(i_2)$$

the result for F would coincide with that obtained from iteration of Eqs. 6.12 after starting with a non-negative initial guess for either $F_1$ or $F_2$. This point is almost trivial when Y identically vanishes, since then no restriction is needed to keep F non-negative.

From the point of view of the background fitting problem, the eta events are seen as a kind of unwanted "background". The term $Y(i_1, i_2)$ is introduced in the above formalism for the purpose of effectively subtracting the unwanted "background" of eta events from

$N(i_1, i_2)$. Another type of event which logically belongs in this category is the accidental coincidence, which so far has not been distinguished from the true background. If we know the spectrum of accidental coincidences, denoted $A(i_1, i_2)$, then we should replace Y with (Y + A) in every formula above. We obtained an estimate of A, and made that replacement, following the procedure outlined below.

We obtain an essentially pure sample of accidental coincidences by selecting events with $t_{12}$ values far from the coincidence peak (see Figure 3.6). The $(i_1, i_2)$ spectrum of such events, denoted $A^o(i_1, i_2)$, is "smoothed" by fitting it with a term of the form $A_1(i_1)A_2(i_2)$, using precisely the fitting methods developed above. This term is then normalized to $T_A$, the expected number of accidental coincidences which survived the timing cut and appear in N. The result is our estimate for $A(i_1, i_2)$. The estimation of $T_A$ involves an extrapolation of the $t_{12}$ spectrum of accidental coincidences into the region of the coincidence peak, which led us to perform a special test. The signal from one shower counter was delayed by 100 ns, which is the period for one orbit of the electron beam in the synchrotron. (Electron "bunching" in the synchrotron increases the probability for an accidental coincidence at multiples of 25 ns, since there were four bunches in the orbit.) The $t_{12}$ spectra obtained for such a test, performed on two different occasions, appear in Figure 6.11. The top spectrum shows a clear peak at the expected place, and this structure is expected for accidental coincidences in the undelayed $t_{12}$ spectrum, Figure 3.6. However, the bottom spectrum in Figure 6.11, produced by the same test performed later in the experiment, has a markedly suppressed peak.

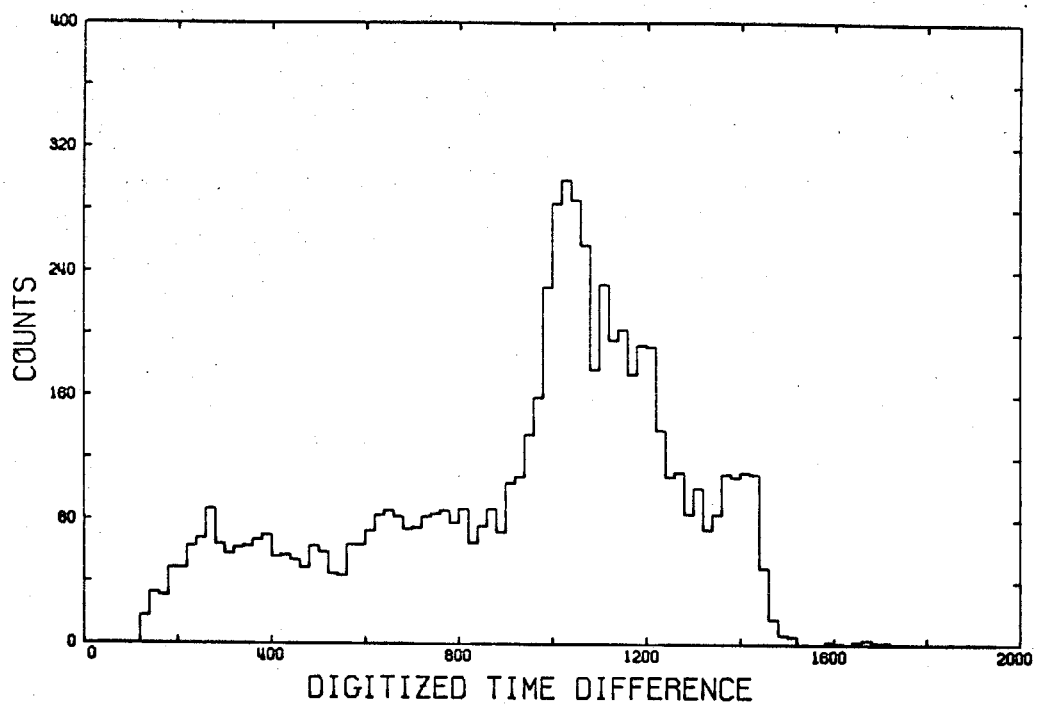


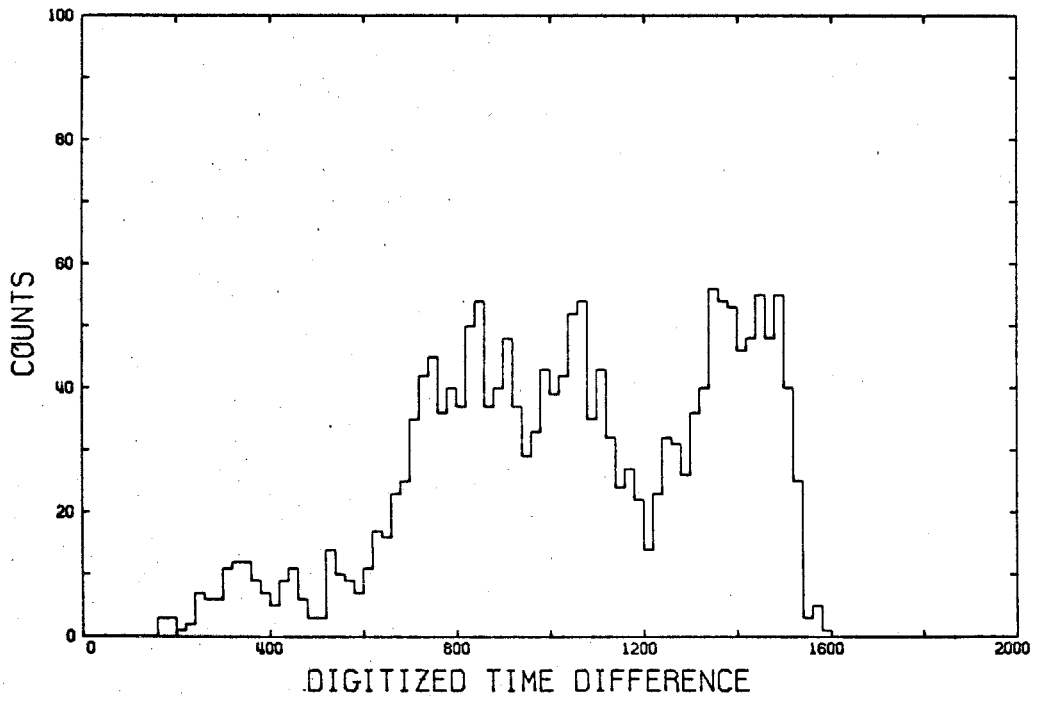


Figure 6.11 Two Examples of Time Difference Spectrum Obtained with 100 ns Delay Between the Shower Counters

Faced with these conflicting results, we elected to extrapolate the $t_{12}$ spectrum into the region of the coincidence peak, using linear interpolation between the bands on either side of the coincidence peak. This provides a dubious estimate of $T_A$, although it is shown in Section 3.7 that the estimated number of etas is practically insensitive to this quantity.

## 6.7 Efficiency Calculation

This is an outline of the Monte Carlo type computer program which estimates the detection efficiency. The results are used at two levels in the data analysis: in the description of the $(E_1, E_2)$ distribution of eta events, Section 3.4 ; and in the cross section unfolding, Section 3.6 . Sub-Section A below details the more exotic features of the Monte Carlo calculation, while B describes an entirely different, closed form type of calculation. The latter is only approximately valid, asymptotically approaching the true efficiency as the incident photon energy increases. The results of this method are in good agreement with those of the Monte Carlo method for photon energies well above threshold.

### A. Monte Carlo Calculation

The Monte Carlo type computer program simulates eta photoproduction and subsequent two-photon eta decay for fixed values of the energy. The detection efficiency is estimated as the fraction of all simulations corresponding to successful two-photon detection. Corrections are made for the occasional conversion of an eta decay photon

in the target outer casing, in the wall of a lead aperture, or in a veto counter or its lucite shield. The mylar windows of the aluminum target casing are taken into account in the conversion probability. The efficiency calculation is, of course, specific to the geometry of the target and the photon telescopes. For each target-telescope configuration of the experiment, the efficiency calculation must be carried out so as to cover the range of incident photon energies from threshold to the highest endpoint energy used. Figure 6.12 is a perspective view of the efficiency for a shower-counter-to-beam angle of $50^{\circ}$, mapped as a function of the incident photon energy and the cosine of the center of mass angle.

The simulation does not go so far as to fluctuate the decay photon energies according to the shower counter energy resolutions, nor is any account made of the electronic biases on the shower counter signals. The finite energy resolution of the shower counters is taken into account in the parametrization described in Section 3.4. As for the electronic biases, the appropriate discriminators had not been calibrated in terms of response probability as a function of pulse height. This point, which directly affects only the eta peak simulation (not the cross section unfolding), led to the introduction of artificial pulse height biases which overrode the electronic biases, as mentioned in Section 3.3.

Each simulated event is characterized by an origin in the hydrogen target, two angles describing the eta motion, and two more angles describing the two-photon eta decay. The latter set of angles are carefully restricted to a useful range containing all possible two-

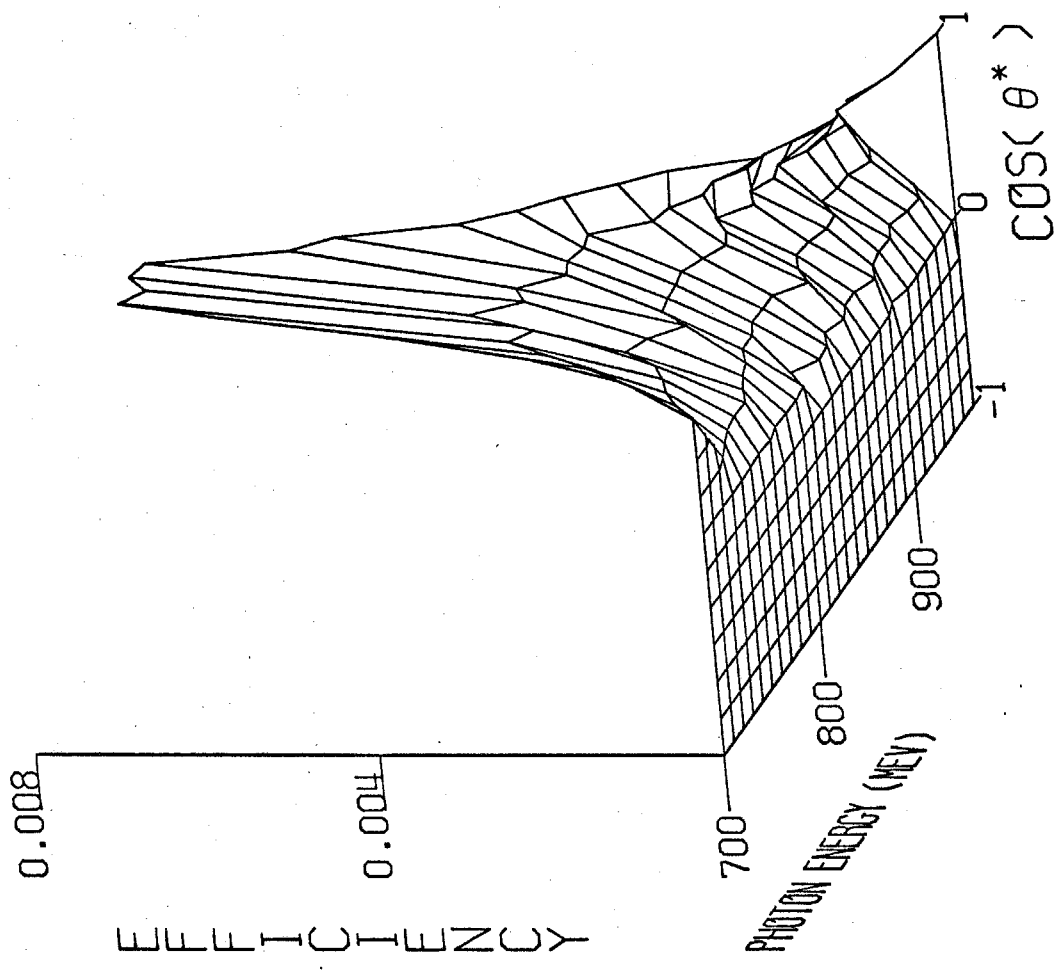


Figure 6.12 Detection Efficiency as a Function of Incident Photon Energy and Center-of-Mass Production Angle

photon detections, in order to reduce the computer running time. The target origin was varied over the irradiated volume of the hydrogen, and the angles of the eta motion were varied over a full sphere; however, the Monte Carlo randomness in these parameters was modified by a deliberate bias, again for the purpose of reducing computer time. As explained below, this bias was kept out of the efficiency estimation by assigning a statistical weight to each simulated event.

Consider a function of one variable, f(x), for which we desire an estimate of the mean, $\bar{f}$, defined as

$$\bar{f} = (b-a)^{-1} \int_a^b f(x)dx \quad . \tag{6.13}$$

This problem arises in the efficiency calculation, where f represents the detection probability and x represents the various free parameters and kinematical variables. For simplicity, we consider only one variable. The Monte Carlo approach is to estimate $\bar{f}$ as the average value of f over a set of randomly-chosen x. We denote this average value by $\bar{f}_N$, where N is the number of random choices of x. Explicitly,

$$\bar{f}_N = \frac{1}{N} \sum_{i=1}^{N} f(x_i) \ , \tag{6.14}$$

where it is understood that the $x_i$ are randomly chosen on the interval (a,b). This type of estimation is less subject to systematic error than methods which depend on an equally-spaced set of x, e.g. Simpson's rule, especially when there are several variables. The expectation value of $\bar{f}_N$, over all possible outcomes for the set of N choices of x,

is just $\bar{f}$, independent of N. The quality of the estimate, on the other hand, improves as N increases. The variance of $\bar{f}_N$ is given by

$$\sigma^2(\bar{f}_N) = \frac{\sigma^2(f)}{N} \tag{6.15}$$

where $\sigma^2(f)$ is the variance of f, which may be estimated as

$$\sigma^2(f) \cong \frac{1}{N-1} \sum_{i=1}^{N} (f(x_i) - \bar{f}_N)^2 \quad .$$

The Monte Carlo method described above is somewhat inefficient. The choice of x is random, even though f is more interesting where it is large than where it is small. Suppose that the choice of x is systematically biased, such that the probability of a choice falling in the interval (x, x + dx) is p(x)dx (normalized to unity over the entire range available). The expectation value of $\bar{f}_N$, calculated as in Eq. 6.14, is written as

$$\langle \bar{f}_N \rangle = \int_a^b p(x)f(x)dx = (b-a)^{-1} \int_a^b g(x)f(x)dx,$$

where g(x) is defined to be (b-a) times p(x). This expression reduces to $\bar{f}$, Eq. 6.13, only when g(x) = 1. However, suppose that we take (f/g) as the quantity to be averaged over N biased-random choices of x, i.e., consider the expectation value of $(\overline{f/g})_N$. It is

$$\langle (\overline{f/g})_N \rangle = (b-a)^{-1} \int_a^b g(x) \frac{f(x)}{g(x)} dx = \bar{f} ,$$

where

$$(\overline{f/g})_N = \frac{1}{N} \sum_{i=1}^{N} f(x_i)/g(x_i) ,$$

independent of N. It is now understood that the $x_i$ are chosen in accordance with the probability spectrum described by g. What is a good choice for g? Intuitively, g should follow f for an optimum estimate. This is confirmed by the expression for the variance of the estimate, Eq. 6.15, which becomes $N^{-1} \sigma^2(f/g)$. This vanishes when g is proportional to f. We do not a priori know f, but the evaluation of f at various x adds information to our picture of f. We may then choose g to be any non-zero approximation to f.

The biased-random type of Monte Carlo method described above was embodied in the computer program for calculating the detection efficiency. The function g(x) is in the nature of a statistical weight for each simulated eta event. The program occasionally pauses to re-calculate g on the basis of a smoothed version of the spectrum of f. One may easily show that g may be "refreshed" at any point in the calculation without altering the expectation value of the result, viz. $\bar{f}$. (A word of advice to would-be users of this method: g should be smoother and broader than the current estimate for f.) This method was applied to three of seven possible Monte Carlo variables; namely, the event origin in the target along the beam line only (the lateral displacement was directly randomized), and the two angles describing the motion of the eta. The two angles describing the two-photon eta decay were directly randomized within a restricted solid angle, which amounts to

using a step-function type of g.

B. Approximate, Closed Form Method

A useful check on the Monte Carlo efficiency calculation was furnished by the closed form type of calculation described below. This method suffers from an integrable singularity in the expression for the infinitesimal contribution to the efficiency, but the error introduced by the singularity decreases as one moves away from threshold in energy. At greater than about 100 MeV above threshold, the results of this calculation are in excellent agreement with those of the Monte Carlo calculation.

The method involves calculating the efficiency in closed form for pairs of point counters and a point target. This expression is then integrated over all pairs of point counters and all points of the hydrogen target. In practice, each finite counter was divided into a finite number of smaller counters, and the integral was approximated by a sum.

Consider the detection efficiency for a pair of point counters, for a point target, as depicted in Figure 6.13a . Constrain the two photons from an eta decay to enter apertues of infinitesimal solid angle, $d\Omega_1$ and $d\Omega_2$. This constrains the eta momentum vector to one of two possible directions, given the energy of the eta. However, at a certain energy, these two directions coalesce. This happens when $\beta = \cos(\theta_{\gamma\gamma}/2)$, where $\beta$ is the eta velocity and $\theta_{\gamma\gamma}$ is the two-photon opening angle. Below that energy, it is impossible to satisfy the constraint on the two photon directions.

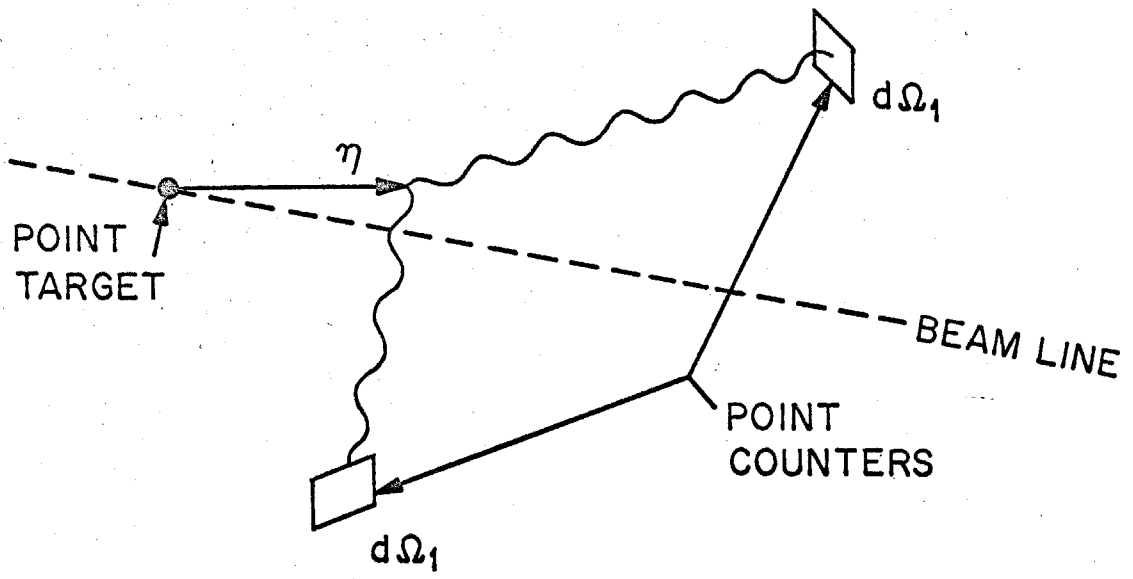


(a)

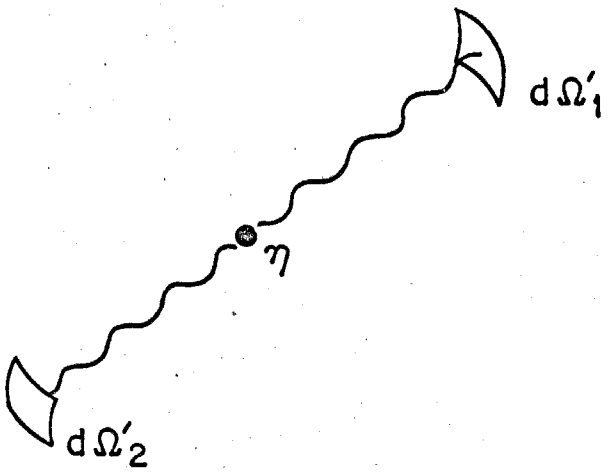


(b)

Figure 6.13 Geometry of Hypothetical Point Counters, as Seen in the Laboratory Frame (a) and the Eta Rest Frame (b)

Suppose that we are above the critical energy for detection with the point counters. In the eta center of mass frame, the point counters "appear" (to photons) as collinear with the point target, as shown in Figure 6.13b . The solid angles $d\Omega_1$ and $d\Omega_2$ are transformed into $d\Omega_1'$ and $d\Omega_2'$ . Let us calculate the probability for successful detection when the eta momentum is randomly chosen from an infinitesimal range of momenta perpendicular to the direction of the counter-target collinearity. Denoting this range of momenta by $d^2\vec{p}_\perp$, it is easily shown that the probability for successful detection is

$$P_{\gamma\gamma} = \frac{d\Omega_1' \, d\Omega_2'}{2\pi} \frac{(M_\eta/2)^2}{d^2\vec{p}_\perp}$$

where $M_\eta$ = eta mass.

Next, we relate $d^2\vec{p}_\perp$ to the eta momentum in the center of mass frame. If the eta energy is fixed, then the center of mass eta momentum, $\vec{p}^*$, is constrained to a spherical surface. An infinitesimal range of allowed momenta, $d^2\vec{p}^*$, will be perpendicular to $\vec{p}^*$ . Now transform to the eta rest frame, where the range $d^2\vec{p}^*$ is preserved by virtue of being transverse momentum. The plane of $d^2\vec{p}^*$ , however, need not be parallel with that of $d^2\vec{p}_\perp$ . Denote the dihedral angle between these planes by $\chi$. It follows that

$$d^2\vec{p}_\perp = |\cos\chi| d^2\vec{p}^* .$$

Therefore, if $\vec{p}^*$ is randomly chosen in the range $d^2\vec{p}^*$, then the

probability for a successful detection is

$$P_{\gamma\gamma} = \frac{d\Omega_1' \, d\Omega_2'}{2\pi} \frac{(M_\eta/2)^2}{|\cos \chi| d^2\vec{p}^*} \quad .$$

The probability that an eta of fixed energy will randomly have its momentum vector in the range defined by $d^2\vec{p}^*$ is

$$P_\eta = \frac{d^2\vec{p}^*}{4\pi|\vec{p}^*|^2} \quad .$$

Thus, the probability that an eta of fixed energy will be successfully detected by the point counters is

$$P = P_\eta \, P_{\gamma\gamma} = \frac{M_\eta^2}{32\pi^2} \frac{d\Omega_1' \, d\Omega_2'}{|\vec{p}^*|^2 |\cos \chi|} \quad , \qquad (6.16)$$

with the proviso that the fixed energy be above that allowed for any detection. Below that energy, P vanishes. The critical energy for detection corresponds to $\chi = 90^\circ$, which is a singular point in the expression for P.

One may now relate $d\Omega_1' \, d\Omega_2'$ to $d\Omega_1 \, d\Omega_2$ and the angle $\theta_{\gamma\gamma}$, and $\cos^2 \chi$ may be related to the eta center of mass quantities $\gamma_\eta^*$ and $\beta_\eta^*$ and the center of mass opening angle, $\theta_{\gamma\gamma}^*$ . We get that

$$d\Omega_1' \, d\Omega_2' = \sin^{-4}(\theta_{\gamma\gamma}/2) \, d\Omega_1 \, d\Omega_2$$

and $\cos^2\chi = (\gamma^*_\eta \beta^*_\eta)^{-2} (\gamma^{*2}_\eta - \sin^{-2}(\theta^*_{\gamma\gamma}/2))$ .

These expressions allow one to evaluate P, Eq. 6.16 , in terms of easily calculable quantities. Then the efficiency, for fixed energy and a point target, is the integral of P over all $d\Omega_1$ and $d\Omega_2$ of the finite counters. Finally, one may integrate over the finite target.

## 6.8 Electronic Dead Time, Empty Target Corrections

We discuss here certain small corrections to the eta yields. Eta events were occasionally lost because of the finite recovery time of electronic elements of the fast logic (Figure 2.2), and we estimate the loss as that due to the 1.5 ms recovery time of the Nuclear Data multi-channel pulse height analyzer. This loss was monitored by way of a scaler which counted the number of master triggers, which is also the number of times the Nuclear Data was gated. The number of gates accepted by the Nuclear Data appears as the number of events on magnetic tape, and the fraction of all gates not accepted, called the "dead time" and denoted here as f, is readily calculated. The instantaneous dead time may be independently estimated from the Nuclear Data recovery time, $\tau_{ND}$, and the time rate of the incoming gates, R. The relation is

$$f = R\,\tau_{ND} \quad . \tag{6.17}$$

R may be estimated using the fiducial events as time markers, since a fiducial event was generated at multiples of the time duration of one

beam dump. (Typically, there were 24 beam dumps between fiducial events.) From a knowledge of the dump time, and from counting the number of events between fiducial events on magnetic tape, one may estimate R. We tested this estimate by calculating $\tau_{ND}$ from Eq. 6.17, using the scaler-measured loss rate for f. For most runs, the $\tau_{ND}$ thus calculated came out about 2 ± 1 ms, more or less as expected. For certain runs, however, the calculation gave a value which was too large by up to a factor of 50. After reviewing this problem thoroughly, we concluded that the probable cause was erratic behavior in the scaler counting the number of master triggers. Thus, the scaler loss rate is a somewhat unreliable estimator of the dead time, although in most cases it appeared reasonable. Our estimation of R is also unreliable if the beam was especially unstable in intensity over the number of dumps between fiducial events. We used the scaler loss rate for the dead time correction to the eta yield, except that runs for which the dead time estimate was greater than 10% were rejected.

There was another source of dead time, one which was not carefully monitored, in the anticoincidence signals generated by the veto counters: Eta events might have been accidently vetoed. This is a potentially serious effect for the cross section asymmetry, since forward photoproduction is associated with higher counting rates and therefore higher accidental veto rates. We neglected to record the veto counter rates, which are necessary for a direct estimation of the accidental veto rates. There are some circumstantial bits of evidence, however, which indicate that the problem was not serious.

Work done early in the experiment establishes that the veto counter rates were typically 30 times the corresponding shower counter rates. Assuming that this ratio holds later in the experiment, we estimated the accidental veto rate for all runs. The largest estimate thus obtained was 2%, and a typical estimate was 0.5%. As further evidence, we have analyzed a run for which the soft-electron lucite shield was inadvertantly missing from its place in front of one of the veto counters. The eta yield for that run was almost identical with that for other runs at the same kinematical setting and with the lucite shields in place, even though the unshielded veto counter was scaling at many times its normal rate. We cannot, however, improve the other estimate of this effect directly, since the eta yields in this case were resolved to within only 10%. We summarize by guessing that the accidental veto rate is at most a 2% effect in the eta yields, and we explicitly assume that the effect is negligible.

A correction must be made for eta photoproduction from the complex nuclei of the empty target material in the beam. This amounts to about 0.016 inches of mylar (see Section 6.2) or about 4% of the total number of nucleons when the target is filled with liquid hydrogen. This correction was based on an estimate of the eta yields for both the empty and full targets, using the Monte Carlo detection efficiency, a trial cross section, and the relation for the estimated eta yield (Eq. 3.7). The detection efficiency was specially calculated for the empty target configuration, with the approximation that mylar is equivalent to liquid hydrogen at the same density of

nucleons per unit area. Any attempt to estimate the absolute empty target correction is overly dependent on the trial cross section, so we corrected in the ratio of the empty to full target estimated yields.

## 6.9 Synchrotron Endpoint Calibration

The synchrotron electron energy, which is the bremsstrahlung endpoint energy, was regulated and nominally measured using a system which measured the synchrotron magnetic field. The true endpoint energy was given as the product of a calibration constant and the nominal endpoint energy. Thiessen[25] gives this calibration constant as 1.021 ± 0.003, based on a precise measurement of the integrated output of the pickup coil located in the synchrotron's magnetic field. Other, unofficial values for this constant preferred 1.015. The exact value was significant in this experiment, since the endpoint energy defined the upper end of the photon energy range accepted by the apparatus.

We were able to independently measure the endpoint calibration constant using data taken just above the threshold for eta photoproduction. The fitting program BLKBOX (Section 3.6C) was applied to those data for which the endpoint energy was between 710 and 750 MeV. The usual threshold phase space factor was suppressed in the fitting. If we assume that S wave dominates near threshold, then the squared amplitude may be non-zero at threshold. The fitting program sought the smoothest fit to the squared amplitude for various choices of the endpoint calibration constant. $\chi^2$ was fixed to the value

corresponding to a linear fit, which makes the fitting program roughly equivalent to a line fitting program. The best fit occurred for a calibration constant of 1.021, which is that reported by Thiessen. The resolution in our measurement was seen by examining the fits for calibration constants of 1.018 and 1.024, shown in Figure 6.14 along with the fit for 1.021. Our resolution is seen to be roughly comparable with that of Thiessen, and our central value agrees with his.

## 6.10 Error Analysis

This discussion of the errors is divided into three parts. Sub-Section A describes a number of tests applied to the background-foreground fitting procedure. That method estimates the number of eta events for each experimental run, and that estimate is uncertain to the extent that it changes with respect to reasonable alterations in the fitting method. Sub-Section B discusses other uncertainties in the number of eta events and in the integrated beam energy. These uncertainties, together with those of the background-foreground fitting, give one an idea of the uncertainty in the eta yield, defined as the number of eta events per unit of integrated beam energy. The eta yield is the input to the cross section evaluation programs discussed in Section 3.6. Sub-Section C discusses systematic error in the cross section evaluation.

A. Background-Foreground Fitting Method

There are a number of quasi-arbitrary features of the back-

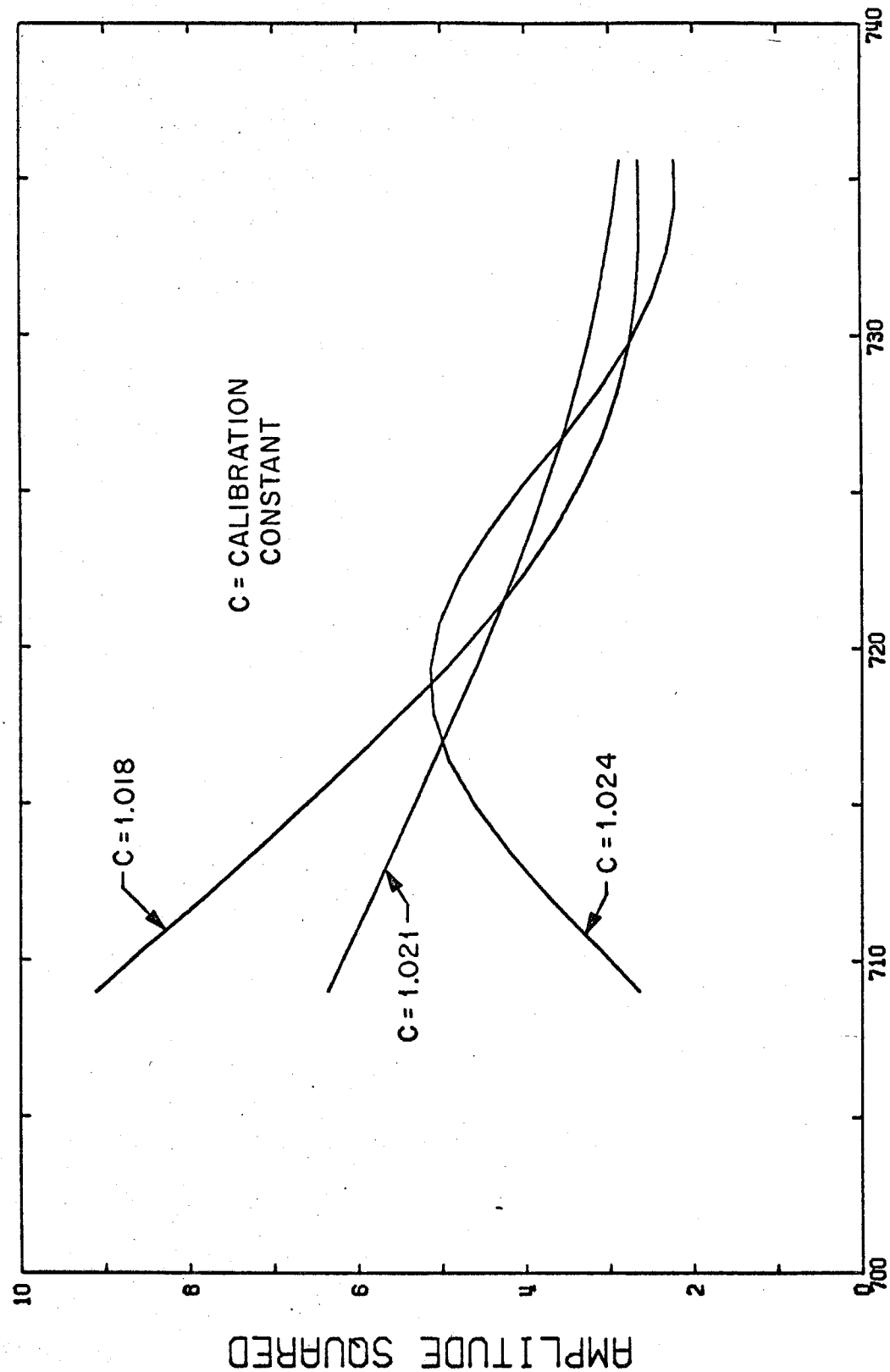


Figure 6.14 Squared Amplitude as a Function of Incident Photon Energy for Three Values of the Endpoint Calibration Constant

ground-foreground fitting method, such as the boundaries of the background and eta regions, the trial cross section used in generating the foreground term, the width of the energy bins, etc. All such features were fixed according to our best common-sense picture of the fitting problem, but there is ample room for variation of the method within that picture. We singled out three experimental runs for an intensive study of the fitting method. These runs were selected to represent photoproduction at forward, intermediate, and backward angles. We label these runs 1, 2, and 3, respectively. In terms of the angle between either photon telescope and the downstream beam line, $\theta_o$, and the synchrotron endpoint energy, $E_o$, the three runs are characterized by:

| Run | $\theta_o$, degrees | $E_o$, MeV |
|---|---|---|
| 1 | 45 | 850 |
| 2 | 55 | 800 |
| 3 | 80 | 775 |

The fitting method produces an estimate for the number of eta events, denoted $T_\eta$, and the estimated statistical error, i.e., the standard deviation, denoted $\sigma_\eta$. When we analyzed runs 1, 2, and 3 in exactly the same manner as all runs had been analyzed preparatory to the cross section evaluation, we obtained the following results for $T_\eta$ and $\sigma_\eta$:

| Run | $T_\eta$ | $\sigma_\eta$ |
|---|---|---|
| 1 | 764 | 36 |
| 2 | 1561 | 51 |
| 3 | 789 | 39 |

Denote the above values for $T_\eta$ by $T_\eta^o$ . We express changes in $T_\eta$ due to changes in the fitting method by the quantity $\Delta$, defined as

$$\Delta = \frac{T_\eta - T_\eta^o}{\sigma_\eta} \tag{6.17}$$

Additionally, we consider certain goodness-of-fit indicators. As explained in Section 3.5, the description of the experimental data is divided into background and foreground fitting problems, with the results of one serving as input for the other. We calculate goodness-of-fit indicators for the background and foreground fitting separately. The type of indicator we use is the number of standard deviations by which $\chi^2$ deviates from its expected value. This quantity is denoted FG and BG for foreground and background fitting, respectively. (For an exact definition of these quantities, see reference 5, Appendix E.) Note well that we do not express changes in FG or BG, but rather we express these quantities directly for each distinct alteration of the fitting method.

For reference, a number is associated with each test of the fitting method. The corresponding numbered paragraph below explains the nature of the test, and the corresponding row of Table 6.1

TABLE 6.1

EFFECTS OF VARIATIONS IN THE BACKGROUND-FOREGROUND FITTING METHOD

| TEST | Δ 1 | Δ 2 | Δ 3 | FG 1 | FG 2 | FG 3 | BG 1 | BG 2 | BG 3 |
|---|---|---|---|---|---|---|---|---|---|
| 0 | 0.0 | 0.0 | 0.0 | -0.23 | -1.13 | 0.19 | -0.92 | -0.27 | 0.15 |
| 1 | -0.01 | -0.01 | -0.08 | -0.32 | -1.29 | 0.12 | -0.83 | -0.59 | -0.19 |
| 2 | -0.51 | 0.13 | 0.0 | -0.21 | -1.15 | 0.19 | -1.15 | -0.04 | 0.15 |
| 3 | -0.03 | -0.07 | 0.96 | -0.27 | -1.01 | 0.22 | -0.90 | -0.08 | 0.69 |
| 4 | 0.02 | -0.04 | 0.13 | -0.22 | -1.14 | 0.20 | -0.02 | -0.59 | 0.37 |
| 5 | -0.34 | -0.28 | 0.48 | -1.64 | -1.60 | -1.46 | -0.92 | -0.27 | 0.15 |
| 6 | -0.15 | 0.54 | -0.71 | -0.27 | -0.98 | 0.03 | -0.83 | -0.48 | 0.05 |
| 7 | -0.04 | -0.01 | 0.04 | -0.26 | -1.14 | 0.26 | -0.97 | -0.29 | 0.34 |
| 8 | 0.01 | 0.06 | -0.02 | -0.28 | -0.47 | 0.51 | -0.92 | -0.27 | 0.15 |
| 9 | 0.03 | -0.06 | 0.13 | -0.20 | -1.20 | 0.19 | -0.02 | -0.59 | 0.37 |
| 10 | -0.01 | -0.01 | 0.04 | -0.17 | -1.04 | -0.06 | -0.92 | -0.27 | 0.15 |
| 11 | -0.51 | 0.16 | 0.24 | -0.76 | 0.63 | -0.06 | 0.11 | 1.00 | 0.61 |
| 12 | -0.47 | -0.18 | 0.26 | -0.33 | -1.81 | -1.03 | -0.41 | -0.16 | -0.35 |
| 13 | 1.69 | 2.90 | 1.00 | 0.49 | -0.34 | 1.81 | 2.16 | 2.12 | 2.24 |

presents the results of the test in terms of $\Delta$, FG, and BG. The unaltered fitting method is associated with the number zero. We consider $|\Delta| \gtrsim 1$ to be a serious change in the number of eta events. Similarly, when either FG or BG is greater than about 2, the quality of the fit is poor and warrants attention. For most of the cases discussed below, FG and BG indicated good fits and were consequently not mentioned.

(0) This is the case of the unaltered fitting method. By definition, Eq. 6. , $\Delta = 0$. Good fits are indicated by FG and BG.

(1) The background fitting is carried out over a domain of events called the "background region." That region excludes events near the eta peak via the so-called "eta cut" (see Section 3.5). For the first test, the eta cut was eliminated, i.e., no events near the eta peak were excluded from the background fitting. As seen in Table 6.1, this test had a negligible effect on $\Delta$, and FG and BG are practically undisturbed from their values for the unaltered fitting method.

(2) The background region excludes events with too low invariant masses via a "mass cut" (see Section 3.4). The boundary of the mass cut was normally 240 MeV, but for this test it was 280 MeV. Briefly, the purpose of the mass cut is to exclude the observed enhancement in the background at low masses. If the enhancement were not sufficiently excluded, then raising the mass cut boundary should cause the estimated number of eta events to decrease, i.e., $\Delta$ would be negative. Although $\Delta$ is moderately negative at a value of -0.51 for run 1, the value is +0.13 for kinematically similar

run 2. We feel that no systematic effect has been demonstrated by these values for $\Delta$. The identically zero $\Delta$ for run 3 requires some explanation. The mass cut competes with artificial biases on the separate shower energies in excluding events, and in some cases the artificial biases override the mass cut, as in run 3.

(3) For this test, the artificial energy biases on shower energies $E_1$ and $E_2$ were relaxed (see Section 3.4). Thus, additional events near the discriminator cutoffs were added to the background and foreground fitting problems. The original purpose of the artificial energy biases was to obviate a correction to the foreground term for the discriminator cutoffs. This test ostensibly reveals the consequences of fitting the data near the discriminator cutoffs without making the requisite correction to the foreground term. From Table 6.1, $\Delta$ is small for runs 1 and 2, but large (at 0.96) for run 3. This result prompted a closer examination, from which it was learned that the artificial energy biases were in the role of the mass cut by excluding events in the background enhancement, especially for runs which favored backward photoproduction. This was not the intended role of the energy biases, and we were fortunate that the energy biases were required for obviating the foregound correction.

(4) The eta cut was enlarged in a specific way for this test. Events situated above the eta peak in both $E_1$ and $E_2$ were excluded from the background region. The enlarged eta cut thus excluded events near the eta peak as well as events above the eta peak. The effect of this change was negligible in all indicators.

(5) The foreground fitting is carried out over a domain of events called the "eta region," the boundary of which is defined using the foreground term itself, as described in Section 3.5. For this test, the eta region was enlarged to include all events except those excluded by the mass cut and the artificial energy biases. The effect on $\Delta$ is moderate, and the sign of the effect appears to be correlated with whether the run is forward or backward photoproduction, insofar as runs 1, 2, and 3 are statistically representative of such a correlation. To check this point, we applied the same test to a number of additional runs. The results for those additional runs is not presented here, but we mention that the supposed correlation was not borne out. Thus, we take the magnitude of $\Delta$ to be significant for this test.

(6) Only events with the time difference signal sufficiently close to exact coincidence are accepted for background-foreground fitting. The "timing cut" described in Section 3.2 excludes other events. For this test, the timing cut was relaxed, so that many more accidental coincidences were included. The estimated number of accidental coincidences, denoted $T_A$, was automatically increased (see Section 6.6). The effect on $\Delta$ is moderate, but it is probably unreasonable to require that the fitting describe a large number of additional events in the nature of accidental coincidences. A more reasonable test is described below.

(7) For this test, the estimated number of accidental coincidences, $T_A$, was manually set to zero, overriding an automatic part

of the fitting program. In effect, the background fitting now "sees" the accidental coincidences previously estimated to be $T_A$ in number. It is reasonable to require that the background term describe this number of accidental coincidences, since the estimate for $T_A$ is dubious (Section 6.6). The effect on $\Delta$ is negligible and justifies using the dubious estimate. Although the timing cut was unaltered in this test, the net effect is similar to that of the previous test of the timing cut. That test, however, unrealistically admitted a large number of accidental coincidences, while the present test deals with only those accidental coincidences admitted normally via the timing cut. If we therefore accept the present test as the definitive one on the question of accidental coincidences, then we have shown that our treatment of the same, in terms of $T_A$, is entirely adequate.

(8) As discussed in Section 3.4, a trial cross section is incorporated in the foreground term. We used an isotropic version of the world data on the cross section, with the understanding that a version consistent with our measured cross section could be later substituted, if necessary, in order to make our measurements independent of world data. To show that such a substitution is unnecessary, the trial cross section energy dependence was temporarily replaced by a "flat" function of photon energy. The fitting is virtually insensitive to such a change, as seen in Table 6.1, and we are justified in not requiring the trial cross section to be consistent with the measured cross section in a detailed way.

(9) The Monte Carlo efficiency calculation (Section 6.7) is

used in generating the foreground term in the manner described in Section 3.4. Statistical fluctuations on the Monte Carlo calculation thus affect the foreground term, although the number of successfully simulated eta events was designed to be adequate for any foreground term. To confirm that the statistics were indeed adequate, the foreground term was artificially fluctuated in accordance with the expected Monte Carlo fluctuations. The negligible effect on fitting runs 1, 2, and 3, seen in Table 6.1, resulted from using the artificially fluctuated foreground terms.

(10) As discussed in Section 3.4, the foreground term embodies certain assumptions about the responses of the shower counters with respect to the energy of an incident photon. One such assumption is that the apparent number of photoelectrons varies linearly with incident photon energy, denoted $E_\gamma$. The slope of that energy dependence, assumed to intersect the origin, is the adjustable parameter $k_e$ in the foreground term. One expects $k_e$ to be a constant descriptive of the shower counters, but in fact, $k_e$ exhibits a dependence on the laboratory configuration of the shower counters. That dependence emerges from adjusting $k_e$ to fit the experimentally produced eta peaks via the foreground fitting. One possibility is that the apparent number of photoelectrons is not truly linear in $E_\gamma$. To first order, one possible departure from linearity in energy may be approximated as a shift in the point in $E_\gamma$ where the linear fit extrapolates to zero apparent photoelectrons, preserving the assumed linearity characterized by the quantity $k_e$. The intersection with the $E_\gamma$ axis is ordinarily at $E_\gamma = 0$, but for this test the intersection point was

at $E_\gamma$ = -200 MeV. As seen in Table 6.1, such a change had practically no effect on the fitting results. Thus, quite apart from the reason for any departure from linearity, or for the dependence of $k_e$ on shower counter configuration, only a negligible error is made with the assumption of linearity.

(11) As first explained in Section 3.3, the shower counter energies $E_1$ and $E_2$ are divided into 20-MeV bins to produce the integers $i_1$ and $i_2$. For this test, the energy bin width was changed to 40 MeV. In retrospect, such a change is probably too drastic, since the shower counter energy resolution is on the order of 40 MeV at only 500 MeV incident photon energy. The resulting $\Delta$, Table 6.1, nevertheless indicates only a moderate effect on the estimated number of etas. The quality of the fits, as indicated by the quantities FG and BG, shows a noticeable deterioration.

(12) This test and the following one deal with the departure of the background from a strictly uncorrelated spectrum in $E_1$ and $E_2$. Rather than confining our consideration to the well-studied enhancement of the background at low masses, we considered a "long-range" departure from an uncorrelated spectrum. As discussed in Section 6.6, the background is described by the term $F_1(i_1)F_2(i_2)$, where $i_1$ and $i_2$ are the energy bin indices of the shower energies $E_1$ and $E_2$. Denote the mean value of $E_1$ by $\langle E_1 \rangle$ , and the standard deviation of $E_1$ by $\sigma(E_1)$, and similarly for $E_2$. The simplest type of correlated spectrum which one can write in terms of $F_1$ and $F_2$ is

$$F_1 F_2 \left(1 + \alpha \frac{(E_1 - \langle E_1 \rangle)(E_2 - \langle E_2 \rangle)}{\sigma(E_1)\,\sigma(E_2)}\right) , \qquad (6.18)$$

where $\alpha$ is a constant. The correlation coefficient for such a spectrum, over any rectangular set of $(i_1, i_2)$ bins, is just $\alpha$. This is one example of a possible long-range type of correlation. Our test of the fitting involved creating artificial data incorporating exactly such a long-range correlation, then fitting that data with the ordinary fitting method with its uncorrelated background term. The eta peak was included in the artificial data, and the number of counts in each $(i_1, i_2)$ bin was fluctuated according to Poisson statistics. Apart from the correlation described by the quantity $\alpha$, the artificial data were modeled after the experimental data for runs 1, 2, and 3. The present test is actually a control, in the sense that $\alpha$ was set to zero, while the following test had $\alpha = 0.1$. As seen in Table 6.1, this control test shows good foreground and background fits, and the $\Delta$ indicates only that the artificial data were patterned after the experimental data reasonably well in the number of eta events. The following test completes the discussion by pointing out the effects of taking $\alpha$ as 0.1.

(13) As explained above, this test and test 12 involve fitting artificially generated data using the deliberately correlated term (6.18) for the background. A 10% long-range correlation ($\alpha = 0.1$) appeared in the data for this test, whereas test 12, as a control, had an uncorrelated background. The artificial data were fluctuated independently for test 12 and 13, so that any systematic difference

between the two tests will be modulated by ordinary statistical variation. In Table 6.1 we see pronounced differences between tests 12 and 13, which rules out statistical variation as the cause of those differences. There is a marked increase in $\Delta$ for all three runs, accompanied by a severe deterioration of the quality of the fits, especially the background fits. It is safe to say that a 10% long-range background correlation is inconsistent with the observed high quality of the background fits to the experimental data. This is fortunate, because the large $\Delta$ for this test represents an intolerable systematic error. We do not hazard a guess for an upper limit on the long-range background correlation, but rather we assume that it is negligible. In passing, we mention that the long-range correlation was measured (via the correlation coefficient) for the below-threshold experimental data, and no evidence of long-range correlation could be detected within statistical error.

B. Uncertainties in the Eta Yield

The eta yield is defined as the number of eta events, $T_\eta$, divided by the integrated beam energy, W. We have previously enumerated systematic uncertainties in the background-foreground fitting method. Here we review those uncertainties along with the corrections discussed in Section 6.8. We also estimate the size of the errors in the measurement of W, finishing with an idea of the uncertainties in the eta yield. Sub-Section C below completes the error analysis by discussing the uncertainties in the cross section evaluation.

The background-foreground fitting process produces an estimate for the number of eta events, $T_\eta$, as well as an estimate for the statistical error on $T_\eta$, denoted $\sigma_\eta$. We have assumed that the estimate for $\sigma_\eta$ is accurate, but that assumption is subject to experimental verification. We may divide a set of events into several subsets and apply the fitting method to each subsets individually, and the observed fluctuation in $T_\eta$ over the subsets allows an independent determination of $\sigma_\eta$. In addition, the sum of $T_\eta$ over the subsets should be equal to $T_\eta$ for the undivided set of events. In order to check these points, we have divided each of the previously studied runs, denoted 1, 2, and 3, into ten equal sub-runs. Table 6.2 lists the values for $T_\eta$ and $\sigma_\eta$ returned by the fitting program for each of the sub-runs. Below this information is listed the sum of $T_\eta$ and the Pythagorean sum of $\sigma_\eta$, followed by the values obtained by fitting the undivided runs, denoted $T_\eta^o$ and $\sigma_\eta^o$. Finally, we express the difference between $T_\eta$ and $T_\eta^o$ by $\Delta$, as defined in Eq. 6.17. The values for $\Delta$ show that the fitting method is reasonably independent of the size of the sample of events, even though the sign of $\Delta$ is negative for each of the runs. As for the independent check on the estimate for $\sigma_\eta$, we calculate an experimental value for $\sigma_\eta$, denoted $\sigma_\eta^{exp}$, from the fluctuation of $T_\eta$ over the sub-runs. This should be compared with the root-mean-square value for $\sigma_\eta$, denoted $\sigma_\eta^{rms}$. The values for these quantities are:

TABLE 6.2

RESULTS OF FITTING SUB-DIVIDED RUNS

| Subset Number | Run 1 | | Run 2 | | Run 3 | |
|---|---|---|---|---|---|---|
| | $T_\eta$ | $\sigma_\eta$ | $T_\eta$ | $\sigma_\eta$ | $T_\eta$ | $\sigma_\eta$ |
| 1 | 85.40 | 12.17 | 145.62 | 15.36 | 72.59 | 10.24 |
| 2 | 81.23 | 10.74 | 163.44 | 15.18 | 64.03 | 10.66 |
| 3 | 75.56 | 10.32 | 158.67 | 15.58 | 90.87 | 12.65 |
| 4 | 64.99 | 9.44 | 182.87 | 17.16 | 80.23 | 10.85 |
| 5 | 73.57 | 10.17 | 146.44 | 14.28 | 76.30 | 12.47 |
| 6 | 76.89 | 11.19 | 152.57 | 14.85 | 75.13 | 11.95 |
| 7 | 62.56 | 10.37 | 134.14 | 14.55 | 83.84 | 10.83 |
| 8 | 99.50 | 11.54 | 149.69 | 13.95 | 91.53 | 11.92 |
| 9 | 63.85 | 10.62 | 146.77 | 16.88 | 69.03 | 11.26 |
| 10 | 77.32 | 11.06 | 162.32 | 15.04 | 75.39 | 11.08 |
| Totals* | 760.87 | 34.10 | 1542.53 | 48.42 | 778.94 | 37.17 |
| $(T_\eta^o \pm \sigma_\eta^o)$ | 763.68 | 36.10 | 1561.07 | 50.67 | 789.10 | 39.18 |
| $\Delta$ | -0.08 | | -0.36 | | -0.26 | |

*Pythagorean sum, for $\sigma_\eta$

| Run | $\sigma_\eta^{exp}$ | $\sigma_\eta^{rms}$ |
|---|---|---|
| 1 | 13.4 | 15.3 |
| 2 | 11.2 | 10.8 |
| 3 | 8.9 | 11.8 |

We regard this as evidence that the estimate for $\sigma_\eta$ returned by the fitting program is believable.

It remains to find an estimate, however crude, for the systematic uncertainty associated with the fitting process. This subject was the motivation for the special tests described in Sub-Section A above. Those tests are not entirely independent of each other, nor do they encompass all conceivable tests, but they give a fair idea of the uncertainty involved. Certain of those tests, however, should probably be disregarded, on the grounds that a reasonable range of variation in the fitting method was exceeded. In test 3, for example, the artificial energy baises were relaxed, deliberately violating the reasons for introducing those biases. Test 6 should be considered as having been supplanted by test 7. The energy bin widening in test 11 was excessive, as was the amount of "long-range correlation" introduced in tests 12 and 13. We therefore discount the results of these tests. It is important to note that, of the remaining tests, the values for $\Delta$ appeared to be statistically independent of whether the run involved forward or backward photoproduction (although the statistics are poor for only three runs).

For a crude estimate of the systematic uncertainty in the fitting method, we take the Pythagorean sum of $\Delta$ over tests 1, 2, 4,

5, 7, 8, 9, 10. From Table 6.1, we get values of 0.61, 0.32, and 0.52 for runs 1, 2, and 3 respectively, for a run-averaged value of 0.48. In words, then, the systematic uncertainty is about half as great as the statistical standard deviation. We wish to express this finding as a fractional uncertainty in the number of eta events. For this purpose, we have calculated the average statistical error over all runs of the experiment, and the result is between 5 and 8 percent, depending on how one weights the individual runs. Taking the upper figure, we may say that the fitting method estimates the number of eta events with a 4 percent uncertainty, of a kind which affects forward and backward photoproduction equally and in the same direction.

Section 6.8 discussed corrections to the number of eta events (or, equivalently, to the eta yield)from the electronic dead time and the empty target contribution. The dead time correction was uncertain for two reasons. First, a crucial scaler was apparently malfunctioning in an unpredictable fashion, and, second, the veto scalers were not systematically recorded. However, the explicitly calculated dead time correction was usually on the order of 1 percent, and the unknown veto dead time was estimated to be less than 2 percent. From this, we assume that the uncertainty in the dead time correction is about 1 percent, of a kind which may affect forward and backward photoproduction differently, causing the forward cross section to be slightly underestimated. The empty target contribution was typically 5 percent, and we estimate an uncertainty of 1 percent in that correction (from the assumption that mylar is equivalent to liquid hydrogen for

the same density of nucleons per unit area).

We turn now to uncertainties in the beam energy measurement (cf. Section 6.1). The theoretical value for $U_Q$ is (5.78 ± 0.18), or 3 percent uncertain.[17] The uncertainty from all other sources in the beam monitoring system is taken as 1 percent, coming primarily from the calibration of the ion chamber against the qunatameter (cf. Figure 6.1).

Finally, the uncertainty in the eta yield may be estimated from the above considerations. (Recall that the eta yield is defined as the number of eta events per unit of integrated beam energy.) The results are expressed as follows:

| Source of Uncertainty | Contribution to Eta Yield, Percent | Contribution to Forward-Backward Eta Yield Difference, Percent |
|---|---|---|
| Fitting method | 4 | 1 |
| Dead time correction | 1 | 0 |
| Empty target correction | 1 | 0 |
| Value for $U_Q$ | 3 | 0 |
| Beam Monitoring | 1 | 0 |
| Absolute sum | 10 | 1 |
| Pythagorean sum | 5 | 1 |

Thus, the eta yield is uncertain by as much as 10 percent, or 5 percent if there was no conspiracy among the contributing sources of uncer-

tainty. We emphasize that only the dead time correction is considered likely to affect forward and backward photoproduction differently.

C. Uncertainties in the Cross Section Evaluation

Section 3.6A describes the elements of the cross section evaluation. We now consider the systematic uncertainties involved, which, together with the previously enumerated uncertainties in the eta yield, lead to an idea of the total uncertainty in the cross section results presented in Section 4.

The branching ratio for two-photon eta decay, denoted $\Gamma$, has been taken as $(0.375 \pm 0.016)$ from reference 20, for a 4 percent uncertainty. The number of protons per unit area in the hydrogen target, denoted $N_p$, is probably known to better than 0.5 percent, which we neglect. The bremsstrahlung photon energy spectrum, denoted $N_\gamma$, is known to about 1 percent, except near the endpoint where it is uncertain by about 5 percent; we take the overall uncertainty as 2 percent. We take the uncertainty in the endpoint energy as negligible. The Monte Carlo detection efficiency, denoted $\epsilon$, contributes a purely statistical error of from 1 to 3 percent to the cross section.

Geometrical errors were serious enough to warrant our special attention. The position of the hydrogen target was first deduced from the results of surveying sessions, until it was learned that certain corrections had been overlooked. Fortunately, we had taken a redundant set of target position measurements using a plumb bob attached to the target. Those measurements, which we finally accepted, were uncertain by about 0.1 inches in the target position along the

beam line. This translates to roughly a 1 percent uncertainty in the forward-backward cross section difference. A related geometrical error was present in the positioning of the shower counters, which was also uncertain by about 0.1 inches. This amounts to roughly a 1 percent statistical error on the cross section, without regard to forward or backward photoproduction. Both kinds of geometrical error logically belong in the uncertainty in the detection efficiency, which we therefore take as 4 percent.

We now collect our previous estimates of the uncertainties involved, taking the eta yield uncertainty as 5 percent, 1 percent of which affects the forward-backward cross section difference directly. Thus, the overall uncertainty in the cross section, apart from statistical error on the eta yields, is:

| Source of Uncertainty | Contribution to Cross Section, Percent | Contribution to Forward-Backward Cross Section Difference, Percent |
|---|---|---|
| Eta Yield | 5 | 1 |
| Branching ratio | 4 | 0 |
| Bremsstrahlung spectrum | 2 | 0 |
| Detection Efficiency | 4 | 1 |
| Absolute sum | 15 | 2 |
| Pythagorean sum | 8 | 2 |

## 7. REFERENCES


1. B. D. Winstein, Ph.D. Thesis, California Institute of Technology (1970). Also see C. A. Heusch et al., Phys. Rev. Letters 25, 1381 (1970).
2. C. Bacci et al., Phys. Rev. Letters 20, 571 (1968).
3. B. Delcourt et al., Physics Letters 29B, 75 (1969).
4. R. P. Bajpai and A. Donnachie, Nuclear Physics B12, 274 (1969).
5. S. J. Yellin, Ph.D. Thesis, California Institute of Technology (1971).
6. R. Prepost, D. Lundquist and D. Quinn, Phys. Rev. Letters 18, 82 (1967).
7. Y. C. Chau, N. Dombey and R. G. Moorhouse, Phys. Rev. 163, 1632 (1967).
8. J. L. Alberi et al., Phys. Rev. 176, 1631 (1968).
9. B. M. K. Nefkens et al., UCRL-19281, unpublished.
10. L. D. Roper, Phys. Rev. Letters 12, 340 (1964).
11. R. G. Moorhouse, Phys. Rev. Letters 16, 772 (1966).
12. C. A. Heusch, C. Y. Prescott and R. F. Dashen, Phys. Rev. Letters 17, 1019 (1966).
13. R. L. Walker, Phys. Rev. 182, 1729 (1969).
14. P. S. L. Booth et al., DNPL/P56, to be submitted to Nuclear Physics B.
15. R. Littauer, Rev. Sci. Instr. 25, 148 (1954).
16. R. R. Wilson, Nuclear Instruments 1, 101 (1957).

17. H. A. Thiessen and J. Pine, CALT-68-76 (1966), unpublished.

18. C. Y. Prescott, CTSL-1, unpublished.

19. H. Ruderman, R. Gomez and A. V. Tollestrup, CTSL-31, unpublished.

20. Particle Data Group, Physics Letters 33B, 1 (1970).

21. R. F. Deery, CTSL-11, unpublished.

22. F. Wolverton, "Manual for BPAK I, Thick Radiator Bremsstrahlung Computer Program," unpublished.

23. C. A. Moore, "SOLVE," unpublished.

24. J. Hamilton and W. S. Woolcock, Rev. Mod. Phys. 35, 737 (1963).

25. H. A. Thiessen, CTSL-21, unpublished.

26. L. S. Rochester, Ph.D. Thesis, California Institute of Technology (1968). See also E. D. Bloom, C. A. Heusch, C. Y. Prescott and L. S. Rochester, Phys. Rev. 21, 1100 (1968).

27. P. S. L. Booth, et al., Lett. al Nuovo Cimento 2, 66 (1969).

28. C. Bacci, et. al, Physics Letters 28B, 687 (1969).

29. R. H. Dalitz, Ann. Rev. Nucl. Sci. 13, 339 (1963).

30. A. T. Davies and R. G. Moorhouse, Nuovo Cimento 52, 1112 (1967).

31. B. T. Feld, "Models of Elementary Particles," Blaisdell Publishing Company, Waltham, Massachusetts (1969), p. 359.

32. S. Gasiorowicz, "Elementary Particle Physics," John Wiley and Sons, Inc., New York (1966), p. 281.

33. W. B. Richards, et. al., Phys. Rev. D1, 10 (1970).

34. F. Gürsey, A. Pais, and L. A. Radicati, Phys. Rev. Letters 13, 299 (1964).

35. R. D. Tripp, et. al., Nucl. Phys. B3, 10 (1967).

36. Cambridge Bubble Chamber Group, Phys. Rev. 163, 1510 (1967).

37. Aachen-Berlin-Bonn-Hamburg-Heidelberg-München Collaboration, Phys. Rev. 175, 1669 (1968).

38. G. Gialanella, et. al., Nuovo Cim. 63A, 892 (1969).

39. E. Flaminio, et al., BNL Preprint 14572 (1970).